# Multiscale Reduced Order Models for the Geometrically Nonlinear Response of Complex Structures

by

Ricardo Angel Perez

A Dissertation Presented in Partial Fulfillment
of the Requirements for the Degree
Doctor of Philosophy

Approved November 2012 by the
Graduate Supervisory Committee:

Marc Mignolet, Chair
Jay Oswald
Stephen Spottswood
Pedro Peralta
Hanqing Jiang

ARIZONA STATE UNIVERSITY

December 2012

ABSTRACT

The focus of this investigation includes three aspects. First, the development of nonlinear reduced order modeling techniques for the prediction of the response of complex structures exhibiting "large" deformations, i.e. a geometrically nonlinear behavior, and modeled within a commercial finite element code. The present investigation builds on a general methodology, successfully validated in recent years on simpler panel structures, by developing a novel identification strategy of the reduced order model parameters, that enables the consideration of the large number of modes needed for complex structures, and by extending an automatic strategy for the selection of the basis functions used to represent accurately the displacement field. These novel developments are successfully validated on the nonlinear static and dynamic responses of a 9-bay panel structure modeled within Nastran. In addition, a multi-scale approach based on Component Mode Synthesis methods is explored.

Second, an assessment of the predictive capabilities of nonlinear reduced order models for the prediction of the large displacement and stress fields of panels that have a geometric discontinuity; a flat panel with a notch was used for this assessment. It is demonstrated that the reduced order models of both virgin and notched panels provide a close match of the displacement field obtained from full finite element analyses of the notched panel for moderately large static and dynamic responses. In regards to stresses, it is found that the notched panel reduced order model leads to a close prediction of the stress distribution obtained on the notched panel as computed by the finite element model. Two enrichment techniques, based on superposition of the notch effects on the virgin panel stress field, are proposed to permit a close prediction of the stress distribution of the notched panel from the reduced order model of the virgin one. A very

good prediction of the full finite element results is achieved with both enrichments for static and dynamic responses.

Finally, computational challenges associated with the solution of the reduced order model equations are discussed. Two alternatives to reduce the computational time for the solution of these problems are explored.

*A mi familia, gracias por brindarme su apoyo y amor.*

*To Whittney, thank you for your constant love, patience, and support.*

*And whatever you do, whether in word or deed, do it all in the name of the Lord Jesus, giving thanks to God the Father through him (Colossians 3:17).*

ACKNOWLEDGMENTS

First, I would like to thank my advisor, Dr. Marc Mignolet, for his guidance and support, I have learned many things from him throughout my studies at ASU.

Special thanks are due to the members of my dissertation committee Dr. Mike Spottswood, Dr. Pedro Peralta, Dr. Hanqing Jiang, and Dr. Jay Oswald for their participation and support.

The financial support of this work, by the grant FA9550-10-1-0080 from the Air Force Office of Scientific Research with Dr. David Stargel as grant monitor, is gratefully acknowledged.

Additionally, I would like to thank Dr. Xiaoquan Wang, Dr. Javier Avalos, Dr. Raghavendra Murthy, and Mr. Andrew Matney, for their friendship and support.

TABLE OF CONTENTS

Page

CHAPTER Page

LIST OF TABLES

Table Page

LIST OF FIGURES

Figure Page

Figure Page

Figure Page

Figure Page

Figure Page

Figure Page

Figure Page

Figure Page

Figure Page

Figure Page

# CHAPTER 1

# OVERVIEW

## 1.1 Motivation

The development of affordable and reusable hypersonic vehicles has been a goal of the USAF and NASA for several years. These hypersonic aircraft operate in very complex environments, with loads that arise from the aerodynamics, acoustics, and thermal effects. These loads in turn, arise from the engine exhaust, turbulence, aerodynamic heating, among other sources (see [1] for a detailed description of these conditions). Furthermore, these loads are large enough, alone or in combination, to induce geometrically nonlinear behavior of the structure and/or its substructures. The nonlinearity results in a stiffening of the structure, due to coupling between bending and membrane stretching which occurs as out-of-plane loading is applied. Therefore, the geometric nonlinearity is in general beneficial; unfortunately it leads to difficulties in the prediction of the response. In addition, the dynamic excitation is also likely to create fatigue (sonic fatigue) and eventually cracks in the panels. The appearance of such cracks will trigger the key question: when will the panels have to be replaced to maintain safe flight conditions? Therefore, there are three computational challenges in the prediction of the response of hypersonic aircraft:

- High loading which results in geometric nonlinear effects.
- Coupling between aerodynamics, thermal problem, and structure implies three separate analyses that must share information.
- Prediction of fatigue life and damage as well as health monitoring for specific mission profiles.

Clearly, accurate and efficient computational tools are needed to address questions during the design stages, but also during the lifespan of the aircraft to be able to

deal with maintenance issues in an efficient way. Such predictions are clearly within the range of standard, commercial finite element software (e.g. Nastran and Abaqus), but even with current computing power they imply a computationally heavy task. The computational expense will be even more for panels that have cracks, because of the fine meshing required near the cracks to accurately capture the stress field. Furthermore, the random nature of the acoustic loading and uncertainties in the loads and in the model, would transform the problem into a random vibration one, which might require the consideration of multiple time histories in a Monte Carlo setting.

### 1.2. Linear Reduced Order Models - Modal Models

For a system with *N* degrees-of-freedom a set of *N* coupled equations has to be solved in order to obtain the response of the system. The solution becomes more complex as *N* becomes large. In such cases, a method known as *modal analysis* [2] allows to obtain the dynamic response with a much smaller number of degrees-of-freedom.

Consider the following discrete *N*-degree-of-freedom linear dynamic system

$$\underline{\underline{M}}\,\underline{\ddot{u}} + \underline{\underline{D}}\,\underline{\dot{u}} + \underline{\underline{K}}\,\underline{u} = \underline{F} \tag{1.1}$$

where *M*, *D*, and *K* are the mass, damping, and stiffness matrices of the system; they are $N \times N$ matrices. The homogeneous solution of the undamped system (*D* equal to the zero matrix) results in *N* eigenvalues and *N* eigenvectors (mode shapes). Assuming the structure is classically damped, the undamped and damped mode shapes coincide [3]. The mode shapes, due to their property of orthogonality, are linearly independent, so they form a basis of the *N*-dimensional space. This means that the solution of Eq. (1.1) can be expressed as follows

$$\underline{u}(t) = \sum_{n=1}^{N} q_n(t)\,\underline{\psi}^{(n)} \tag{1.2}$$

where the $q_n(t)$ are called the generalized coordinates and $\underline{\psi}^{(n)}$ are the mode shapes.

Since the mass and stiffness matrices of the system are symmetric, and assuming the modes are mass normalized, the following properties follow:

$$\begin{aligned} \left(\underline{\psi}^{(n)}\right)^T \underline{\underline{M}}\,\underline{\psi}^{(n)} &= 1 \\ \left(\underline{\psi}^{(n)}\right)^T \underline{\underline{K}}\,\underline{\psi}^{(n)} &= \omega_n^2 \end{aligned} \tag{1.3}$$

where, $\omega_n$ is the $n^{th}$ natural frequency from the undamped system. Therefore, substitution of Eq. (1.2) into Eq. (1.1), pre-multiplying by the transpose of the mode shapes, and using Eqs. (1.3) yields a set of uncoupled differential equations

$$\ddot{q}_i + 2\varsigma\omega_i\dot{q}_i + \omega_i^2 q_i = F_i \quad \text{for}\, i = 1,...,N \tag{1.4}$$

where, $\varsigma$ is the damping ratio of the system. Furthermore, the solution can be approximated by truncating Eq. (1.2) to *M* modes, where $M << N$.

**1.3. Nonlinear Reduced Order Models**

Linear modal models are easy to build from commercial finite element codes. The advantage in using commercial codes is in the availability of a variety of materials, boundary conditions, loadings, and types of analyses (e.g., linear static, nonlinear static, etc.).

The extension of linear modal models to the study of structures undergoing "large" deformations (i.e., exhibiting geometric nonlinearity) has received significant attention during the last decade or so. The formulation of these nonlinear reduced order models (ROMs) is based on the use of finite element models generated using *commercial* codes (e.g. Nastran, Abaqus, DYNA3D), see [4] for a recent review. This not only facilitates the analysis of realistic structural models and complex boundary conditions,

but it also permits a direct transition to the industrial setting where they are routinely used.

The ROM capabilities have progressed significantly during the last decade or so. Starting with applications to flat structures, the ROM methodology has been used to predict the response of simple clamped-clamped beams (see [5-8]), flat cantilevered beams (see [9]), and panels (see [10-12]) under both dynamic and static loadings. Also, the analysis of moderately large deflections of curved structures has been performed (see [13-17]). The coupling of these nonlinear structural reduced order models with aerodynamics, either full or reduced order model, has also been successfully demonstrated in [18-20]. The coupling of the structural dynamics and thermal aspects, the two in reduced order model format, has been proposed and validated for uniform steady-state thermal loadings of beams and panels [21], non-uniform transient temperature fields of a 3-D panel [22], the structural dynamic analysis of a beam subjected to a moving heat flux [23], and the analysis of a 3-D hypersonic panel [24].

These developments have dealt with mono-bay structures, i.e., beams and plates with various boundary conditions, material properties, and loads. However, structures are seldom free of imperfections, and cracks, debonds, fasteners, shock impingement points, etc. can have a significant effect in the stress field. Furthermore, aircraft are formed from assemblies of elastic substructures and components (e.g., panels, spars, ribs, etc.). Therefore, the interaction of these components under high loading conditions can be significant. In this light, an important challenge in the development of the ROM capabilities is to be able to go from mono-bay structures ("meso" scale) down to the "micro" scale and up to the "macro" scale. Shown in Fig. 1.1 is a schematic that illustrates these three different scales.

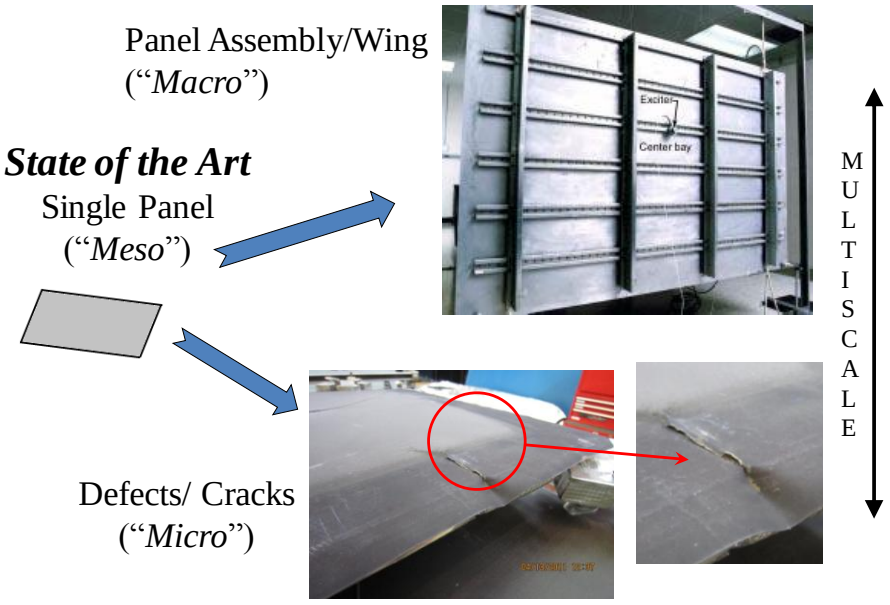


Figure 1.1. Schematic showing examples of the micro, meso, and macro scales.

The final challenge will be to incorporate the multi-scale character of the structure with the multidisciplinary nature that arises from the variety of loadings described in section 1.1. Shown in Fig. 1.2 is a schematic of these challenges, where all the couplings are represented by arrows. The present work will focus on the structural problem with acoustic loading.

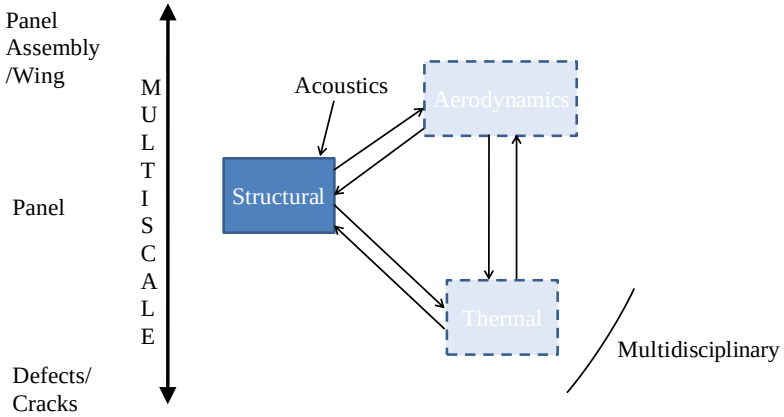


Figure 1.2. Schematic showing the multi-scale and multidisciplinary aspects of the computational challenges in the prediction of the response of hypersonic aircraft

The objective of the present work is to expand the ROM capabilities to the macro and micro-scales. There are two key aspects in the construction of a ROM: the

identification of the ROM parameters and the selection of a basis to represent the motions. The challenges associated with these two aspects have been seen to increase as more complex structural models are studied, since larger ROMs are required to capture the dominant aspects of the response. This in turn, implies an increase in the computational effort in the identification of the ROM parameters. In this light, a novel approach that requires a reduced computational effort for the identification of the ROM parameters will be introduced. The other challenge is related to the selection of a basis, so a new type of basis enrichment will be presented. Both propositions make use of the tangent stiffness matrix of the structure computed at certain displacement configurations. Furthermore, they will facilitate the construction of ROMs for complex models such as those within the macro-scale category. A validation on a complex structure will proceed.

The second objective is to assess the ROM capabilities for problems in the micro-scale. The main question to be addressed is: Can a displacement-based ROM capture a localized stress distribution? The following phenomenological issues will be addressed:

1) Is the displacement field affected by the local defect?
2) Does the defect need to be accounted for in the displacement?
3) Can a local enrichment of the stress be developed?

### 1.4. Outline

In Chapter 2 a background of nonlinear reduced order modeling is presented. The formulation of the ROM equations, along with the general methodology for the identification of the ROM parameters, and a discussion on the selection of the basis to represent the displacements is reviewed.

In Chapter 3, the formulation of the new identification procedure for the ROM parameters is discussed. In addition, the new type of basis enrichment is presented. The advantages of the new identification procedure are discussed.

In Chapter 4, the results of the validation of the methodologies developed in Chapter 3 on a complex model will be presented. The validation consists of static and dynamic excitations. In addition, a multi-scale approach based on Component Mode Synthesis tools is explored on a 9-bay panel.

The assessment of the ROM capabilities for problem in the micro-scale is done in Chapter 5. Both static and dynamic validation results are presented.

Two algorithmic improvements aimed at reducing the computational time of the solution of the ROM equations of motion are presented in Chapter 6. A summary is presented in Chapter 7.

# CHAPTER 2

# BACKGROUND ON REDUCED ORDER MODEL FORMULATION

## 2.1. Introduction

A reduced order model (ROM) is defined here as a modal-like representation of the displacement field $u_i$

$$u_i(\underline{X},t)=\sum_{n=1}^{M} q_n(t)\,U_i^{(n)}(\underline{X}) \tag{2.1}$$

In these equations, the functions $U_i^{(m)}$ are specified functions of the position vector $\underline{X}$ in the undeformed configuration, chosen to satisfy the necessary boundary conditions. Furthermore, $q_n(t)$ is a time dependent generalized coordinate of the structural problem, which is required to satisfy the governing equations. The following sections will deal with the derivation of the governing equations for the structural problem. Then, the reduced order models will be derived following a Galerkin approach. Finally, an identification procedure for the parameters of the model as well as the selection of the functions $U_i^{(m)}$ will be reviewed, both based on a commercial finite element code.

## 2.2. Geometric Nonlinear Formulation

In structural dynamic problems related to beams, plates, and shells the von Karman strain definition is often used. However, it is of interest here to study a more general situation. Thus, an arbitrary linearly elastic (i.e., with a linear relation between Green strain and second Piola-Kirchhoff stress tensors) body undergoing large deformations will be considered. The elastodynamic problem will be derived in the undeformed configuration for convenience in the derivation of the reduced order model. In the deformed configuration, the panel is continuously changing; therefore, the basis

functions for the reduced order model would similarly vary in order to satisfy the geometric boundary conditions, thus the reason for choosing the undeformed configuration.

The position vector of a point of the structure will be denoted by $\underline{X}$ in the reference configuration and $\underline{x}$ in the deformed one. Then, the displacement vector is $\underline{u} = \underline{x} - \underline{X}$ and the deformation gradient tensor $\underline{\underline{F}}$ is then defined by its components as

$$F_{ij} = \frac{\partial x_i}{\partial X_j} = \delta_{ij} + \frac{\partial u_i}{\partial X_j} \tag{2.2}$$

where $\delta_{ij}$ denotes the Kronecker delta. Associated with the displacement field $\underline{u}$ are deformations that are characterized by the Green strain tensor $\underline{\underline{E}}$ of components

$$E_{ij} = \frac{1}{2}\left(F_{ki}\,F_{kj} - \delta_{ij}\right) \tag{2.3}$$

In the above equation and in the following ones summation is implied on all repeated indices, unless stated otherwise. The equation of motion of the structure is then given by (e.g. see [26])

$$\frac{\partial}{\partial X_k}\left(F_{ij}\,S_{jk}\right) + \rho_0\, b_i^0 = \rho_0\, \ddot{u}_i \qquad \text{for } \underline{X} \in \Omega_0 \tag{2.4}$$

where $\underline{\underline{S}}$ denotes the second Piola-Kirchhoff stress tensor, $\rho_0$ is the density in the reference configuration, and $\underline{b}^0$ is the vector of body forces, all of which are assumed to depend on the coordinates $X_i$ and are expressed in the reference configuration, where the structure occupies the domain $\Omega_0$. The boundary $\partial\Omega_0$ of the domain, which the structure occupies in the reference configuration, is composed of two parts, $\partial\Omega_0^{\mathrm{t}}$ where tractions are prescribed and $\partial\Omega_0^{\mathrm{u}}$ on which displacements are given. Therefore, the boundary conditions are

$$F_{ij}S_{jk}n_k^0 = t_i^0 \qquad \text{for } \underline{X} \in \partial\Omega_0^t \tag{2.5}$$

and

$$\underline{u} = \underline{0} \qquad \text{for } \underline{X} \in \partial\Omega_0^u \tag{2.6}$$

where the displacement boundary condition assumes the corresponding sides to be fixed, which is usually the case in structural dynamic problems.

In Eqs. (2.4) and (2.5) the vectors $\underline{b}^0$ and $\underline{t}^0$ are obtained by transforming the body forces and tractions in the deformed configuration back to the reference configuration. This transformation is achieved by the following relations

$$\underline{b}^0 = J\underline{b} \quad \text{and} \quad \underline{t}^0 = \left(\frac{da}{dA}\right)\underline{t} \tag{2.7}$$

where $J$ is the Jacobian of the transformation $\underline{x} = \underline{x}(\underline{X})$, i.e. $J = det(\underline{F})$. Also, the area ratio can be obtained from Nanson's formula (see [26])

$$\frac{da}{dA}\underline{n} = J\underline{\underline{F}}^{-T}\underline{N} \tag{2.8}$$

where $\underline{N}$ is the unit normal vector to the boundary $\partial\Omega_0$ at point $\underline{X}$ and $\underline{n}$ is its counterpart in the deformed configuration.

**2.3. Constitutive Relations**

To complete the formulation of the problem, it is necessary to define the material constitutive relations, which stem from the Helmholtz free energy (per unit mass) $H$ defined as

$$H = E - T\,S \tag{2.9}$$

where $\mathsf{E}$ denotes the elastic energy and $\mathsf{S}$ denotes the specific entropy. Then, since the second Piola-Kirchhoff stress tensor and the Green strain rate are work conjugates, using conservation of energy along with Eq. (2.9) one has

$$\rho_0\left(\frac{\partial H}{\partial E_{ij}}\right)_T = S_{ij} \tag{2.10}$$

$$\left(\frac{\partial H}{\partial T}\right)_{E_{ij}} = -S\,. \tag{2.11}$$

In the present investigation, the Duhamel-Neumann form of the Helmholtz free energy (see [27]) will by assumed, i.e.,

$$\rho_0 H = \frac{1}{2} C_{ijkl}\, E_{ij}\, E_{kl} - C_{ijkl}\, \alpha_{kl}\, (T - T_0)\, E_{ij} + f(T, T_0) \tag{2.12}$$

where $\underline{\underline{C}}$ denotes the fourth order elasticity tensor and $\underline{\underline{\alpha}}$ is the second order tensor of thermal expansion. Furthermore, $T_0$ is the reference temperature, and

$$f(T, T_0) = -\rho_0\, C_v\, T_0 \left[\frac{T}{T_0} \ln\left(\frac{T}{T_0}\right) - \frac{T}{T_0} + 1\right] \tag{2.13}$$

in which $C_v$ is the specific heat per unit mass measured in the state of constant strain (see [27]).

Introducing Eqs. (2.12) and (2.13) in Eqs. (2.10) and (2.11) leads to the stress-strain relation

$$S_{ij} = \rho_0 \left(\frac{\partial H}{\partial E_{ij}}\right)_T = C_{ijkl} \left[E_{kl} - \alpha_{kl}\, (T - T_0)\right] \tag{2.14}$$

In the sequel, it will be assumed that the structure is not subjected to thermal effects, thus Eq. (2.14) reduces to

$$S_{ij} = C_{ijkl} E_{kl}\,. \tag{2.15}$$

Finally, the fourth order elasticity tensor $\underline{\underline{C}}$ satisfies the symmetry conditions

$$C_{ijkl} = C_{jikl} = C_{ijlk} = C_{klij} \tag{2.16}$$

and the positive definiteness property

$$A_{ij} C_{ijkl} A_{kl} \geq 0 \tag{2.17}$$

for any second order tensor $\underline{\underline{A}}$.

### 2.4. Structural Reduced Order Model

The previous sections have provided the governing equations of the continuous problem of determining the stress and displacement fields everywhere in the structure considered.

Substitution of Eq. (2.1) in the equation of motion, Eq. (2.4), introduces an error in the solution

$$\xi_i(\underline{X},t)=\sum_{n=1}^{M}\left[\rho_0\ddot{q}_n(t)U_i^{(n)}(\underline{X})-\rho_0 b_i^0-\frac{\partial}{\partial X_k}\left(F_{ij}S_{jk}\right)\right]\neq 0 \tag{2.18}$$

where $S_{jk}$ is given by Eq. (2.15). It is desired to minimize the error $\xi_i$. To this end, following a Galerkin approach the error is forced to be orthogonal to the basis functions $U_i^{(m)}(\underline{X})$ so that

$$\int_{\Omega_0} U_i^{(m)}(\underline{X})\xi_i(\underline{X},t)d\underline{X} \qquad \text{for } m=1,\ldots,M. \tag{2.19}$$

Substitution of Eq. (2.18) into Eq. (2.19) yields the weak form of the equation of motion

$$\begin{aligned}\sum_{n=1}^{M}\left\{\int_{\Omega_0} U_i^{(m)}(\underline{X})\left[\rho_0\ddot{q}_n(t)U_i^{(n)}(\underline{X})-\rho_0 b_i^0-\frac{\partial}{\partial X_k}\left(F_{ij}S_{jk}\right)\right]d\underline{X}\right\} \\ =0 \qquad \text{for } m=1,\ldots,M.\end{aligned} \tag{2.20}$$

The last integral in the previous expression can be expressed as

$$\begin{aligned}&\int_{\Omega_0} U_i^{(m)}\frac{\partial}{\partial X_k}\left(U_i^{(m)}F_{ij}S_{jk}\right)d\underline{X} \\ &\qquad=\int_{\Omega_0}\frac{\partial}{\partial X_k}\left(U_i^{(m)}F_{ij}S_{jk}\right)d\underline{X}-\int_{\Omega_0}\frac{\partial U_i^{(m)}}{\partial X_k}F_{ij}S_{jk}\,d\underline{X}\end{aligned} \tag{2.21}$$

It follows that, by using the Divergence theorem, the previous expression can be simplified into the following

$$\int_{\Omega_0} \frac{\partial}{\partial X_k}\left(F_{ij} S_{jk}\right) d\underline{X} = \int_{\partial\Omega_0^t} U_i^{(m)} t_i^0 \, d\underline{X} - \int_{\Omega_0} \frac{\partial U_i^{(m)}}{\partial X_k} F_{ij} S_{jk} \, d\underline{X}. \tag{2.22}$$

It is left to expand the term $F_{ij}S_{jk}$ from Eq. (2.22). Using Eqs. (2.2), (2.3), and (2.15)

$$F_{ij} S_{jk} = \frac{\partial x_i}{\partial X_j} C_{jklp} \left[ \frac{1}{2} \left( \frac{\partial x_s}{\partial X_l} \frac{\partial x_s}{\partial X_p} - \delta_{lp} \right) \right]. \tag{2.23}$$

Using the fact that $\underline{u} = \underline{x} - \underline{X}$ Eq. (2.23) can be expressed as

$$F_{ij} S_{jk} = \left( \delta_{ij} + \frac{\partial u_i}{\partial X_j} \right) C_{jklp} \left[ \frac{\partial u_l}{\partial X_p} + \frac{1}{2} \frac{\partial u_s}{\partial X_l} \frac{\partial u_s}{\partial X_p} \right]. \tag{2.24}$$

Substitution of Eq. (2.1) yields

$$F_{ij} S_{jk} = \left( \delta_{ij} + q_n \frac{\partial U_i^{(n)}}{\partial X_j} \right) C_{jklp} \left( q_r \frac{\partial U_l^{(r)}}{\partial X_p} + \frac{1}{2} q_r q_w \frac{\partial U_s^{(r)}}{\partial X_l} \frac{\partial U_s^{(w)}}{\partial X_p} \right), \tag{2.25}$$

where summation is implied by repeated indices.

Subsequently, substitution of Eqs. (2.22) and (2.25) into Eq. (2.20) and after some algebraic manipulations, the formulation of the reduced order model is obtained as

$$M_{ij} \ddot{q}_j + D_{ij} \dot{q}_j + K_{ij}^{(1)} q_j + K_{ijl}^{(2)} q_j q_l + K_{ijlp}^{(3)} q_j q_l q_p = F_i \quad \text{for } i=1,\ldots,M \tag{2.26}$$

where

$$M_{mn} = \int_{\Omega_0} \rho_0 U_i^{(m)} U_i^{(n)} d\underline{X} \tag{2.27}$$

$$K_{mn}^{(1)} = \int_{\Omega_0} \frac{\partial U_i^{(m)}}{\partial X_k} C_{iklp} \frac{\partial U_l^{(n)}}{\partial X_p} d\underline{X} \tag{2.28}$$

$$K_{mnp}^{(2)} = \frac{1}{2}\left[ \hat{K}_{mnp}^{(2)} + \hat{K}_{pmn}^{(2)} + \hat{K}_{npm}^{(2)} \right] \tag{2.29}$$

$$\hat{K}^{(2)}_{mnp} = \int_{\Omega_0} \frac{\partial U_i^{(m)}}{\partial X_j} C_{ijkl} \frac{\partial U_r^{(n)}}{\partial X_k} \frac{\partial U_r^{(p)}}{\partial X_l} d\underline{X} \tag{2.30}$$

$$K^{(3)}_{msnp} = \frac{1}{2} \int_{\Omega_0} \frac{\partial U_i^{(m)}}{\partial X_j} \frac{\partial U_i^{(s)}}{\partial X_k} C_{jklw} \frac{\partial U_r^{(n)}}{\partial X_l} \frac{\partial U_r^{(p)}}{\partial X_w} d\underline{X} \tag{2.31}$$

and,

finally,

$$F_m = \int_{\Omega_0} \rho_0 U_i^{(m)} b_i^0 \, d\underline{X} + \int_{\partial\Omega_0^t} U_i^{(m)} t_i^0 \, ds \tag{2.32}$$

The knowledge of the displacements provides a complete solution of the problem and other quantities can then be evaluated. For example, any component of the second Piola-Kirchhoff stress tensor at any point can be expressed as

$$S_{ij} = \bar{S}_{ij} + \hat{S}_{ij}^{(m)} q_m + \tilde{S}_{ij}^{(m,n)} q_m q_n \tag{2.33}$$

where the coefficients $\bar{S}_{ij}$, $\hat{S}_{ij}^{(m)}$, and $\tilde{S}_{ij}^{(m,n)}$ depend only on the point $\underline{X}$ considered.

**2.5. Identification of ROM Parameters**

Formal expressions, as integrals over the undeformed domain of the structure, for the stiffness coefficients $K_{ij}^{(1)}$, $K_{ijl}^{(2)}$, $K_{ijlp}^{(3)}$ were obtained above in the process of deriving Eq. (2.26). Their use would however require a discretization of the domain consistent with the finite element model. To bypass this effort, non-intrusive (or indirect) methods (see [4] for review) have been developed to identify these coefficients based on computed static responses.

The estimation of the mass components $M_{ij}$ and modal forces $F_i$ is achieved as in linear modal models, i.e.

$$M_{ij} = \underline{\psi}^{(i)T} M_{FE} \underline{\psi}^{(j)} \tag{2.34}$$

$$F_i = \underline{\psi}^{(i)T} \underline{F}(t) \tag{2.35}$$

where $M_{FE}$ is the finite element mass matrix and $\underline{F}(t)$ is the excitation vector on the structure.

Next is the determination of the stiffness coefficients $K_{ij}^{(1)}$, $K_{ijl}^{(2)}$, and $K_{ijlp}^{(3)}$. In this regard, note first that the linear coefficients $K_{ij}^{(1)}$ could be determined as in linear modal models, i.e.

$$K_{ij}^{(1)} = \underline{\psi}^{(i)T} K_{FE}^{(1)} \underline{\psi}^{(j)} \tag{2.36}$$

where $K_{FE}^{(1)}$ is the finite element linear stiffness matrix.

Another approach must however be adopted for $K_{ijl}^{(2)}$ and $K_{ijlp}^{(3)}$ as nonlinear stiffness matrices are typically not available from a commercial finite element code. A reduction in this computational effort is obtained by noting the symmetrical role of the indices *j* and *l* in the quadratic terms and *j*, *l*, and *p* in the cubic ones, which indicates that the summations over those indices can be restricted to $p \geq l \geq j$ leading to approximately $M^4/6$ coefficients to be identified.

Two approaches have been proposed to identify the above quadratic and cubic stiffness parameters (and potentially the linear ones as well) from a series of static finite element solutions. The first one relies on prescribing a series of load cases and projecting the induced responses on the basis functions $\underline{\psi}^{(n)}$ to obtain the corresponding generalized coordinates values $q_j^{(p)}$, *p* being the index of the load cases (see [6-7]). Then, introducing these values into Eq. (2.26) for each load case yields

$$K_{ij}^{(1)} q_j^{(p)} + K_{ijl}^{(2)} q_j^{(p)} q_l^{(p)} + K_{ijlr}^{(3)} q_j^{(p)} q_l^{(p)} q_r^{(p)} = F_i^{(p)} \quad , i = 1, ..., M \tag{2.37}$$

where $M$ denotes the number of basis functions (or modes) in the reduced order model. Proceeding similarly for $P$ load cases yields a set of linear algebraic equations for the coefficients $K_{ijl}^{(2)}$ and $K_{ijlp}^{(3)}$, and possibly the linear stiffness coefficients $K_{ij}^{(1)}$ as well, which can be solved in a least squares format to complete the identification of the stiffness parameters.

An alternate strategy has also been proposed (e.g. see [28] and the modification of [12]) in which the *displacements* are prescribed and the required force distributions are obtained from the finite element code. The corresponding modal forces are then evaluated from Eq. (2.35) and a set of equations of the form of Eq. (2.37) is again obtained. Appropriately selecting the displacement fields to be imposed can lead to a particularly convenient identification of the stiffness coefficients. Specifically, the imposition of displacements proportional to the basis function $\underline{\psi}^{(n)}$ only, i.e.

$$\underline{u} = q_n \, \underline{\psi}^{(n)} \qquad \underline{\hat{u}} = \hat{q}_n \, \underline{\psi}^{(n)} \qquad \underline{\tilde{u}} = \tilde{q}_n \, \underline{\psi}^{(n)} \tag{2.38}$$

leads to the 3 sets of equations

$$\begin{aligned} K_{in}^{(1)} q_n + K_{inn}^{(2)} q_n^2 + K_{innn}^{(3)} q_n^3 &= F_i \quad \text{(no sum on } n\text{)} \\ K_{in}^{(1)} \hat{q}_n + K_{inn}^{(2)} \hat{q}_n^2 + K_{innn}^{(3)} \hat{q}_n^3 &= \hat{F}_i \quad \text{(no sum on } n\text{)} \\ K_{in}^{(1)} \tilde{q}_n + K_{inn}^{(2)} \tilde{q}_n^2 + K_{innn}^{(3)} \tilde{q}_n^3 &= \tilde{F}_i \quad \text{(no sum on } n\text{)} \end{aligned} \tag{2.39}$$

in which no sum over the index $n$ is to be understood and for $i = 1, ..., M$. In fact, these 3 sets of equations permit the direct evaluation of the coefficients $K_{in}^{(1)}$, $K_{inn}^{(2)}$, and $K_{innn}^{(3)}$

for all *i*. Repeating this effort for $n$ = 1, ..., $M$ thus yields a first set of stiffness coefficients.

Proceeding similarly but with combinations of two basis functions, i.e.

$$\underline{u} = q_n \, \underline{\psi}^{(n)} + q_m \, \underline{\psi}^{(m)} \quad m \geq n \tag{2.40}$$

and relying on the availability of the coefficients $K_{in}^{(1)}$, $K_{inn}^{(2)}, K_{innn}^{(3)}$ and $K_{im}^{(1)}$, $K_{imm}^{(2)}$, $K_{immm}^{(3)}$ determined above, leads to equations involving the three coefficients $K_{inm}^{(2)}$, $K_{innm}^{(3)}$, and $K_{inmm}^{(3)}$. Thus, imposing three sets of displacements of the form of Eq. (2.40) provides the equations needed to also identify $K_{inm}^{(2)}$, $K_{innm}^{(3)}$, and $K_{inmm}^{(3)}$.

Finally, imposing displacement fields as linear combination of three modes, i.e.

$$\underline{u} = q_n \, \underline{\psi}^{(n)} + q_m \, \underline{\psi}^{(m)} + q_r \, \underline{\psi}^{(r)} \quad r \geq m \geq n \tag{2.41}$$

permits the identification of the last coefficients, i.e. $K_{inmr}^{(3)}$.

Proceeding either with load cases, i.e. Eq. (2.37), or with imposed displacement solutions, Eq. (2.38) and Eqs. (2.40)-(2.41), $M$ coefficients (1 for each value of *i*) can be evaluated for each load/displacement solution. Accordingly, there will be approximately $M^3/6$ such solutions to be determined, each one of which requires a full finite element nonlinear analysis. For an $M$ = 60 basis function reduced order model, there will thus be 36,000 solutions which represents a very significant upfront computational effort.

Note, that the modal forces $F_i$ will in general be affected by the "pull back" operations of Eq (2.7). However, this issue was not addressed here because the displacements of the panels considered in this investigation did not exceed a few thicknesses.

Finally, it remains to discuss the selection of the $q$ values for the imposed displacement fields from Eq. (2.38) and Eqs. (2.40)-(2.41). The first difficulty in the selection of an appropriate $q$ value lies in the numerical precision of the computations. This can be clearly appreciated with an example. Assuming a static displacement proportional to the first mode only, Eq. (2.26) becomes equal to

$$K_{11}^{(1)} q_1 + K_{111}^{(2)} q_1^2 + K_{1111}^{(3)} q_1^3 = F_1 \tag{2.42}$$

In order to solve for the $K_{1111}^{(3)}$ coefficient, division by $q_1^3$ would be required. If $q_1$ is a very "small" number, then there is the risk of amplifying any "noise" that might be present in $F_1$ and/or any of the coefficients $K_{11}^{(1)}$ and $K_{111}^{(2)}$. When the formulation of the finite element code used to create the ROM matches the formulation presented above, i.e. it is based on the reference configuration, then any value for the $q$ coefficients (that is large enough to avoid numerical errors) would be good enough to identify the stiffness coefficients. However, this is not always the case; for example, the geometric nonlinear computations in Nastran are carried out with respect to the deformed configuration. So, if "large" $q$ values are used, then the Lagrangian formulation used to derive the ROM becomes too different from the formulation used by Nastran, and the resulting stiffness coefficients do not represent well the problem. Therefore, there exists a range of values that yield fitting stiffness coefficients. For problems such as simple beams and panels this range has been found to be such that the resulting peak transverse displacement is larger than half beam or panel thicknesses but below one thickness.

**2.6. ROM Basis Selection**

The selection of the basis functions $\underline{\psi}^{(n)}$ represents a key challenge of the reduced order modeling strategy: if the structural response is not well represented within this basis, the corresponding prediction of the reduced order model will in general be

poor. The modes/basis functions needed for a nonlinear problem are certainly expected to include those used for the corresponding linear problem, but others are also anticipated to model the difference in physical behavior induced by the nonlinearity. This situation is particularly clear in shell-like structures subjected to transverse loadings in which the linear response is predominantly transverse while the tangential/in-plane displacement field plays a fundamental role (the "membrane-stretching" effect, see [4,6-7] for discussion) in large motions.

This issue was addressed in [12] through the inclusion in the basis of an additional set of basis functions referred to as *dual modes*, aimed at capturing the membrane stretching effects. The key idea in this approach is to first subject the structure to a series of "representative" static loadings, and determine the corresponding *nonlinear* displacement fields. Then, extract from them additional basis functions, the "dual modes", to append to the linear basis, i.e. the modes that would be used in the linear case. It was argued in [12] that the representative static loadings should be selected to excite primarily the linear basis modes and, in fact, in the absence of geometric nonlinearity (i.e. for a linear analysis) should only excite these modes. i.e. the applied load vectors $\underline{F}_{FE}^{(m)}$ on the structural finite element model should be such that the corresponding linear static responses are of the form

$$\underline{u}^{(m)} = \sum_i \alpha_i^{(m)} \, \underline{\psi}^{(i)} \tag{2.43}$$

which occurs when

$$\underline{F}_{FE}^{(m)} = \sum_i \alpha_i^{(m)} K_{FE}^{(1)} \underline{\psi}^{(i)} \tag{2.44}$$

where $\alpha_i^{(m)}$ are coefficients to be chosen with *m* denoting the load case number. A detailed discussion of the linear combinations to be used is presented in [12] but, in all validations carried out, it has been sufficient to consider the cases

$$\underline{F}_{FE}^{(m)} = \alpha_i^{(m)} K_{FE}^{(1)} \underline{\psi}^{(i)} \quad i = \text{dominant mode} \tag{2.45}$$

and

$$\underline{F}_{FE}^{(m)} = \frac{\alpha_i^{(m)}}{2} K_{FE}^{(1)} \left[ \underline{\psi}^{(i)} + \underline{\psi}^{(j)} \right] \quad i = \text{dominant mode}, \; j \neq i \tag{2.46}$$

where a "dominant" mode is loosely defined as one expected to provide a large component of the panel response to the physical loading. The ensemble of loading cases considered is formed by selecting several values of $\alpha_i^{(m)}$ for each dominant mode in Eq. (2.45) and also for each mode $j \neq i$ in Eq. (2.46). Note further that both positive and negative values of $\alpha_i^{(m)}$ are suggested and that their magnitudes should be such that the corresponding displacement fields $\underline{u}^{(m)}$ range from near linear cases to some exhibiting a strong nonlinearity. Finally, a proper orthogonal decomposition (POD) analysis of each set of "nonlinear responses" is then sequentially carried out to extract the dominant features of these responses which are then selected as dual modes, see [12] for full details.

Validating the appropriateness of these dual modes can be done in particular by demonstrating notable improvements in the projection of snap-shots of the full response on a basis that includes them vs. one that does not, see ensuing section for details. A more visual approach would be to demonstrate that the deflections induced by the loadings of Eqs. (2.45) and (2.46) are similar to those obtained with the physical loading of interest for a broad range of overall magnitude. This effort could be done by plotting the corresponding displacement fields and comparing them. A more expedient strategy

would be to visualize these displacement fields in the *N*-dimensional space, where *N* is the number of degrees of freedom of the structure, and to show that the displacements induced by the physical loading and by the ones of Eqs. (2.45) and (2.46) closely occupy the same part of the space. Since *N* is typically much larger than 3, this space cannot be represented graphically but 2- and 3-dimensional sections of it can be very informative.

To exemplify this situation, consider the clamped-clamped aluminum beam of [21] subjected to both static and dynamic uniform loads. In the absence of symmetry breaking, the transverse displacements are symmetric while the in-plane ones are anti-symmetric. Three representative descriptors of the displacement field are thus the transverse displacements of the beam middle and of another point, taken here as the 1/4 point, and the in-plane displacement of that same off-center point. The magnitude of these displacements is plotted vs. each other in Fig. 2.1 for a series of loadings. First are a uniform static load of varying magnitude, loads of the form of Eq. (2.45) using the first symmetric mode (1-1 Dual) and the second symmetric mode (2-2 Dual), and finally loads in the form of Eq. (2.46) with combinations between the first symmetric mode and the two following ones (1-2 Dual and 1-3 Dual). Also included in Fig. 2.1 are snap shots of the dynamic stationary response to a uniformly distributed load varying randomly in time as a white noise bandlimited process in the frequency range [0,1042Hz] simulating an acoustic loading of overall sound pressure level (*OASPL*) of 143dB.

It is clearly seen from Fig. 2.1 that the displacements induced by the loadings of Eq. (2.45) for the 1-1 Dual and Eq. (2.46) closely occupy the same space as both static and dynamic physical loads and thus they can efficiently be used in the construction of the basis for the representation of the full nonlinear response. Note as well that the displacements induced by the loading of Eq. (2.45) for the 2-2 Dual does not occupy the same space as the other ones and thus is not a good candidate for the basis, i.e. its

inclusion in the basis would not be detrimental but would not be very beneficial either. This observation was indeed expected as mode 2 is not a dominant mode, i.e. it does not or rarely does (in the dynamic case) represent the largest component of the response. This finding confirms the selection strategy of the modes, dominant or not, in Eqs. (2.45) and (2.46). The appropriateness of the above duals extends well beyond the uniform loads, static or dynamic, discussed above; they are appropriate for the class of loading conditions in which the response is dominated by mode 1 (the mode selected as dominant). To confirm this expectation, the displacements induced by triangular loads (zero at the clamp supports and maximum at the beam middle) are also plotted in Fig. 2.1 and they also closely occupy the same space.

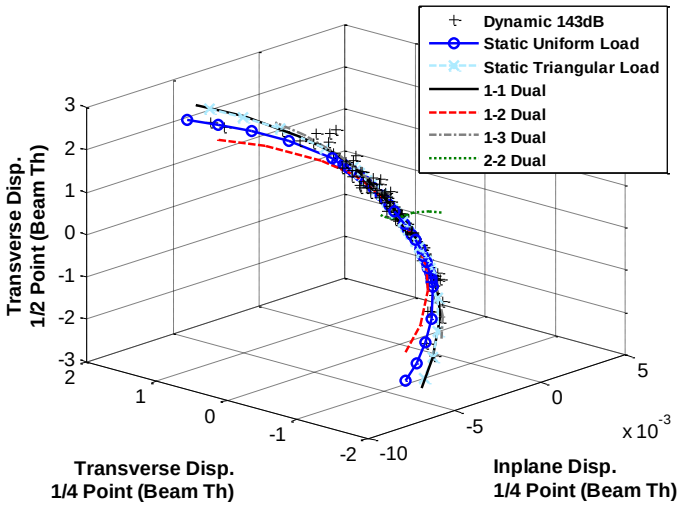


Figure 2.1. Displacements from NX/Nastran at two points of a clamped-clamped beam under various loadings. Transverse displacement at middle point vs. transverse and in-plane displacements at quarter point

# CHAPTER 3

# NEW IDENTIFICATION AND BASIS ENRICHMENT METHODOLOGIES

## 3.1. Introduction

The use of commercial finite element codes enables the straightforward consideration of complex models, allows a broad ensemble of possible elements and capabilities, but also permits a direct transition to the industrial setting where these codes are routinely used. The counterpart of these advantages is the unavailability of certain information and the uncertainty on the formulation implemented in the finite element modeling and response computation. As seen in Chapter 2, the developed reduced order models are parametric, i.e. the form of the equations governing the generalized coordinates is fixed, linear in mass and damping operators with a stiffness operator exhibiting linear, quadratic, and cubic terms in all combinations of generalized coordinates as derived from finite deformation elasticity in the reference configuration. One of the key challenges involved in the ROM is accordingly the estimation of the parameters of the model from a set of finite element results. As seen in the previous chapter, current methods for this identification are based on computed static responses for specified loads [6-7], or in reverse, necessary loads to achieve a particular displacement (see [12,28]). This strategy becomes computationally expensive as the size of the model increases as it is proportional to the third power of the number of modes retained. Therefore, a new strategy for the identification of these coefficients, which makes use of the tangent stiffness matrix of the structure, will be presented and validated in this chapter. It is proportional to the square of the number of modes and thus provides a significant reduction in the computational cost associated with the model building.

A second challenge involved in complex structural model is the selection of the basis to represent well and “economically” (with a small basis) the displacements. In this

regard, it will be shown that the modes obtained from the tangent stiffness matrix, computed at certain displacement configurations, form an excellent enrichment to capture the geometric nonlinearities in addition to the modes of the linear structure and the *dual modes*.

### 3.2. Identification Methodology for Complex Models

An alternate identification approach is proposed here, which relies on the availability of the final *tangent stiffness matrix* for each load or imposed displacement case. The advantage of this approach is that an $M \times M$ matrix is obtained for each solution and thus a reduction of the computational effort to $O\left(M^2\right)$ is expected. The specific details of this novel algorithm are developed below.

The *iu* component of the reduced order tangent stiffness matrix is derived from the cubic stiffness operator of Eq. (2.26) as

$$\begin{aligned} K_{iu}^{(T)} &= \frac{\partial}{\partial q_u}\left[K_{ij}^{(1)} q_j + K_{ijl}^{(2)} q_j q_l + K_{ijlp}^{(3)} q_j q_l q_p\right] \\ &= K_{iu}^{(1)} + \left[K_{iju}^{(2)} + K_{iuj}^{(2)}\right] q_j + \left[K_{ijlu}^{(3)} + K_{ijul}^{(3)} + K_{iujl}^{(3)}\right] q_j q_l \end{aligned} \tag{3.1}$$

It is proposed here to determine the stiffness coefficients $K_{ij}^{(1)}$, $K_{ijl}^{(2)}$, and $K_{ijlp}^{(3)}$ by imposing the matching, for a series of deformed configurations, of the reduced order tangent stiffness matrix with the projection on the basis of its finite element counterpart $\hat{K}^{(T)}$. That is,

$$K^{(T)}(\underline{q}^{(p)}) = \Psi^T \hat{K}^{(T)}(\underline{u}^{(p)})\,\Psi \quad \text{where} \quad \underline{u}^{(p)} = \Psi \underline{q}^{(p)} \tag{3.2}$$

for a series of $p = 1, ..., P$ deformed configurations. In the above equations, the subscript $^T$ denotes the operation of matrix transposition and $\Psi$ is the modal matrix

$$\Psi = \left[ \underline{\psi}^{(1)} \; \underline{\psi}^{(2)} \ldots \underline{\psi}^{(M)} \right] \tag{3.3}$$

The deformed configurations $\underline{u}^{(p)} = \Psi \underline{q}^{(p)}$ selected here are those of the imposed displacement scheme, Eq. (2.38) and Eqs. (2.40)-(2.41). Consider first the situation in which the imposed displacement is along a single basis function, i.e. $\underline{u} = q_j \; \underline{\psi}^{(j)}$. The corresponding ROM tangent stiffness matrix can then be written as (no sum on *j*)

$$K_{iu}^{(T)} = K_{iu}^{(1)} + \left[ K_{iju}^{(2)} + K_{iuj}^{(2)} \right] q_j + \left[ K_{ijju}^{(3)} + K_{ijuj}^{(3)} + K_{iujj}^{(3)} \right] q_j^2 \tag{3.4}$$

Since the elements $K_{ijl}^{(2)}$ and $K_{ijlp}^{(3)}$ were assumed to be zero unless $p \geq l \geq j$, the above equation is equivalent to

$$\begin{aligned}
K_{iu}^{(T)} &= \left[ \Psi^T \hat{K}^{(T)} \Psi \right]_{iu} = K_{iu}^{(1)} + K_{iju}^{(2)} q_j + K_{ijju}^{(3)} q_j^2 \qquad j < u \\
K_{iu}^{(T)} &= \left[ \Psi^T \hat{K}^{(T)} \Psi \right]_{iu} = K_{iu}^{(1)} + 2 K_{iuu}^{(2)} q_u + 3 K_{iuuu}^{(3)} q_u^2 \quad j = u \\
K_{iu}^{(T)} &= \left[ \Psi^T \hat{K}^{(T)} \Psi \right]_{iu} = K_{iu}^{(1)} + K_{iuj}^{(2)} q_j + K_{iujj}^{(3)} q_j^2 \qquad j > u
\end{aligned} \tag{3.5}$$

from which the coefficients $K_{ijl}^{(2)}$, $K_{ijjl}^{(3)}$, and $K_{ijll}^{(3)}$ can be estimated if it is assumed that the linear stiffness coefficients are obtained from Eq. (2.36).

To complete the identification of the reduced order model, it remains to evaluate the coefficients $K_{ijlu}^{(3)}$ for $j \neq l$, $j \neq u$, and $u \neq l$. They can be evaluated from the knowledge of $K_{iu}^{(T)}$ corresponding to a displacement field which involves both basis functions *j* and *l*, i.e. of the form of Eq. (2.40). Then, $K_{iu}^{(T)}$ is given by Eq. (4.1) for which no summation on *j* and *l* applies. Specifically, for $u > l > j$, one has

$$K_{iu}^{(T)} = \left[\Psi^T \hat{K}^{(T)} \Psi\right]_{iu}$$
$$= K_{iu}^{(1)} + \left[K_{iju}^{(2)}\, q_j + K_{ilu}^{(2)}\, q_l\right] + \left[K_{ijlu}^{(3)}\, q_j\, q_l + K_{ijju}^{(3)}\, q_j^2 + K_{illu}^{(3)}\, q_l^2\right] \tag{3.6}$$

in which all terms are known except $K_{ijlu}^{(3)}$.

Note in the above procedure, that no combination of three modes, as in Eq. (2.41), is necessary and thus, as suggested at the beginning of this section, the number of deformed configurations to consider is only of order $O\left(M^2\right)$, it is indeed $2M + M(M-1)/2$. To corroborate this analysis, shown in Table 4.1 are the number of static solutions required for the new, tangent stiffness-based identification scheme and the imposed displacement force-based method. These results clearly show the reduction in computational effort necessary which converges to *M*/3 for large *M*.

However, the CPU time required in the construction of the tangent stiffness matrix and its transformation to the modal tangent stiffness matrix ought to be taken into account to perform a fair comparison. For the 9-bay panel considered in the ensuing sections and with 96,156 degrees of freedom, the CPU time required to produce a static solution with tangent stiffness matrix was found to be approximately 1.5 times the time to obtain the same solution without computing the tangent stiffness matrix. The combination of these factors suggests that the net reduction in computational time implied by the tangent stiffness algorithm is a factor of the order of *M*/4 to *M*/5 for large *M*.

Table 3.1. Number of Static Solutions Needed for ROM Identification

| Number of Modes | Imposed Displ. Tangent Stiffness ID Method | Imposed Displ. Force ID Method |
|---|---|---|
| 15 | 135 | 815 |
| 25 | 350 | 3,275 |
| 75 | 2,950 | 76,075 |

A limited set of comparisons were performed, on the 9-bay panel described below and on a flat clamped-clamped beam, to assess whether the stiffness coefficients

identified by the imposed displacement methods based on the forces and the tangent stiffness matrix were noticeably different, and/or they led to reduced order model with different predictive capabilities. While some, typically small, differences in the coefficients were found, the two methods led to reduced order model predictions that were very close to each other suggesting that the methods provide an equal accuracy in estimating the stiffness coefficients.

Finally, another advantage of this method lies in the numerical accuracy issue discussed at the end of Chapter 2.4. Indeed, since no combination of three modes is needed the largest power in the identification is quadratic. Therefore, smaller values of $q$ can be used without bringing a problem of accuracy such as the one described in that chapter.

### 3.3. ROM Basis for Complex Models

The dual mode construction from the previous chapter has been very successfully applied to various beam and plate structural models, e.g. see [9, 12, 17-25], to capture the nonlinear interaction, both static and dynamic, between transverse and "in-plane" motions. Its application to the 9-bay panel of [29] did provide a basis that represented much better the nonlinear response, especially in the in-plane (tangential) direction, than the one based on the linear modes but yet not well enough to obtain an accurate reduced order model prediction of the full order Nastran results. This observation suggested that the load cases of Eq. (2.45) and (2.46) do provide a very valuable platform to identify the nonlinear effects, but it also demonstrated that other, smaller components, are also present.

A potential solution to capture these components of the response would be to expand the summation in Eq. (2.46) to include more than 2 modes. Such an effort would however likely bring many static solutions to be determined and analyzed. If such modes

were indeed included, it would be expected that the coefficients $\alpha_i^{(m)}$ multiplying them would be small, reflecting the small discrepancies observed. Then, the changes in the displacement fields $\underline{u}^{(m)}$ would probably also be small and thus may be captured in a perturbation-like format. Central to such an analysis would be the finite element tangent stiffness matrix $\hat{K}^{(T)}(\underline{u}^{(m)})$ evaluated at the displacements $\underline{u}^{(m)}$ induced by the loadings of Eqs. (2.45) and (2.46).

The above discussion suggests that this tangent stiffness matrix does also contain valuable basis information. To extract it, it was proposed to first proceed with a generalized eigenvector analysis of each matrix $\hat{K}^{(T)}(\underline{u}^{(m)})$ yielding the vectors $\underline{\phi}_j^{(m)}$ such that

$$\hat{K}^{(T)}(\underline{u}^{(m)})\,\underline{\phi}_j^{(m)} = \lambda_j^{(m)} M_{FE}\underline{\phi}_j^{(m)}. \tag{3.7}$$

Next, the eigenvectors $\underline{\phi}_j^{(m)}$ that are most significantly excited by the loading were retained and projected on the basis consisting of the linear and dual modes. Finally, a POD analysis of the ensemble of eigenvector projections was carried out to extract the new information in the eigenvectors $\underline{\phi}_j^{(m)}$. The basis functions thus retained to complement the linear and dual modes are referred to in the sequel as "tangent dual modes".

A somewhat similar argument to the one developed above has recently been proposed [30] for enriching the linear modes by eigenvectors of the second derivative of the tangent stiffness matrix evaluated at the undeformed configuration.

# CHAPTER 4

# VALIDATION ON A MIDDLE COMPLEXITY MODEL

## 4.1. Model Description

The 9-bay panel of [29] modeled within Nastran was considered for the validation of the novel (i) stiffness coefficients identification and (ii) basis selection strategy. This panel is a section of the sidewall fuselage panel studied in [31], see Fig. 4.1. The finite element model of the 9-bay panel, shown in Fig. 4.2, has a total of 96,156 degrees of freedom. The dimensions of the skin panel are 58.11in by 25.06in, and it is subdivided into nine bays by a riveted frame and longeron substructure. Each bay measures 18.75in by 7.5in between rivet lines. The thickness of the skin panel and frame substructure is of 0.05in and of 0.04in for the longeron substructure. The finite element model consists of 4-node plate elements. Furthermore, beam elements were used to model the rivets that join the skin panel to the frame and longeron substructures. The material properties are shown in Table 4.1.The edges of the skin panel are simply supported.

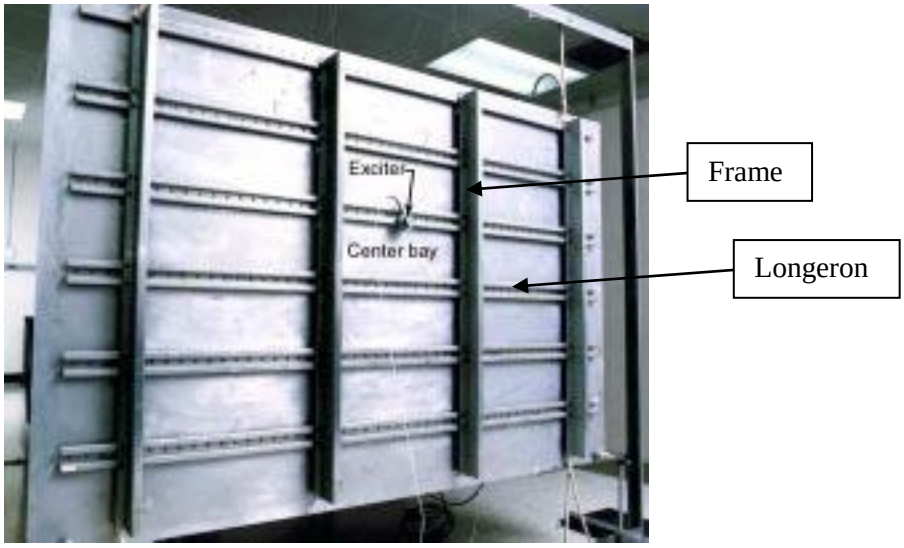


Figure 4.1. Sidewall fuselage panel taken from [31]. 9-bay panel is a section of this structure.

Table 4.1. 9-Bay Panel Material Properties

| | |
|---|---|
| Young's Modulus | $10.5\times10^{6} psi$ |
| Poisson's Ratio | 0.33 |
| Density | $2.614\times10^{-4} lb_f\text{-}s^2/in^4$ |

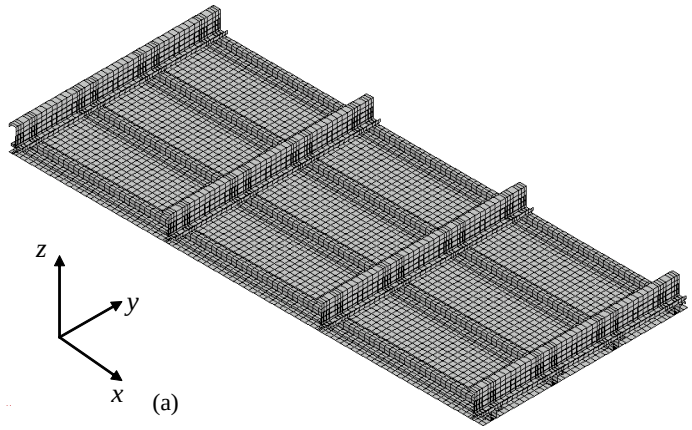


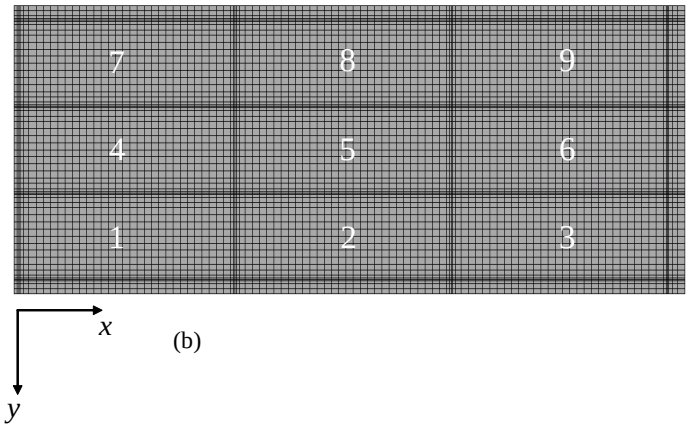


Figure 4.2. Finite element model of the 9-bay fuselage sidewall panel, (a) isometric view, (b) top view.

### 4.2. Reduced Order Model Basis Selection of the 9-Bay Panel

A series of 10 uniform pressures were applied to the skin panel, and the corresponding NX/Nastran nonlinear static responses (SOL 106) were obtained to provide a sample of "snapshots" for the reduced order model construction. The

magnitudes of the pressures ranged from 0.015psi to 0.6 psi, which led to peak transverse deflections (direction normal to the skin panel) from 0.1 skin panel thicknesses to 2.5 thicknesses. A reduced order basis formed from 51 linear modes, 13 dual modes, and 18 tangent dual modes was built to represent the displacements.

The appropriateness of a basis to model the response can be assessed by the representation error

$$\varepsilon_{rep} = \frac{\left\| \underline{u} - \underline{u}_{proj} \right\|}{\left\| \underline{u} \right\|} \tag{4.1}$$

where $\underline{u}$ is the static displacement field computed by the finite element code and $\underline{u}_{proj}$ is its projection on the selected basis. The representation error $\varepsilon_{rep}$ was plotted as a function of the number of retained linear modes and the modes at which noticeable drops in this error occurred were recorded. This process led to the identification of a set of 51 linear modes, with natural frequencies ranging from 68Hz to 900Hz. The resulting transverse displacement (T3 or *z* component) representation errors, for the 2.5 thickness level case, were equal to 0.44% for the skin panel and 0.6% for the frame-longeron substructure. Furthermore, the representation errors for the in-plane component along the length of the skin panel (T1 or *x* component) were equal to 61% for the skin panel and 2% for the frame-longeron substructure. The errors for the component along the width (T2 or *y* component), which is the dominant "in-plane" component, were equal to 104% for the skin panel and 10% for the frame-longeron substructure, see Table 4.2 for the skin panel values.

The large errors for the in-plane components are fully expected and result from the membrane stretching that occurs when the behavior of the panel is in the nonlinear regime, and which the linear basis cannot capture. A comparison of these representation errors for the skin panel and the frame-longeron substructure suggests that the

nonlinearity is dominant in the skin panel with the frame-longeron substructure behaving approximately linearly.

The 10 linear modes with the largest modal components, i.e. modes 1, 5, 7, 9, 13, 15, 16, 25, 28 and 46, were used to construct the dual modes. Since the modal component of mode 1 is much larger than the other ones (by a factor of at least 10) for all static responses analyzed, it was considered as the only dominant mode in Eqs. (2.45) and (2.46). The POD-based dual mode construction procedure highlighted in Chapter 2 (see [12] for full details) was performed for the data obtained for mode 1 alone and each of the 9 combinations of mode 1 and another of the 10 largest responding modes. In each of these 10 situations, 12 different loading factors $\alpha_i^{(m)}$ were used, half positive and half negative, and leading to peak deflections ranging from 0.12 to approximately 0.6 skin panel thicknesses. The remainders of these 120 deflections, after projection on the 51 linear modes identified above, were analyzed by POD. The POD eigenvectors with largest eigenvalues and leading to a reduction of the representation error of the T2 component (i.e., the dominant in-plane component) were selected as dual modes. Thirteen dual modes were identified in this manner. The representation error of the resulting 64-mode model (51 linear modes and 13 dual modes), shown in Table 4.2, indicates a very sharp drop in the T2 direction confirming the appropriateness of the dual modes. Another perspective on the adequacy of the dual modes is provided by the 3-dimensional section of the *N*-dimensional space of displacements shown in Fig. 4.3, which focuses on the transverse displacements at the middle points of the center bay and of the corner and side bays (bays 1 and 2, see Fig. 4.2b) and the T2 displacement at these latter points obtained from a nonlinear static analysis. Clearly, the duals shown closely occupy the same space as the physical uniform loading, as seen in connection with the beam model, see Fig. 2.1.

Unlike the uniform pressure loading, the loadings used to obtain the 1-1 and 1-16 duals have dominant components on bays 2, 5, and 8. For this reason, the "1-1 Dual" and the "1-16 Dual" curves are much closer to the "Static Uniform Pressure" curve in bay 2 than in bay 1. On the other hand, the 1-13 dual loading has a dominant component on bay 5 and its T2 component is dominant near the long edges of the skin panel.

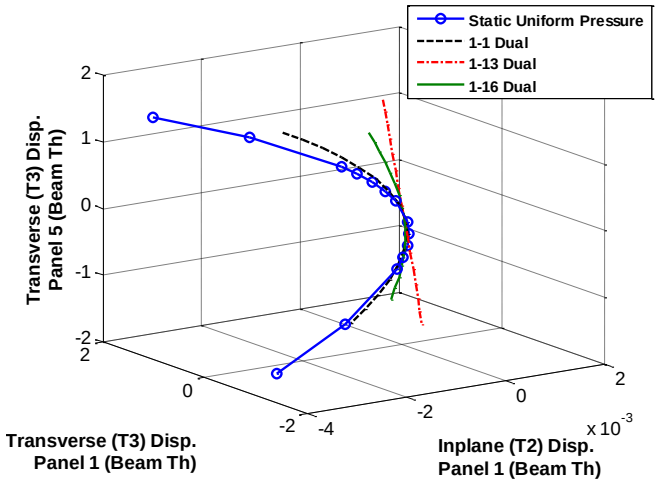


(a)

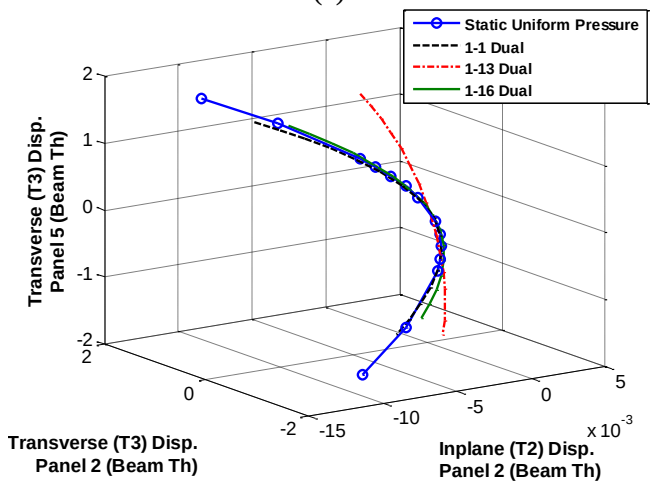


(b)

Figure 4.3. Displacements from NX/Nastran at two points of the 9-bay panel under various loadings, transverse displacements at the middle point of the center bay and transverse and in-plane (T2) displacement at the middle point of: a) bay 1 and b) bay 2.

The basis was then enriched with the tangent duals, obtained from a POD analysis of the eigenvectors of the tangent stiffness matrix computed at peak

displacement levels ranging from 0.003 to 0.015 skin panel thicknesses. It was found that more valuable information, for the representation of the displacement field, could be extracted from the tangent stiffness modes if they were obtained at smaller loading levels than the levels used to compute the dual modes. A possible explanation may be related to the way the nonlinear stiffening affects the various substructures. Indeed, the nonlinear stiffening is more significant in the skin panel than in the frame substructure, since the latter is cantilevered (see Fig. 4.2). Therefore, for large loading factors the motion of the frame in the tangent stiffness modes becomes dominant. However, the objective of the tangent duals is to improve the representation of the in-plane component of the skin panel.

Loadings proportional to combinations of the first mode and modes 5, 13, 15, and 16 were used and only the first mode, i.e. the one with largest "modal force", of each matrix was computed. This process led to 18 tangent dual modes being selected as contributing most to the T2 representation. The final in-plane representation errors for the 82-mode basis at the 2.5 thickness loading level are shown in Table 4.2 and indicate a further drop in the T2 direction as compared to the 64-mode model including only linear and dual modes.

### 4.3. Static Validation on the 9-Bay Panel

#### 4.3.1. Uniform Loading

Having completed the reduced order model construction, it was desired to assess its predictive capability in comparison with NX/Nastran. To this end, a loading of 0.6 psi, leading to a 2.5 thicknesses maximum skin panel deflection, was considered and shown in Figs. 4.4-4.11 are contour plots of the different displacement components. Note the excellent matching, both qualitatively and quantitatively, between reduced order model and NX/Nastran results. The norm errors of the former in comparison to the latter were

1.2% for the transverse (T3) component, 3.3% for the in-plane T2 component, 36% for the other, smaller, in-plane component T1, and 4.3% for the in-plane magnitude (see also Table 4.2). Clearly, the matching of the dominant components, T3 and T2, is very good. On the other hand, the relative error of the T1 component is still rather large but it is clear from Figs. 4.6-4.11 that this component is much smaller than its T2 counterpart (as stated above). The summary of representation and prediction errors for the skin panel presented in Table 4.2 highlights the benefits of each set of basis functions: linear modes, dual modes, and tangent dual modes. Note as well that the final prediction error is only slightly larger than its prediction counterpart suggesting that the model has indeed reached a converged solution near the optimum projection point of the Nastran displacements on the basis.

The prediction errors for the frame substructure were equal to 1.3% for T3, 21% for T1, 2% for T2, and 19% for the magnitude of the in-plane displacements.

Table 4.2. Summary of Representation and Prediction Errors - Skin Panel.

| | 51-Mode Rep. Error | 64-Mode Rep. Error | 82-Mode Rep. Error | 82-Mode Prediction Error |
|---|---|---|---|---|
| T3 | 0.44% | 0.35% | 0.3% | 1.2% |
| In-Plane Mag. | 90% | 6.8% | 3.4% | 4.3% |
| T2 | 104% | 6.4% | 1.8% | 3.3% |
| T1 | 61% | 31% | 31% | 36% |

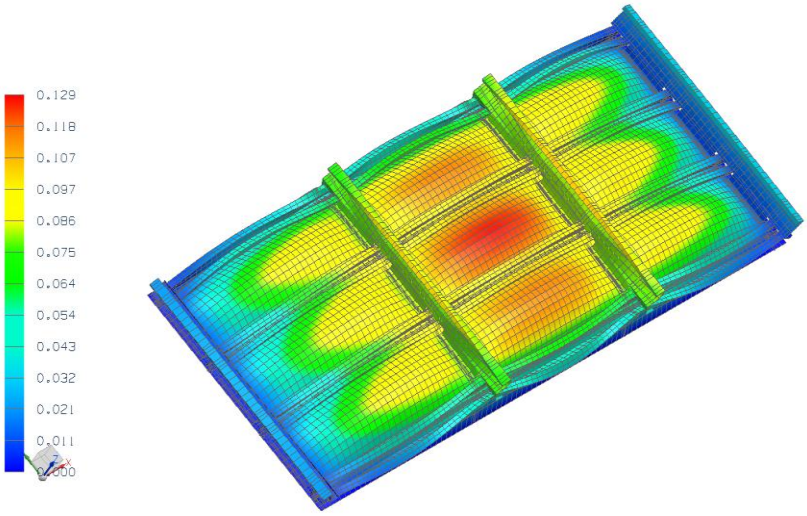


Figure 4.4. Translational displacement magnitude induced by a uniform pressure of 0.6 psi, NX/Nastran.

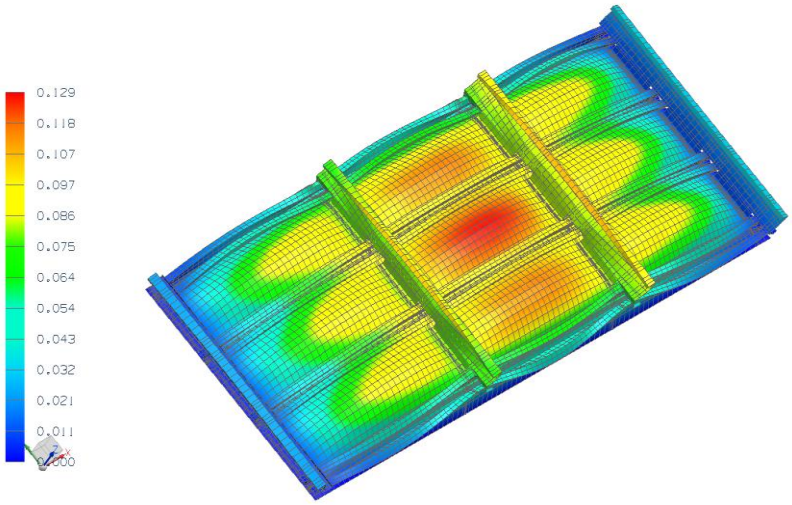


Figure 4.5. Translational displacement magnitude induced by a uniform pressure of 0.6 psi, 82-mode ROM.

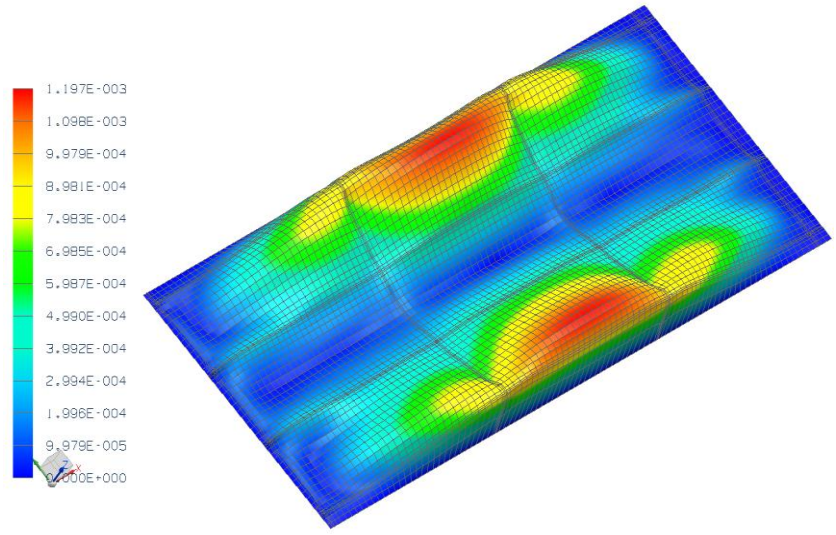


Figure 4.6. Magnitude of the in-plane displacement induced by a uniform pressure of 0.6 psi, skin panel only, NX/Nastran.

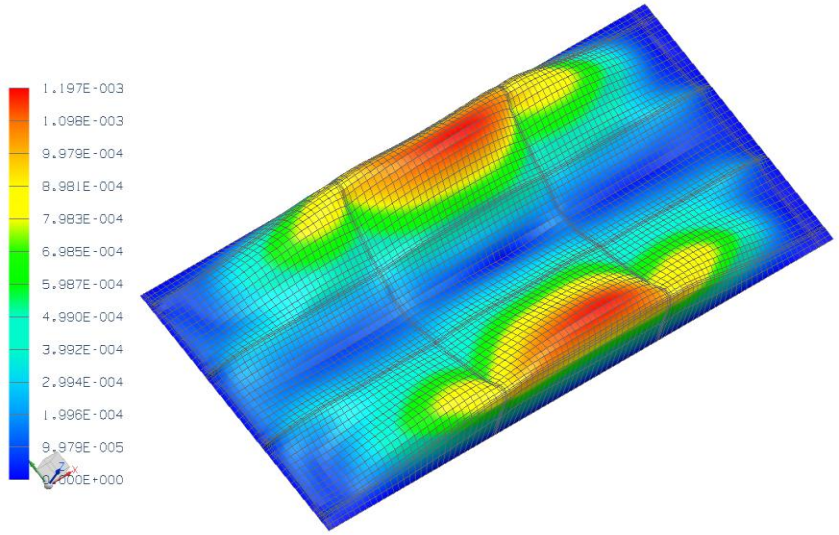


Figure 4.7. Magnitude of the in-plane displacement induced by a uniform pressure of 0.6 psi, skin panel only, 82-mode ROM.

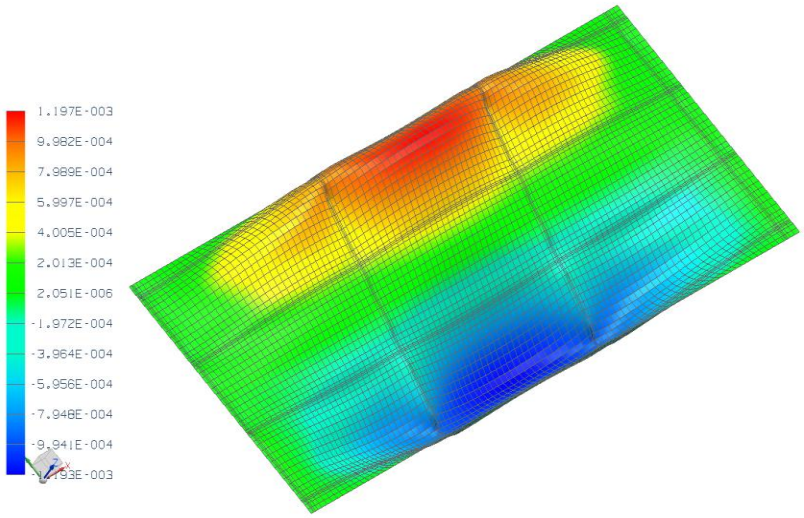


Figure 4.8. In-plane displacement along T2 induced by a uniform pressure of 0.6 psi, skin panel only, NX/Nastran.

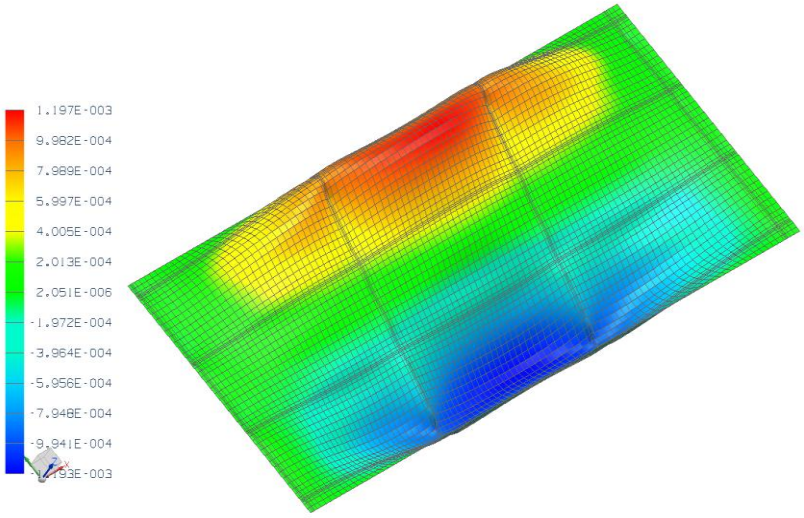


Figure 4.9. In-plane displacement along T2 induced by a uniform pressure of 0.6 psi, skin panel only, 82-mode ROM.

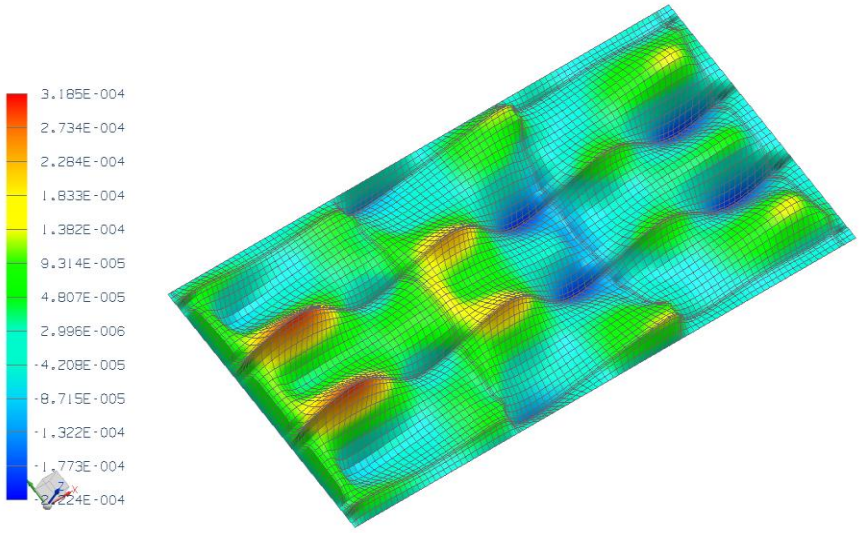


Figure 4.10. In-plane displacement along T1 induced by a uniform pressure of 0.6 psi, skin panel only, NX/Nastran.

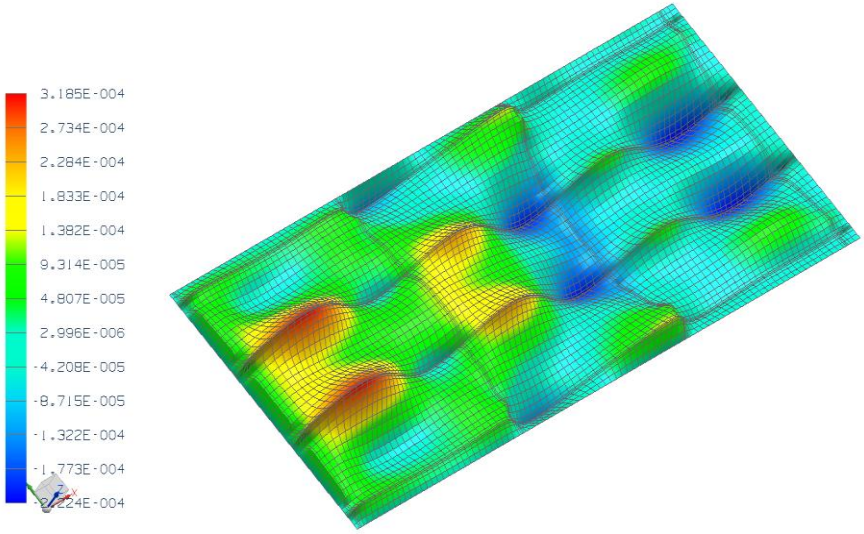


Figure 4.11. In-plane displacement along T1 induced by a uniform pressure of 0.6 psi, skin panel only, 82-mode ROM.

A peak displacement of 2.5 thicknesses is usually considered to be well within the nonlinear range for a clamped-clamped panel. To confirm this assessment, a linear NX/Nastran analysis was carried out for the same loading condition and shown in Figs. 4.12-4.15 are the resulting T3, T2, and T1 components of the skin panel displacements. Note the dramatic difference in the T2 displacements between linear and nonlinear

analyses (Figs. 4.8 and 4.14). Fewer differences in the shape of the T3 components are observed, but the peak magnitude is notably reduced in the nonlinear case, 2.5 thicknesses as compared to 5 thicknesses in the linear case, as expected.

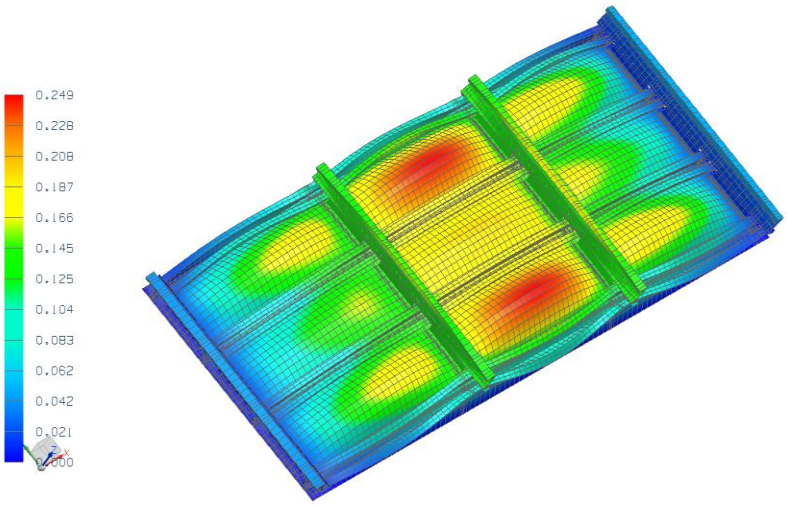


Figure 4.12. NX/Nastran linear response induced by a uniform pressure of 0.6 psi, translational displacement magnitude.

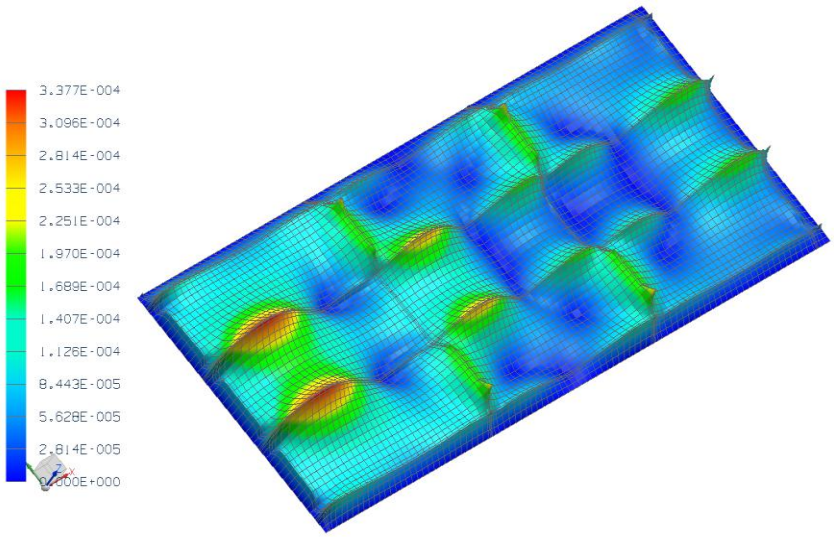


Figure 4.13. NX/Nastran linear response induced by a uniform pressure of 0.6 psi, in-plane component magnitude.

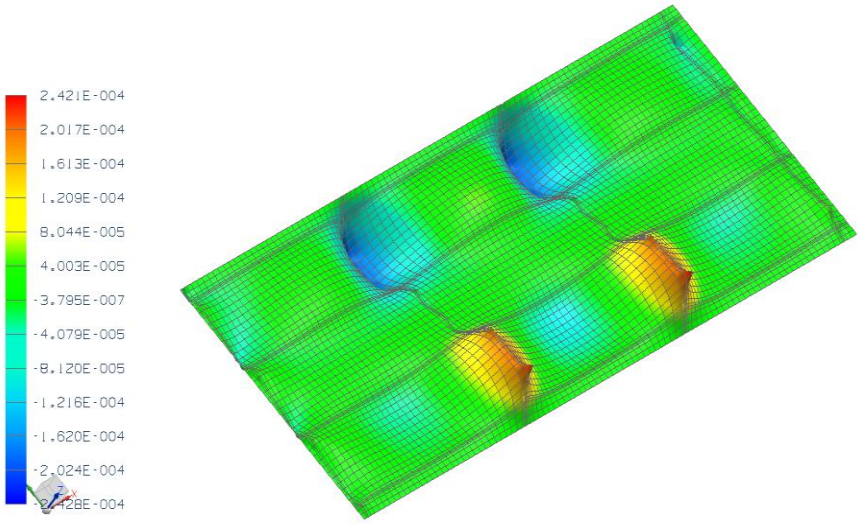


Figure 4.14. NX/Nastran linear response induced by a uniform pressure of 0.6 psi, in-plane component along T2.

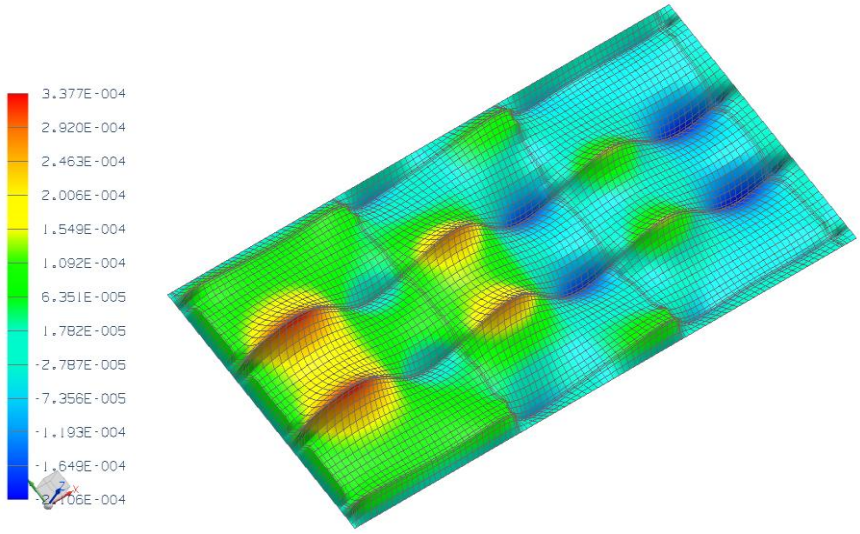


Figure 4.15. NX/Nastran linear response induced by a uniform pressure of 0.6 psi, in-plane component along T1.

### 4.3.2. Non-Uniform Loading

The modes of the 82-mode ROM were selected to reduce the representation errors from a series of uniform loading cases. In this light, it was desired to assess this model in a non-uniform loading case. To this end, the nonlinear static response due to a non-uniform pressure on the skin panel, varying as a function of $x$ and uniform with

respect to *y*, was computed. Shown in Fig. 4.16 is the spatial variation of the loading with respect to *x*. This loading led to a peak transverse displacement of 2.5 skin panel thicknesses.

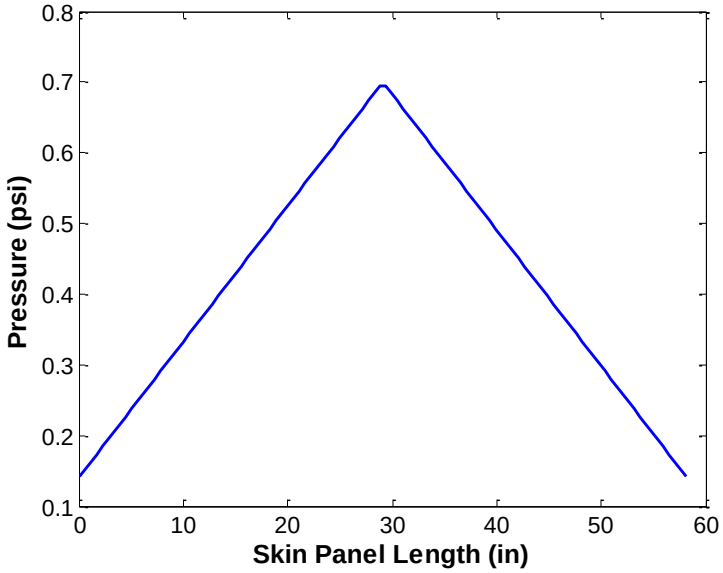


Figure 4.16. Non-uniform pressure variation along the skin panel.

Shown in Table 4.3 are the prediction errors for the skin panel transverse and in-plane degrees-of-freedom, the matching with NX/Nastran is excellent. The prediction errors for the frame substructure were equal to 1% for T3, 17% for T1, 2.6% for T2, and 15% for the magnitude of the in-plane displacements. Shown in Figs. 4.17-4.24 are contour plots of the different displacement components.

Table 4.3. Summary of Prediction Errors - Skin Panel.

| | 82-Mode Prediction Error |
|---|---|
| T3 | 0.9% |
| In-Plane Mag. | 2.5% |
| T2 | 2.5% |
| T1 | 7% |

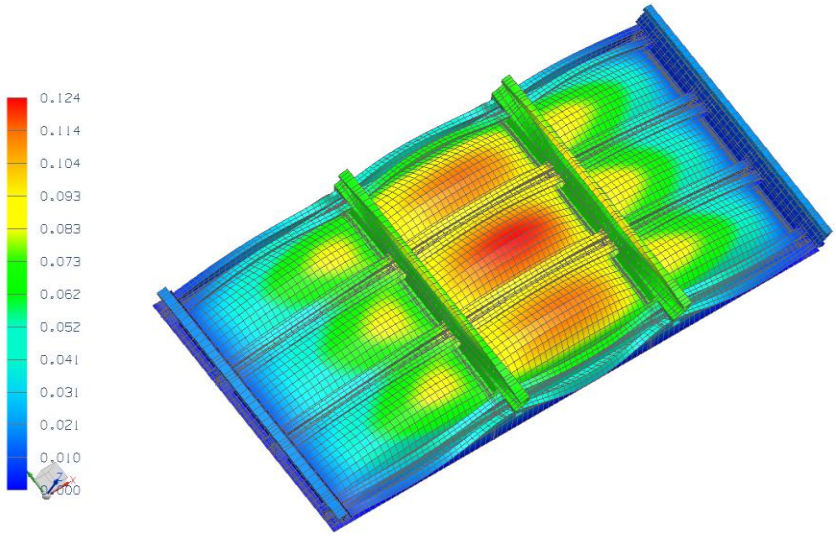


Figure 4.17. Translational displacement magnitude induced by a non-uniform, NX/Nastran.

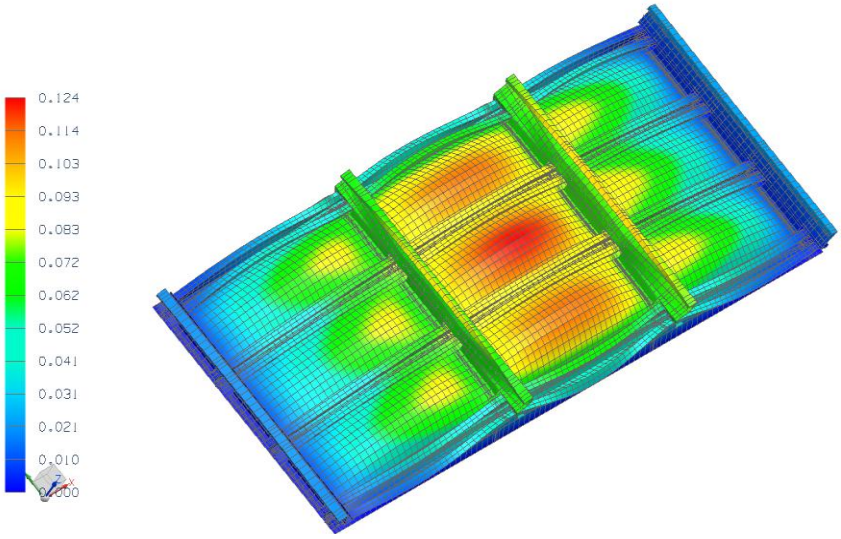


Figure 4.18. Translational displacement magnitude induced by a non-uniform, 82-mode ROM.

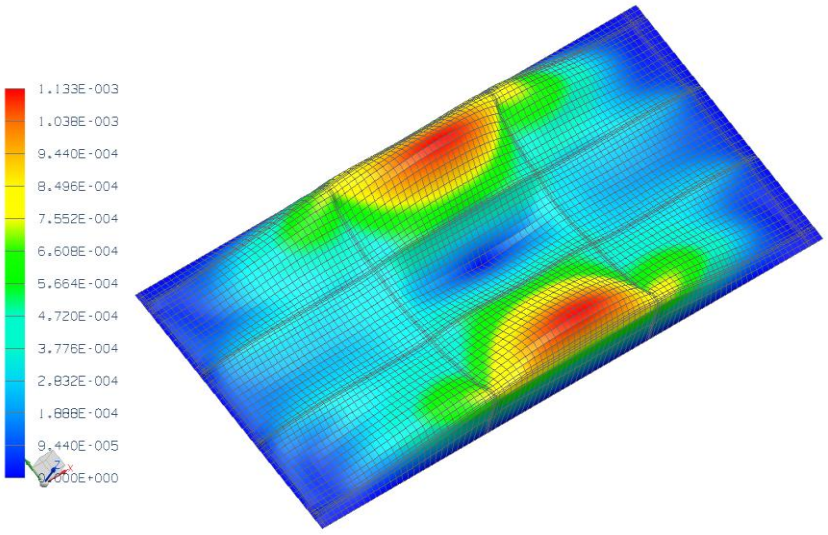


Figure 4.19. Magnitude of the in-plane displacement induced by a non-uniform, skin panel only, NX/Nastran.

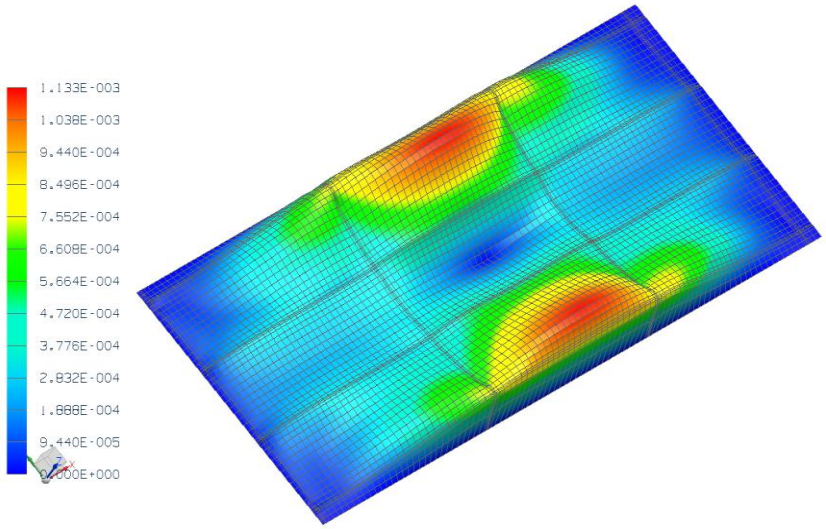


Figure 4.20. Magnitude of the in-plane displacement induced by a non-uniform, skin panel only, 82-mode ROM.

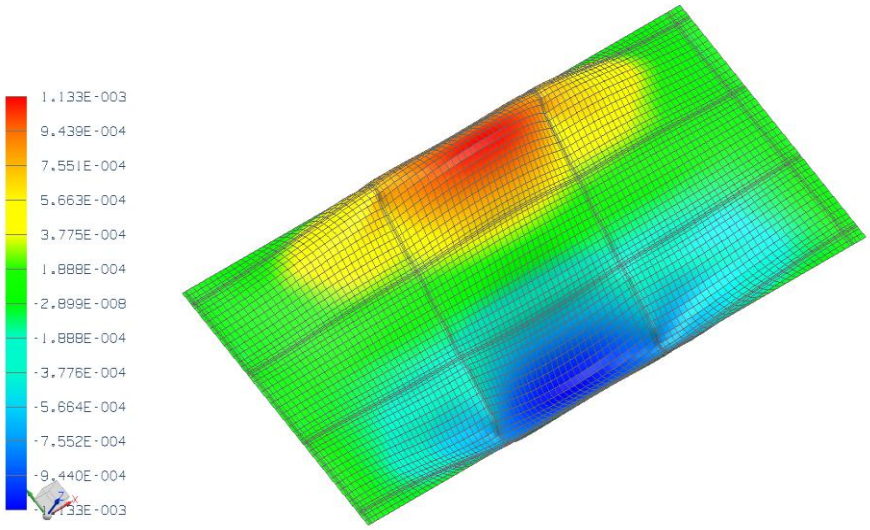


Figure 4.21. In-plane displacement along T2 induced by a non-uniform, skin panel only, NX/Nastran.

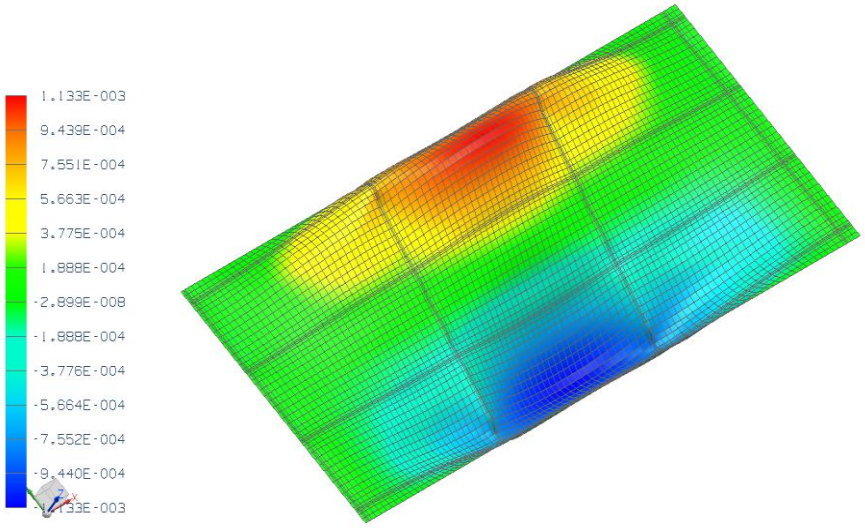


Figure 4.22. In-plane displacement along T2 induced by a non-uniform, skin panel only, 82-mode ROM.

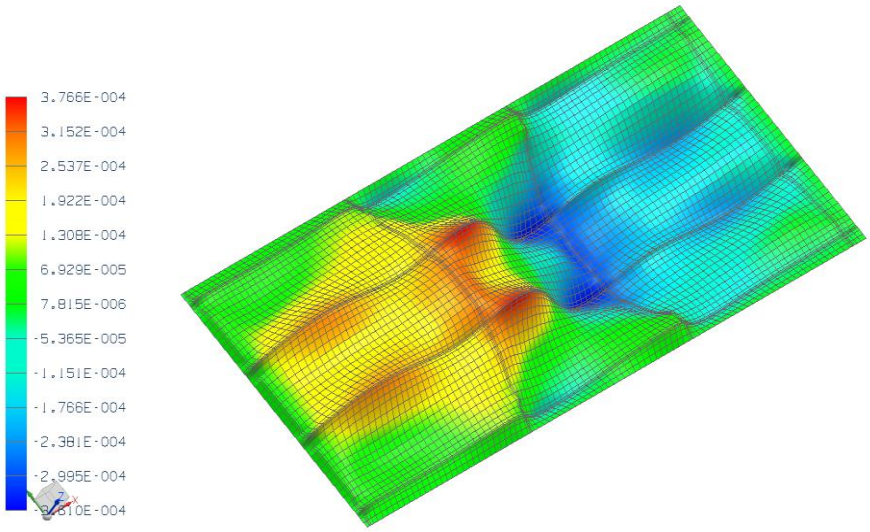


Figure 4.23. In-plane displacement along T1 induced by a non-uniform, skin panel only, NX/Nastran.

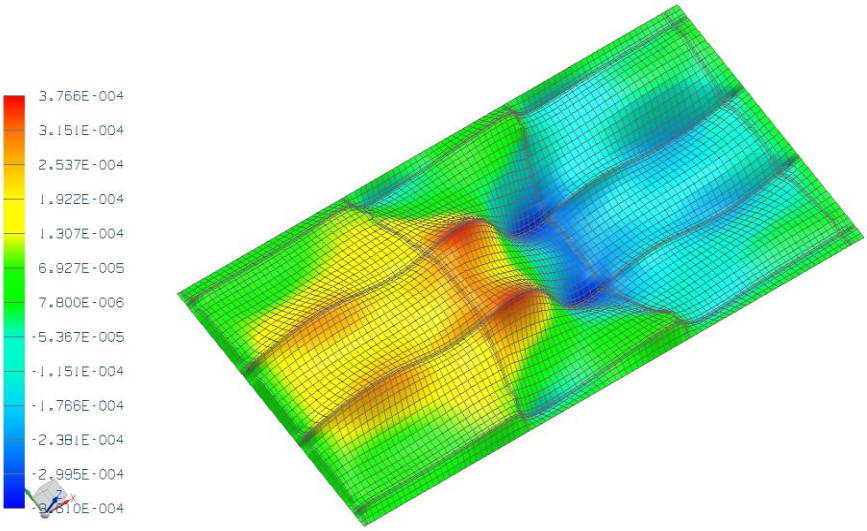


Figure 4.24. In-plane displacement along T1 induced by a non-uniform, skin panel only, 82-mode ROM.

### 4.4. Dynamic Validation on the 9-Bay Panel of Conventional ROM

The 9-bay panel was subjected to a uniform pressure on its top surface varying randomly in time as a white noise band-limited process in the frequency range [0,500]Hz to simulate an acoustic loading. The acoustic excitation consisted of overall sound pressure levels (*OASPL*) of 136dB and 146dB. Furthermore, to permit a close comparison between the full finite element and ROM results, a simple Rayleigh damping model was adopted, i.e. for which the damping matrix is $D = \alpha M + \beta K$ with α=7.55/s and β=5.6E-6s. This selection led to damping ratios between 0.65% and 1% for all transverse modes in the excitation band.

#### 4.4.1 Linear Dynamic Results

The computational effort required to compute the full dynamic response of the 96,156 degree-of-freedom 9-bay panel was found to be too high with NX/Nastran SOL 109 (full transient analysis). For instance, the amount of scratch space needed to compute the response of a relatively short time history of 50,000 time steps was approximately equal to 320GB. The specifics of why so much scratch space is needed are not known to the author; however, a newer solver in NX/Nastran, SOL 601, was found to be more computationally expedient and it can be used to solve linear and nonlinear problems. This new solver is an integration of the ADINA solver into NX/Nastran, and consequently the elements use a different formulation than the conventional NX and MSC Nastran solution sequences, like SOL 109, and some differences in the natural frequencies were found. Since it was not possible to obtain a time history of the response large enough with SOL 109, a modal transient analysis was performed with the first 89 modes which have natural frequencies within the frequency band of excitation. A comparison between SOL 601 (in its linear mode) and the modal analysis, for an acoustic excitation of 106dB, is shown in Figs. 4.25-4.28 at selected points. These points correspond to the middle points of bays 1,

2 and 5, and point A (see Fig. 4.29) in the frame substructure. The middle point of bay 5 is where the maximum global T3 displacement occurs; the middle point of bay 2 is near the peak of the T2 component; near the middle point of bay 1 the nonlinear effects on the T1 component can be observed; and point A in the frame is important because it is where the T1 and T3 components are dominant in the frame-longeron substructure.

The large modal density in the frequency range considered in this analysis can be clearly seen by the large number of peaks in the power spectral density plots. The family of modes between 334Hz to 434Hz has very small modal amplitudes in the transverse direction at the middle points of bays 2 and 5, which explains the sharp drop in energy in that frequency band. Finally, the sharp drop in the energy at 500Hz is because the acoustic excitation has no energy to induce resonance of the modes with natural frequencies higher than 500Hz.

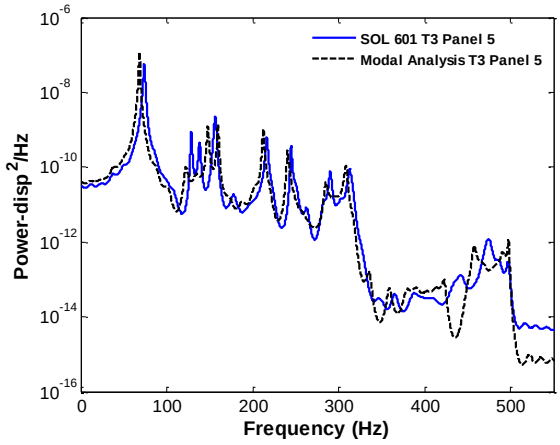


(a)

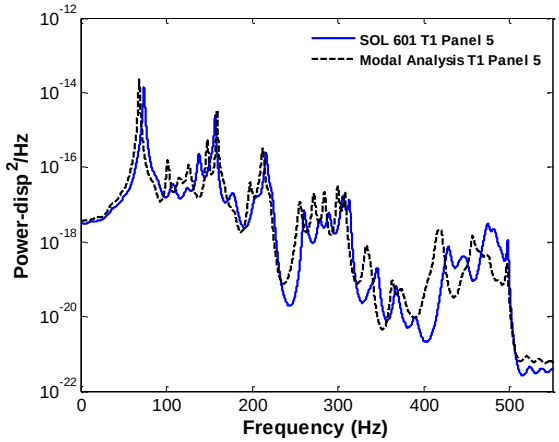


(b)

Figure 4.25. Power spectral density of the transverse (T3) and in-plane (T1) deflections at the middle point of bay 5. Full transient finite element analysis ("SOL 601") and transient modal analysis, *SPL* =106dB.

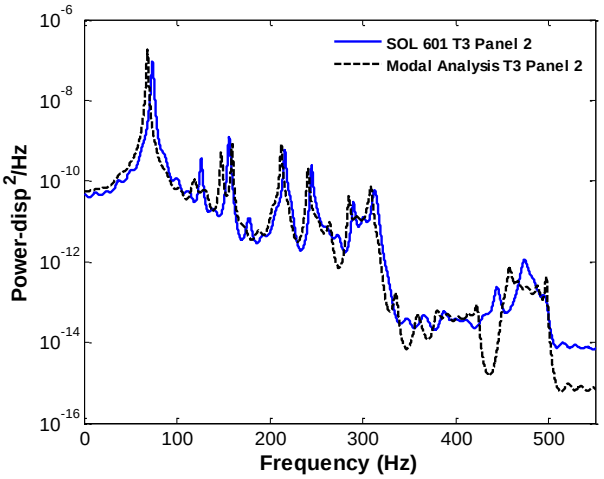


(a)

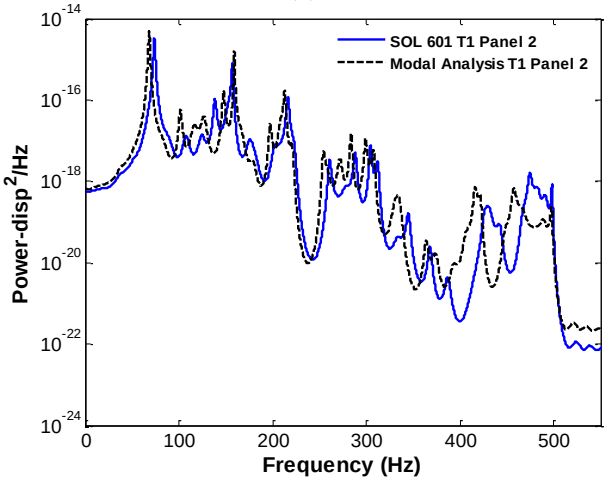


(b)

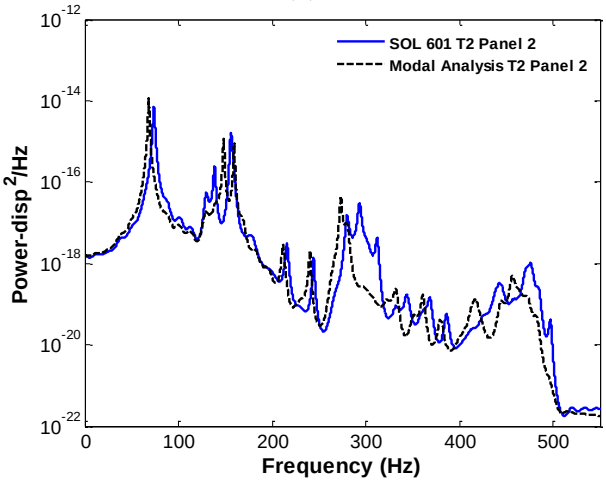


(c)

Figure 4.26. Power spectral density of the transverse (T3) and in-plane (T1 and T2) deflections at the middle point of bay 2. Full transient finite element analysis ("SOL 601") and transient modal analysis, *SPL* =106dB.

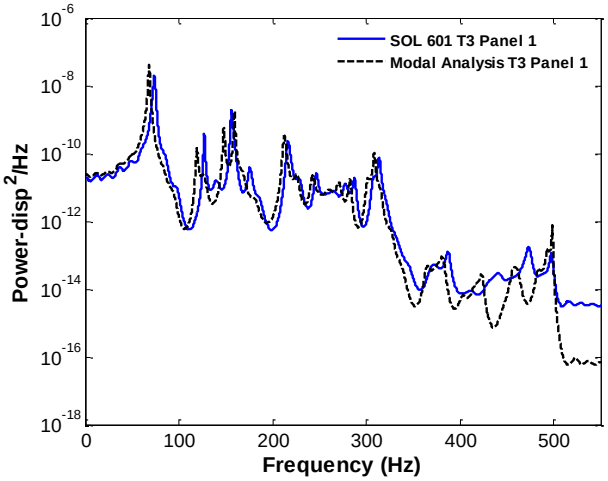


(a)

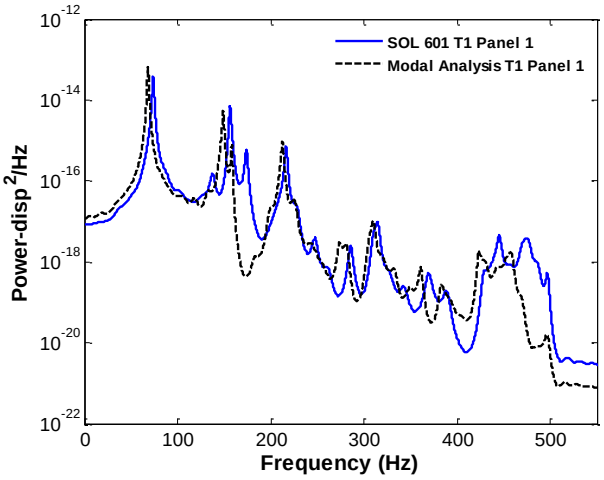


(b)

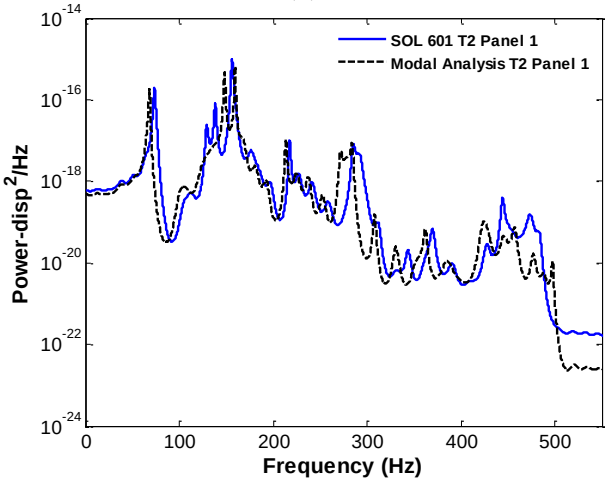


(c)

Figure 4.27. Power spectral density of the transverse (T3) and in-plane (T1 and T2) deflections at the middle point of bay 1. Full transient finite element analysis ("SOL 601") and transient modal analysis, *SPL* =106dB.

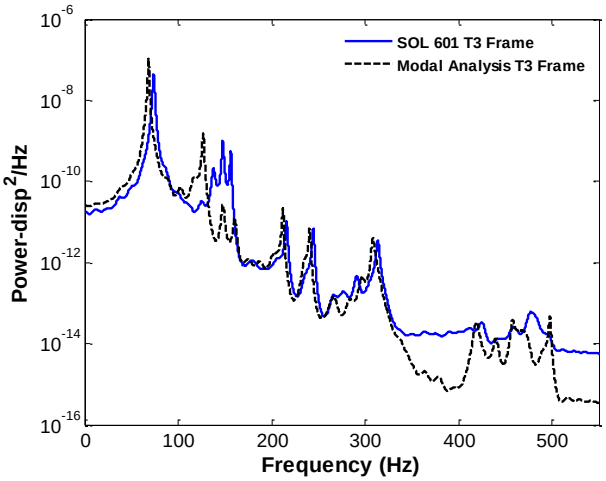


(a)

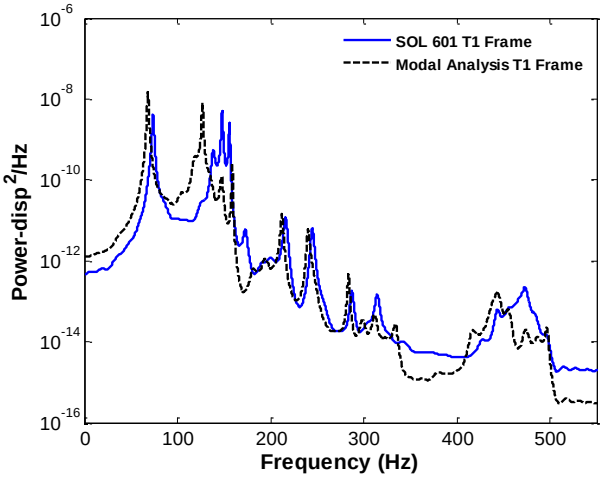


(b)

Figure 4.28. Power spectral density of the transverse (T3) and in-plane (T1 and T2) deflections at point A of the frame. Full transient finite element analysis ("SOL 601") and transient modal analysis, *SPL* =106dB.

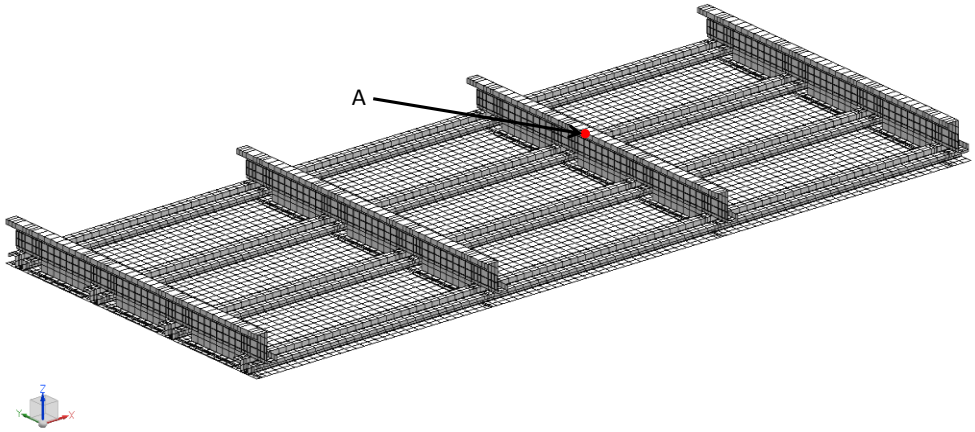


Figure 4.29. Location of selected frame node for output of results.

### 4.4.2. Nonlinear Dynamic Validation Results

Two excitation levels were used for the dynamic validation; the first one with a sound pressure level of 136dB, which led to a peak transverse displacement of approximately 1 skin panel thickness; and the second one with a sound pressure level of 146dB, which led to a peak transverse displacement of approximately 2.5 skin panel thicknesses. These two levels ranged from lowly to highly nonlinear.

The computational effort required to obtain the nonlinear dynamic response of the 96,156 degree-of-freedom 9-bay panel was found to be very large. Two different solvers were considered: MSC/Nastran SOL 400 and NX/Nastran SOL 601. The advantage of using SOL 400 is that it shares the same element formulation as SOL 106, which was used to identify the nonlinear stiffness coefficients of the reduced order model. Unfortunately, a very large amount of disk space was required to store the scratch data generated during the run (e.g., 700GB for 100,000 time steps), a successful SOL 400 simulation of a long time history was not possible given our current computational resources. Therefore, NX/Nastran SOL 601 was chosen. The wall time used for the solution of 250,000 time steps was approximately equal to 8 days using 6 processors.

A series of 200 “snapshots” were obtained from the stationary part of the NX/Nastran SOL601 dynamic simulation for the 136dB and 144dB excitation levels. The representation errors were computed and the mean representation error was used as a measure of the appropriateness of the basis. Shown in Table 4.3 are the mean representation errors, for both excitation levels, corresponding to the 82-mode basis identified in a previous section. Clearly, the errors are large, especially for the 144dB level. Therefore, the basis identification procedure described for the static validation was used with the “snapshots” of the dynamic problem. A reduced order basis was identified

from 48 linear modes and 21 dual modes. The mean representation errors for this basis are also shown in Table 4.4.

The first 9 dominant linear modes were 1, 13, 16, 25, 15, 7, 5, 28, and 46; where the modes were sorted from most to least dominant. The modal component of mode 1 was found to be larger than the other ones for most of the dynamic "snapshots" analyzed; therefore, it was considered as the only dominant mode in Eqs. (2.45) and (2.46). The 21 dual modes of the 69-mode basis were obtained from the 5 most dominant modes. The POD-based dual mode construction procedure highlighted above was performed for the data obtained for mode 1 alone and each of the *n* combinations of mode 1 and another of the *n* largest responding modes, where *n* is equal to 4. For each of these *n* situations, 12 different loading factors $\alpha_i^{(m)}$ were used, half positive and half negative, and leading to peak deflections ranging from 0.6 to approximately 1.3 skin panel thicknesses. The residuals of these 12×*n* deflections, after projection on the 48 linear modes identified above, were analyzed by POD. The POD eigenvectors with largest eigenvalues and leading to a reduction of the representation error of the T2 component (i.e., the dominant in-plane component) were selected as dual modes. Shown in Table 4.4 are the mean representation errors for the 69-mode model. Clearly, the representation of the response corresponding to both excitation levels is better than for the 82-mode model.

Table 4.4. Summary of Mean Representation Errors - Skin Panel

| | 69-Mode (136dB) | 82-Mode (136dB) | 69-Mode (144dB) | 82-Mode (144dB) |
|---|---|---|---|---|
| T3 | 0.2% | 0.2% | 0.5% | 0.7% |
| In-Plane Mag. | 3.3% | 16.8% | 14.6% | 37.3% |
| T2 | 3.7% | 23.4% | 19.7% | 55.7% |
| T1 | 6.6% | 26.2% | 22.6% | 61.1% |

Next, it was desired to assess the predictive capabilities of the reduced order models in comparison with the dynamic solution of SOL601 in NX/Nastran. Shown in Figs. 4.30 and 4.31 are plots of the power spectral density of the transverse (T3) and in-plane (T1 and T2) responses of the middle point of bays 1 and 2 (see Fig. 4.2(b) for panel numbering). The T2 component is very small at the middle point of bay 5 and point A (see Fig. 4.29) of the frame; therefore, only the power spectral density of the T3 and T1 components are shown in Figs. 4.32 and 4.33. Clearly, the matching of the T3 component is very good. Furthermore, the dominant aspects of the in-plane response (i.e., the first peaks for which the energy of the response is larger) are also captured well. Most of the peaks of the power spectral plots are sharp, which indicates that the level of nonlinearity is not too large for this excitation level.

The power spectral densities of the transverse (T3) and in-plane (T1 and T2) responses of the middle points of bays 1 and 2 are shown in Figs. 4.34 and 4.35. The results for the T3 and T1 components of the middle point of bay 5 and point A of the frame are shown in Figs. 4.36 and 4.37. The matching of the first peak of the T3 component (dominant component) is excellent for all cases. Furthermore, the energy level of the rest of the peaks was well captured by the 69-mode model, except for the frame, where it can be seen that the ROM response is stiffer than the SOL 601 results. The matching of the T2 component at bays 1 and 2 is excellent for all frequencies. The correlation of the first peak of the T1 component is very good for all cases.

The wall time used for the solution of 250,000 time steps was approximately equal to 10 days using only 1 processor (please see Chapter 6 for a discussion on algorithmic improvements that permit the reduction of the computational time).

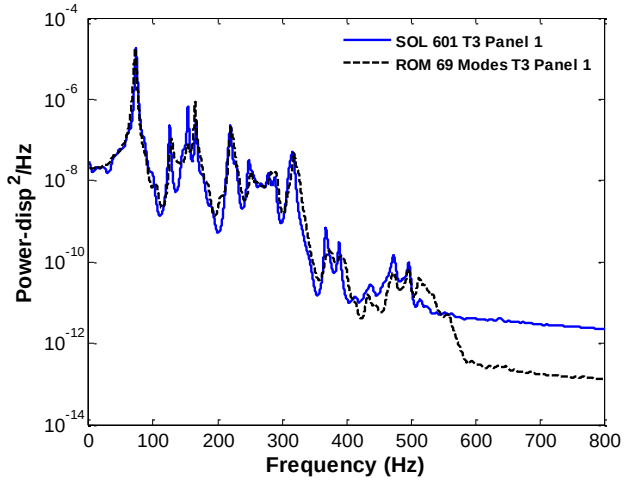


a)

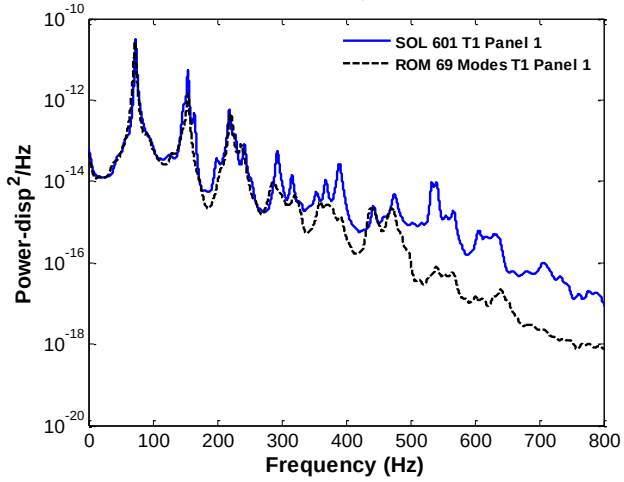


b)

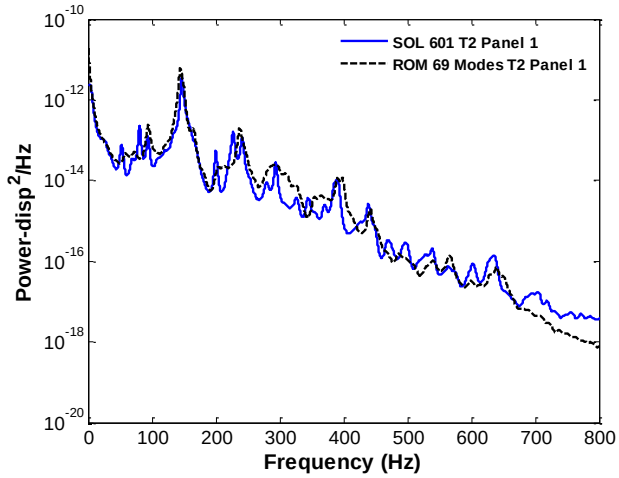


c)

Figure 4.30. Power spectral density of the transverse (T3) and in-plane (T1 and T2) deflections at the middle point of bay 1. Reduced order model and finite element ("SOL 601"), *SPL* =136dB.

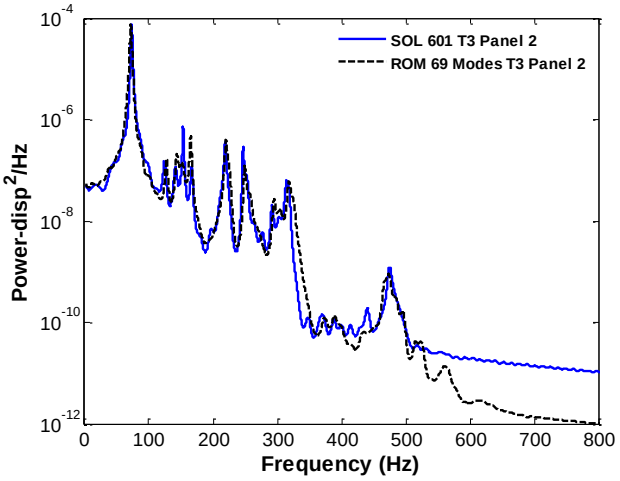


a)

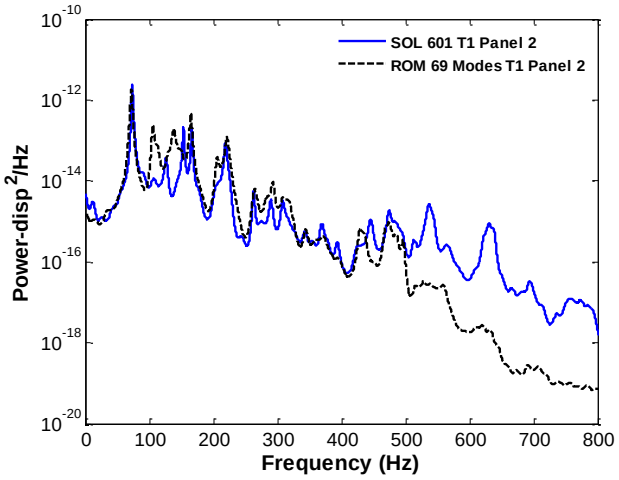


b)

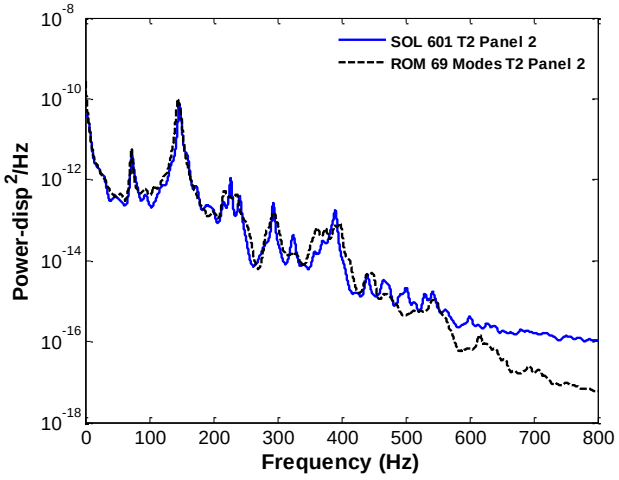


c)

Figure 4.31. Power spectral density of the transverse (T3) and in-plane (T1 and T2) deflections at the middle point of bay 2. Reduced order model and finite element ("SOL 601"), *SPL* =136dB.

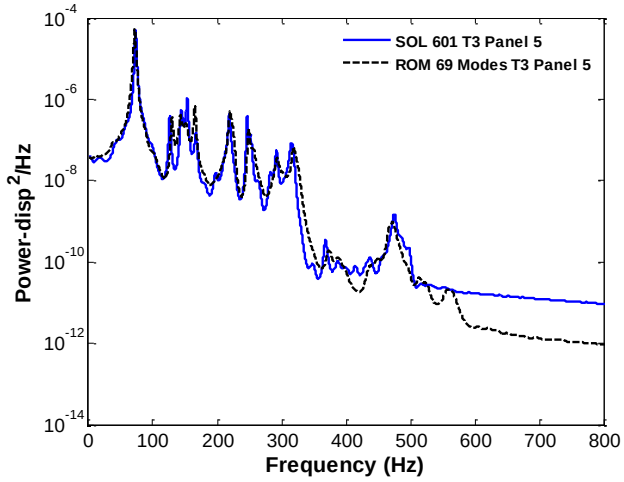


a)

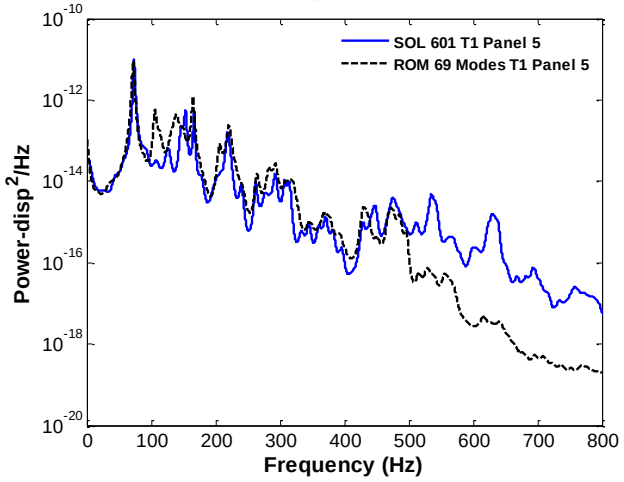


b)

Figure 4.32. Power spectral density of the transverse (T3) and in-plane (T1) deflections at the middle point of bay 5. Reduced order model and finite element ("SOL 601"), *SPL* =136dB.

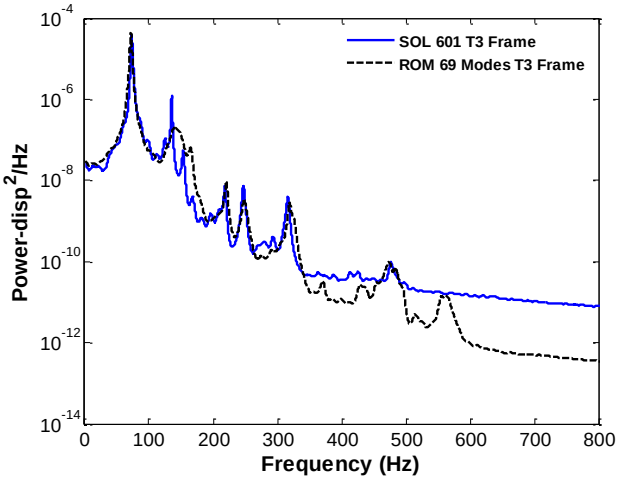


a)

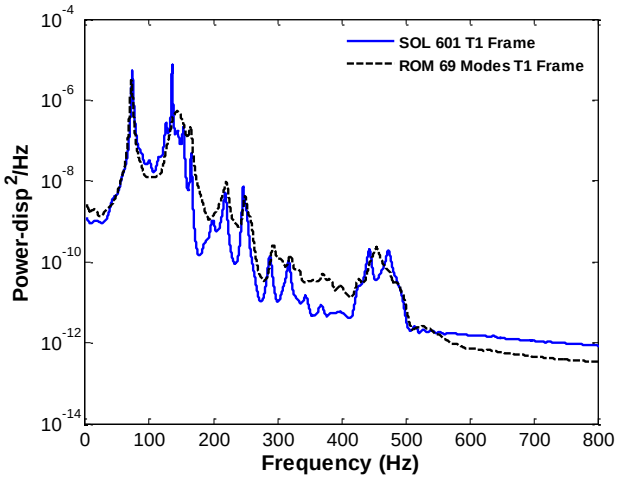


b)

Figure 4.33. Power spectral density of the transverse (T3) and in-plane (T1) deflections at point A of the frame. Reduced order model and finite element ("SOL 601"), *SPL* =136dB.

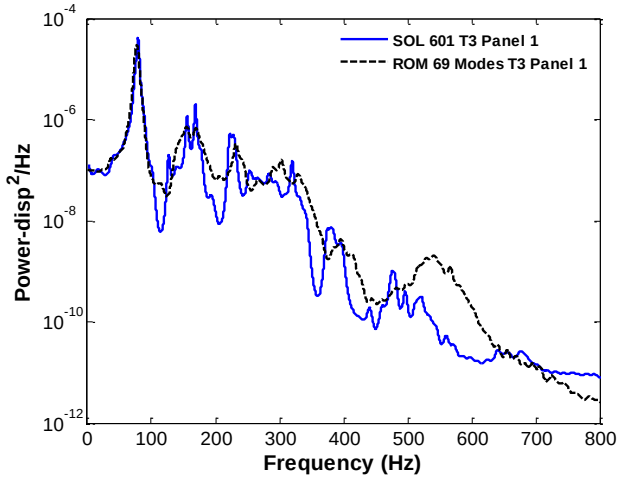


a)

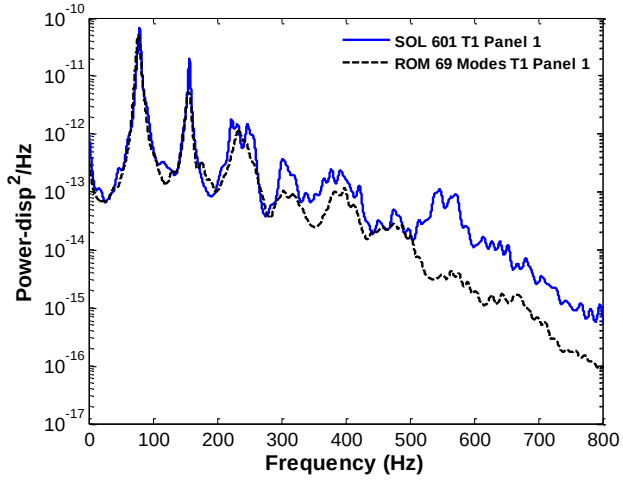


b)

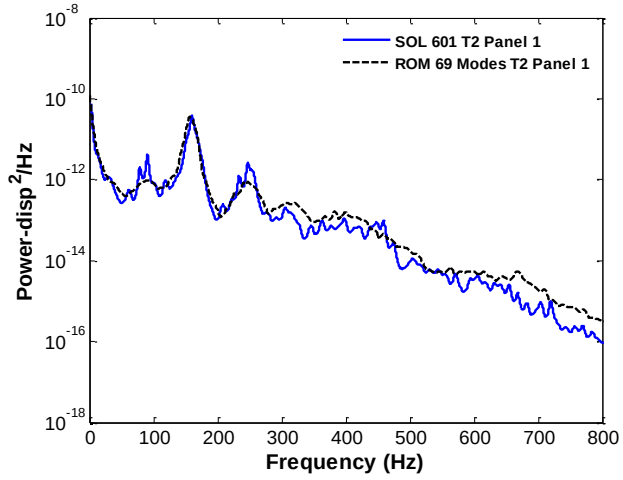


c)

Figure 4.34. Power spectral density of the transverse (T3) and in-plane (T1 and T2) deflections at the middle point of bay 1. Reduced order model and finite element ("SOL 601"), *SPL* =144dB.

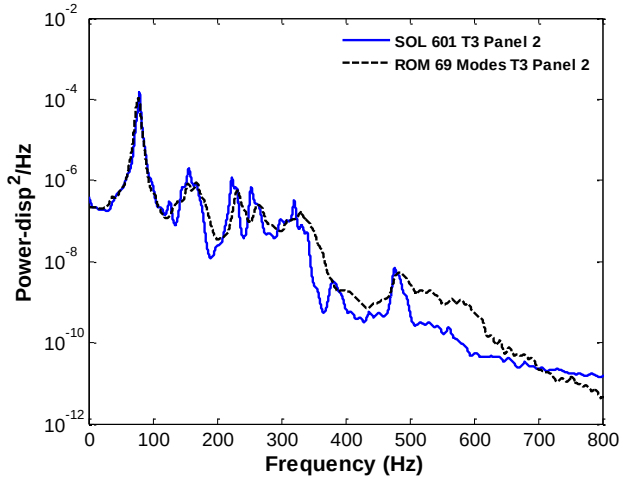


a)

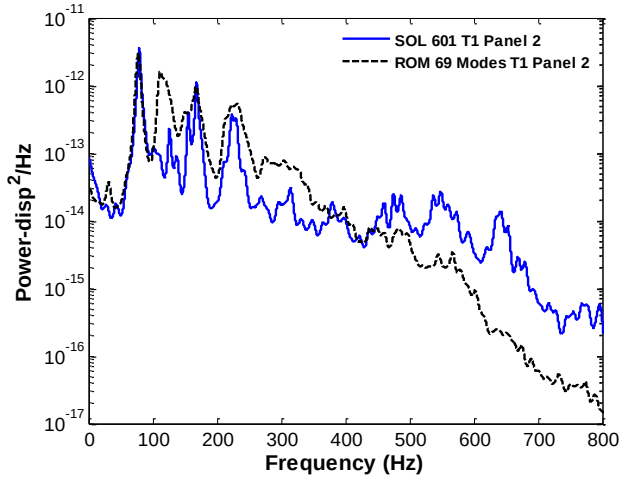


b)

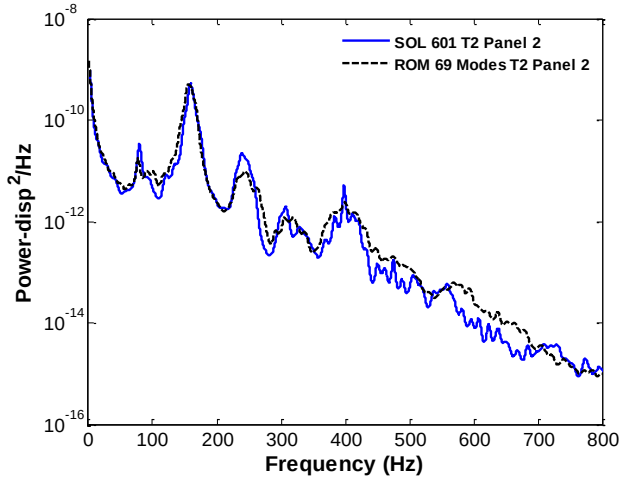


c)

Figure 4.35. Power spectral density of the transverse (T3) and in-plane (T1 and T2) deflections at the middle point of bay 2. Reduced order model and finite element ("SOL 601"), *SPL* =144dB.

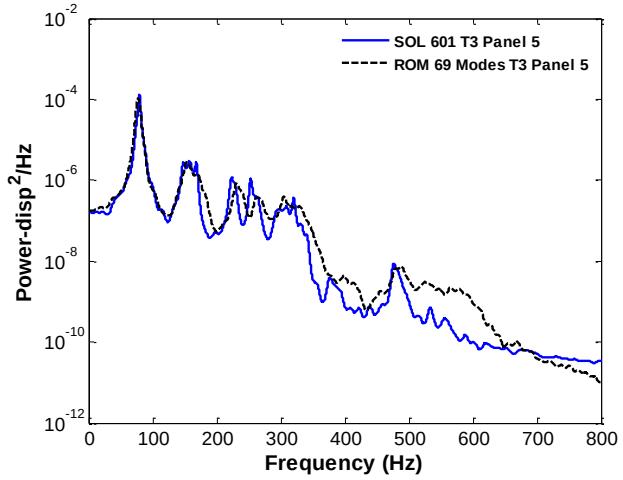


a)

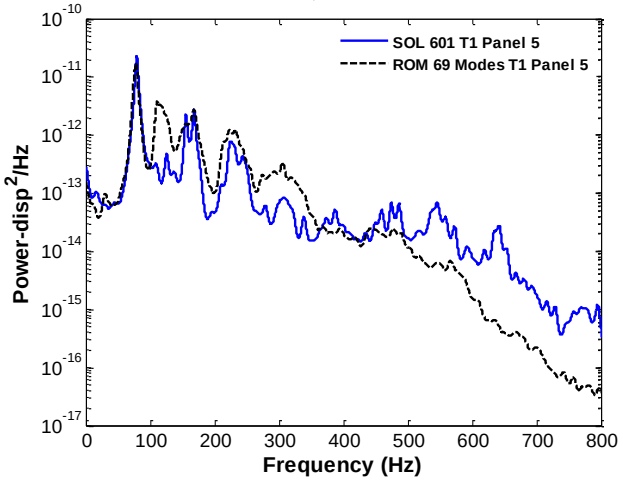


b)

Figure 4.36. Power spectral density of the transverse (T3) and in-plane (T1) deflections at the middle point of bay 5. Reduced order model and finite element ("SOL 601"), *SPL* =144dB.

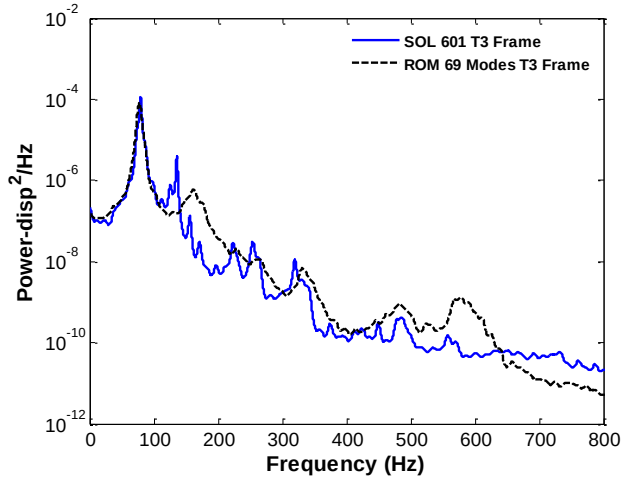


a)

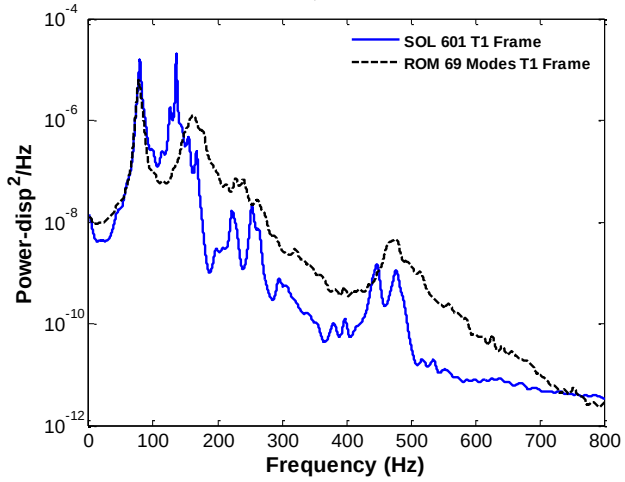


b)

Figure 4.37. Power spectral density of the transverse (T3) and in-plane (T1) deflections at the frame. Reduced order model and finite element ("SOL 601"), *SPL* =144dB.

A first assessment of the 69-mode ROM prediction with its MSC/Nastran SOL 400 counterpart was done for the 144dB excitation level. Four shorter time histories (100,000 time steps vs. 250,000) were analyzed, the power spectral densities computed, and their mean compared with the SOL 601 and the 69-mode ROM results. The amount of scratch space generated during the analysis of 100,000 time steps was within our computational resources. Shown in Figs. 4.37-4.38 are power spectral density plots of the transverse and in-plane displacements at some of the most important locations. As noted in the linear case, there are differences between the SOL 601 and SOL 400 predictions,

although they are less significant in the nonlinear case. The 69-mode model still does a good qualitative job, although a better matching of the third and fourth peaks of the T3 components would be desired.

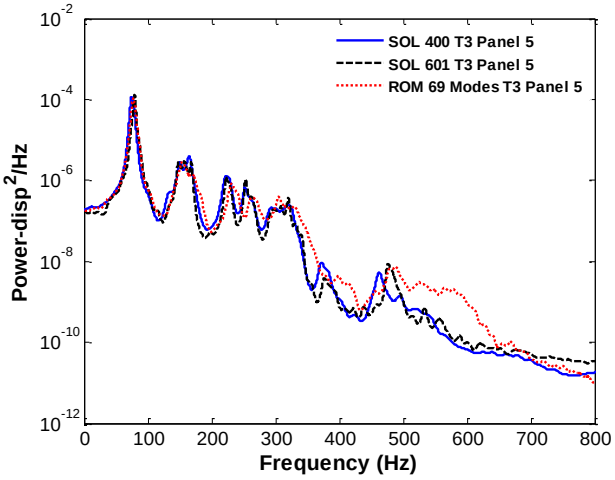


a)

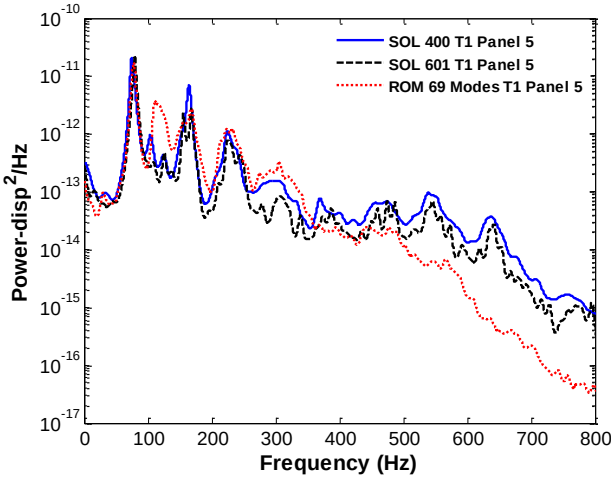


b)

Figure 4.38. Power spectral density of the transverse (T3) and in-plane (T1) deflections at the middle point of bay 5. Reduced order model and finite element ("SOL 400" and "SOL 601"), *SPL* =144dB.

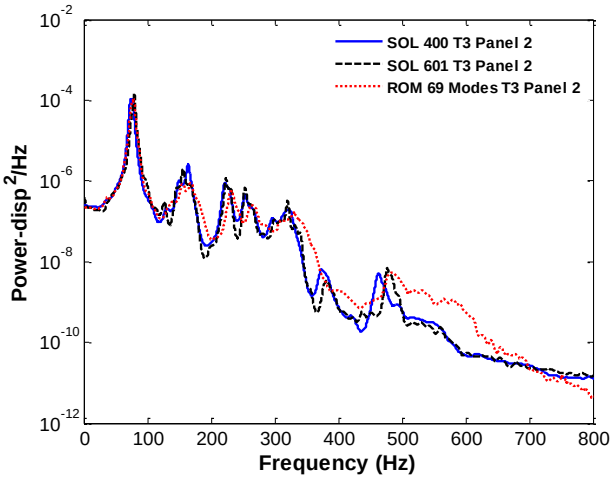


a)

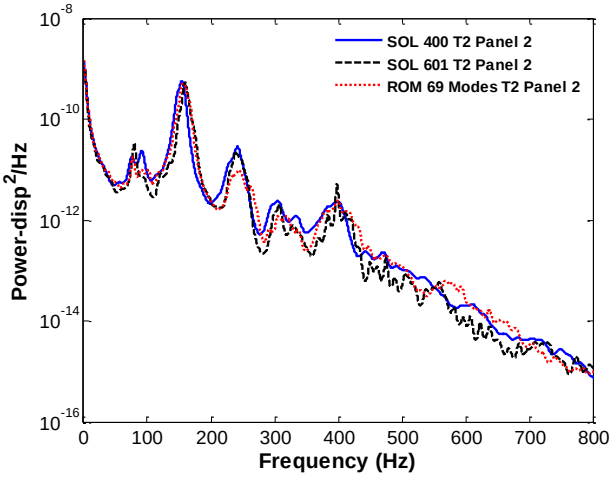


b)

Figure 4.39. Power spectral density of the transverse (T3) and in-plane (T2) deflections at the middle point of bay 2. Reduced order model and finite element ("SOL 400" and "SOL 601"), *SPL* =144dB.

The dynamic excitation in the previous validation cases consisted of a white noise band-limited process used to simulate an acoustic excitation. Next, it was desired to assess the ROM methodology by assuming the 9-bay panel to be excited by a uniform deterministic pressure acting on the skin panel. The energy was assumed to be flat in the range [-500,500] Hz, see Fig. 4.40 for time history and Fig. 4.41 for its frequency content. A more detailed description of this type of excitation can be found in [34]. Shown in Fig. 4.42 is the time history of the transverse displacement of the middle point of the middle panel. In addition, shown in Fig. 4.43 is the Fourier transform of the SOL

400 and SOL 601 responses. The first peak of the SOL 601 response has a lower magnitude and it's located at a higher frequency than the first peak of the SOL 400 response. This indicates that the response from SOL 601 is stiffer. This, in fact, can be observed with the other peaks as well.

A comparison between SOL 400 and the 69-mode ROM is shown in Figs. 4.44-4.46. Clearly, the most dominant features of the response are well captured by the 69-mode model. The matching of the T2 component is very good for all frequencies; the correlation of the T1 and T3 components is good for frequencies within the frequency band of excitation.

The results presented for the static and dynamic validations show that the ROM methodology can be used for the approximation of the response of complex structures.

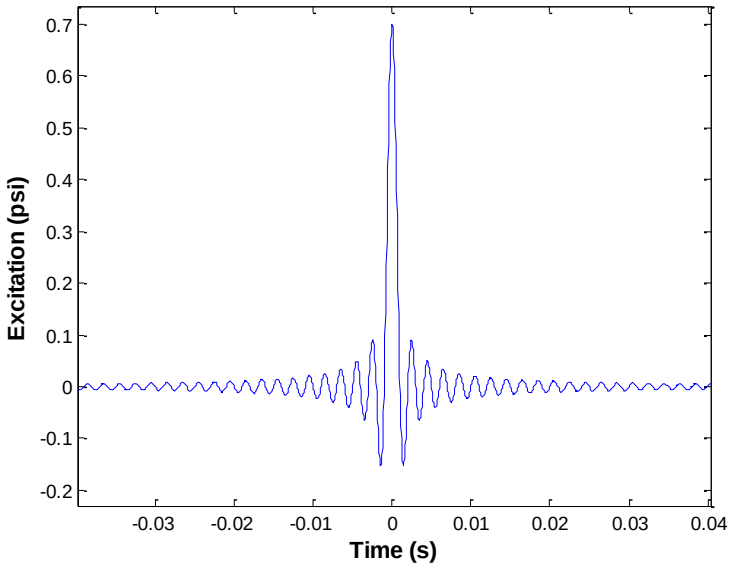


Figure 4.40. Time history of the loading.

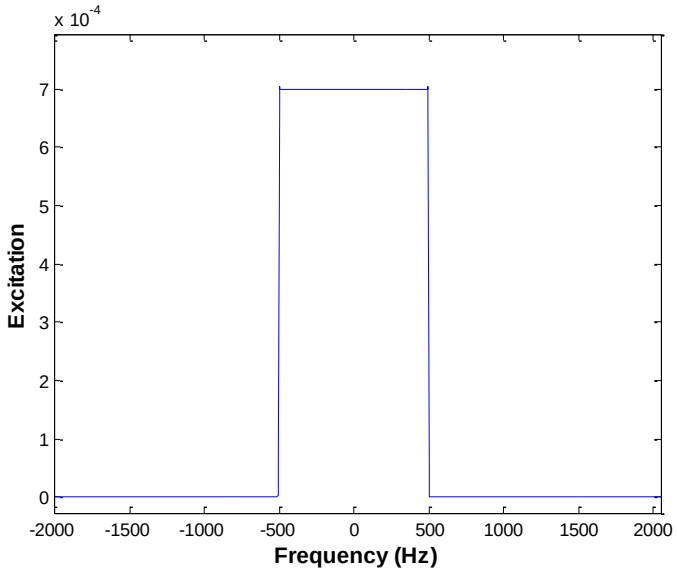


Figure 4.41. Frequency content of the loading.

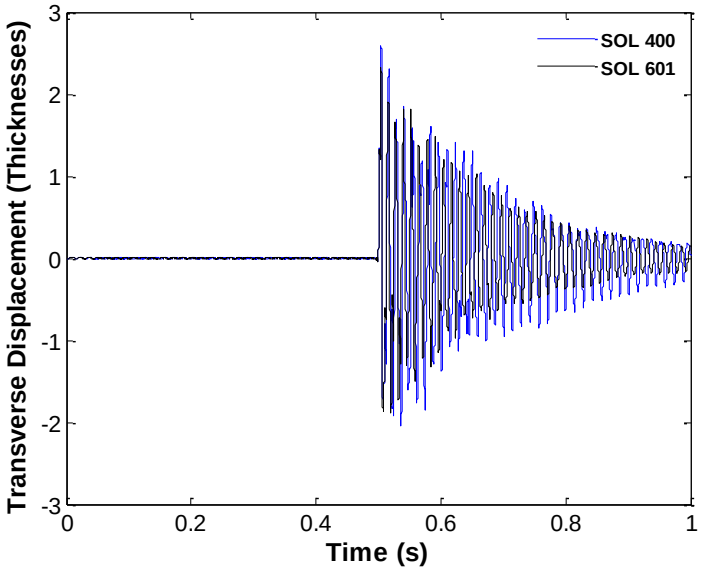


Figure 4.42. Transverse displacement of the middle point of the middle panel (full FEA results) as a function of time.

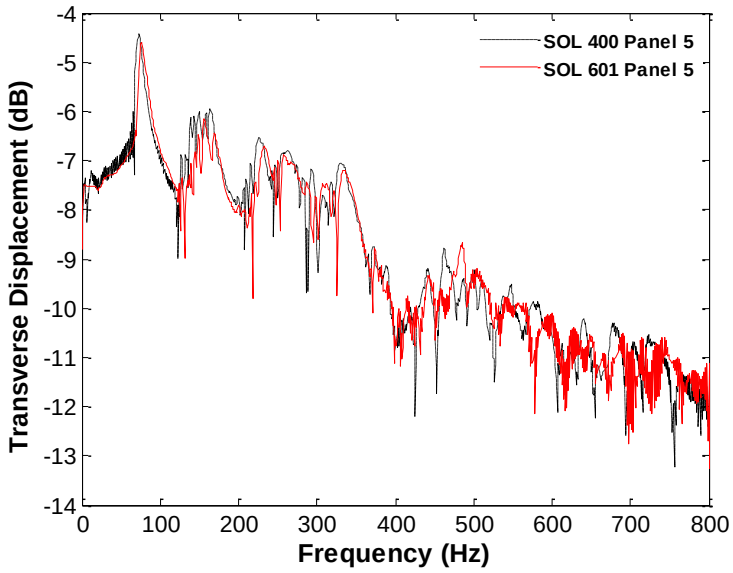


Figure 4.43. Transverse displacement of the middle point of bay 5 as a function of frequency, MSC/Nastran SOL 400 and NX/Nastran SOL601.

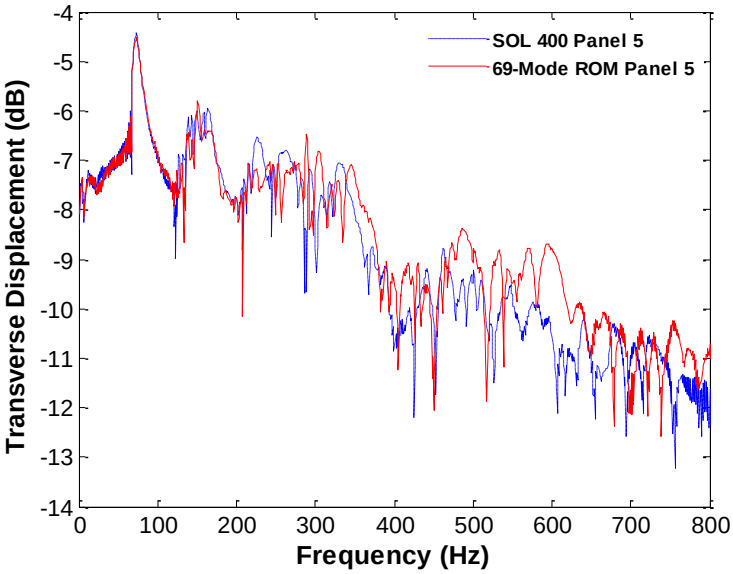


Figure 4.44. Transverse displacement of the middle point of bay 5 as a function of frequency, MSC/Nastran SOL 400 and ROM 69-mode model.

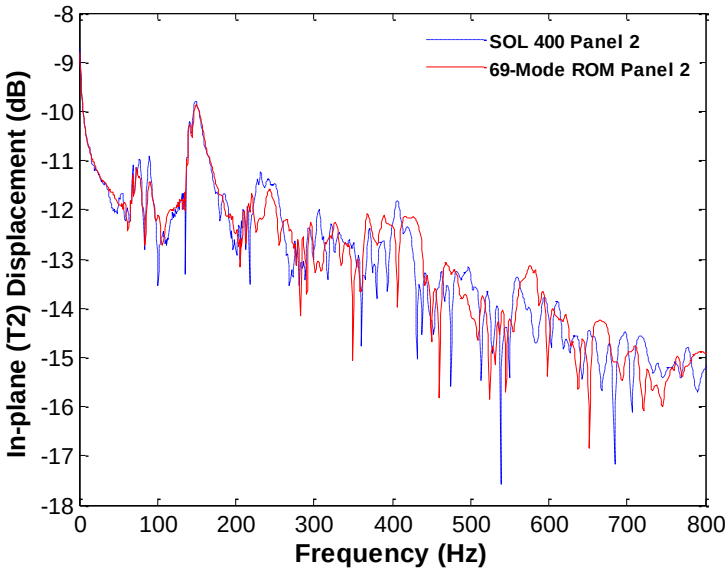


Figure 4.45. In-plane (T2) displacement of the middle point of bay 2 as a function of frequency, MSC/Nastran SOL 400 and ROM 69-mode model.

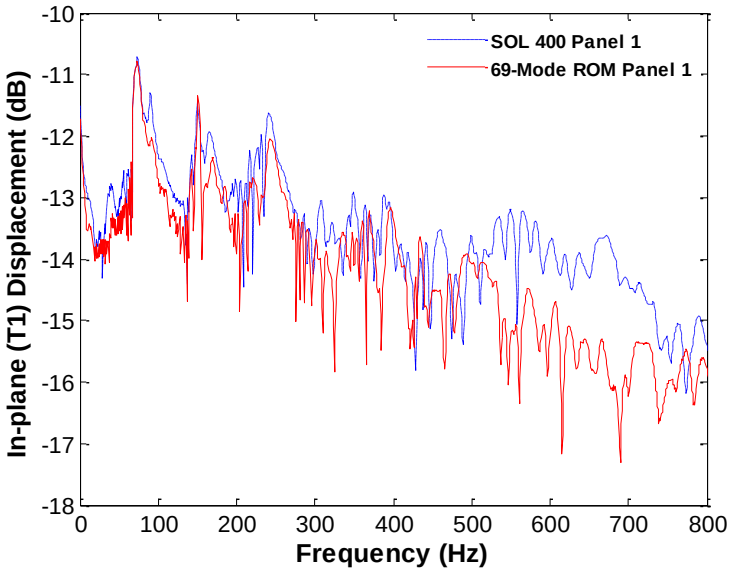


Figure 4.46. In-plane (T1) displacement of the middle point of bay 1 as a function of frequency, MSC/Nastran SOL 400 and ROM 69-mode model.

### 4.5. Multi-Scale Approach

The validation effort from previous sections showed that a monolithic ROM, i.e. one constructed from the entire structure, is capable of predicting the dominant features of the response of a complex multi-bay panel with a much smaller number of degrees-of-

freedom. Nonetheless, the 9-bay panel used in this validation effort is made of different substructures, which makes a multi-scale approach an attractive alternative to the monolithic ROM. In this case, the full model corresponds to the "macro-scale" and the response of a single bay lies in the "meso-scale".

In this light, a reduced order model could be built for each substructure at a time in a *Bottom-Up* approach, and then these reduced order models assembled in order to predict the response of the entire structure (see left half of Fig. 4.47). Or, the global response of the entire model could be approximated and the interface information of a particular substructure used to compute the response of that substructure in a *Top-Down* approach (see right half of Fig. 4.47).

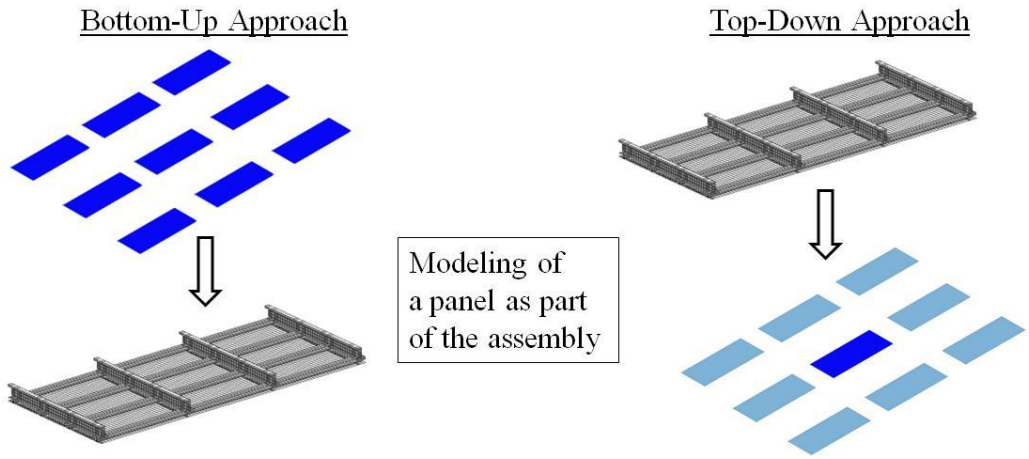


Figure 4.47. In-plane (T1) displacement of the middle point of bay 1 as a function of frequency, MSC/Nastran SOL 400 and ROM 69-mode model.

The modeling of a panel as part of the assembly is a key aspect in both approaches, and the successful development of reduced order models for single beams and panels during the last decade or so makes the proposed multi-scale approach very appealing. Another advantage of this approach is in a possible reduction of the computational cost, which could be achieved by building the reduced order model of one substructure at a time. Furthermore, a multi-scale approach may help in gaining a better

understanding of the complexities of the response induced by the interaction between substructures.

In the present work, a first assessment of a *Bottom-Up* approach, based on the Criag-Bampton Method, will be presented.

### 4.3.1. Background on CMS

The objective of Component Mode Synthesis methods in the analysis of dynamic structures is to reduce the complexity associated with large finite element models that arise from complex structures. In essence, these methods involve the division of the structure into substructures, the development of reduced order models of the substructures, and the coupling of the component reduced order models to form one for the entire system [32]. In general, the accuracy of the reduced order model is improved by using an increasing quantity of modes in each substructure.

The equation of motion of an undamped substructure *s* may be written as follows,

$$\underline{\underline{M}}^{(s)}\ddot{\underline{u}}^{(s)} + \underline{\underline{K}}^{(s)}\underline{u}^{(s)} = \underline{F}^{(s)}. \tag{4.2}$$

where $\underline{\underline{M}}^{(s)}$, $\underline{\underline{K}}^{(s)}$, $\underline{u}^{(s)}$, and $\underline{F}^{(s)}$ are the mass matrix, stiffness matrix, displacement vector, and the force vector of the substructure, all expressed in physical coordinates. The mass and stiffness of substructure *s* can be expressed as follows,

$$\begin{bmatrix} \underline{\underline{M}}_{ii} & \underline{\underline{M}}_{iB} \\ \underline{\underline{M}}_{Bi} & \underline{\underline{M}}_{BB} \end{bmatrix}^{s} \tag{4.3}$$

$$\begin{bmatrix} \underline{\underline{K}}_{ii} & \underline{\underline{K}}_{iB} \\ \underline{\underline{K}}_{Bi} & \underline{\underline{K}}_{BB} \end{bmatrix}^{s} \tag{4.4}$$

where *i* corresponds to the interior degrees-of-freedom and *B* corresponds to the boundary degrees-of-freedom.

A reduced order model of the substructure, using the Craig-Bampton method, can be obtained by expressing the internal and boundary degrees-of-freedom as

$$\begin{aligned} \underline{u}^{(s)} &= \underline{\underline{\Phi}}^{(s)} \underline{q}^{(s)} + \underline{\underline{\Xi}}^{(s)} \underline{Y}^{(s)} \\ \underline{u}_B^{(s)} &= \underline{Y}^{(s)} \end{aligned} \tag{4.5}$$

where $\underline{\underline{\Phi}}^{(s)}$ denotes a matrix of $p$ selected fixed-interface modes, where one of its columns $\varphi_j$ is obtained from

$$\underline{\underline{K}}_{ii}^{(s)} \underline{\varphi}_j^{(s)} = \lambda_j^{(s)} \underline{\underline{M}}_{ii}^{(s)} \underline{\varphi}_j^{(s)} . \tag{4.6}$$

Furthermore, $\Xi$ is the matrix of constraint modes obtained as follows

$$\underline{\underline{\Xi}}^{(s)} = -\left(\underline{\underline{K}}_{ii}^{(s)}\right)^{-1} \underline{\underline{K}}_{iB}^{(s)} . \tag{4.7}$$

Finally, the vector $\underline{q}^{(s)}$ contains the generalized coordinates of the fixed-interface modes.

The transformation matrix where the fixed-interface modes and constraint modes are included is

$$\underline{\underline{T}}_1^{(s)} = \begin{bmatrix} \underline{\underline{\Phi}}^{(s)} & \underline{\underline{\Xi}} \\ 0 & \underline{\underline{I}} \end{bmatrix} \tag{4.8}$$

where $\underline{\underline{I}}$ denotes the identity matrix of appropriate dimensions.

The reduced Craig-Bampton mass and stiffness matrices can be obtained as follows

$$\underline{\underline{\overline{M}}}^{(s)} = \left(\underline{\underline{T}}_1^{(s)}\right)^T \underline{\underline{M}}^{(s)} \underline{\underline{T}}_1^{(s)} = \begin{bmatrix} \underline{\underline{\overline{M}}}_{qq} & \underline{\underline{\overline{M}}}_{qY} \\ \underline{\underline{\overline{M}}}_{Yq} & \underline{\underline{\overline{M}}}_{YY} \end{bmatrix}^s \tag{4.9}$$

and

$$\overline{\underline{\underline{K}}}^{(s)} = \left(\underline{\underline{T}}_1^{(s)}\right)^T \underline{\underline{K}}^{(s)} \underline{\underline{T}}_1^{(s)} = \begin{bmatrix} \overline{\underline{\underline{K}}}_{qq} & \overline{\underline{\underline{K}}}_{qY} \\ \overline{\underline{\underline{K}}}_{Yq} & \overline{\underline{\underline{K}}}_{YY} \end{bmatrix}^s . \tag{4.10}$$

Two observations from the stiffness matrix are in order. First, the top left partition is diagonal and it contains the eigenvalues of the fixed-interface problem. Second, the fixed-interface modal coordinates and the modal coordinates from the constraint modes are uncoupled. This means that the only coupling between these sets of coordinates appears in the dynamic case since the mass matrix is full.

The reduced order model that results from the Craig-Bampton method has two types of degrees-of-freedom: modal coordinates for the interior degrees-of-freedom and physical coordinates for the boundary degrees-of-freedom. A "full" reduced order model can be developed by expressing the physical boundary degrees-of-freedom of the entire system [33] as

$$\underline{Y} = \underline{\underline{\Psi}}\,\underline{z} \tag{4.11}$$

where $\underline{\underline{\Psi}} = \begin{bmatrix} \underline{\psi}_1 & \underline{\psi}_2 & \cdots & \underline{\psi}_r \end{bmatrix}$ is a matrix whose columns are the eigenvectors corresponding to

$$\underline{\underline{K}}_{BB}\underline{\psi}_j = \lambda_j \underline{\underline{M}}_{BB}\underline{\psi}_j . \tag{4.12}$$

This second reduction of degrees-of-freedom is achieved by the following transformation matrix

$$\underline{\underline{T}}_2 = \begin{bmatrix} \underline{\underline{I}} & 0 \\ 0 & \underline{\underline{\Psi}} \end{bmatrix}. \tag{4.13}$$

Using this transformation, the mass and stiffness matrices are reduced as follows

$$\hat{\underline{\underline{M}}}^{(s)} = \left(\underline{\underline{T}}_2^{(s)}\right)^T \overline{\underline{\underline{M}}}^{(s)} \underline{\underline{T}}_2^{(s)} = \begin{bmatrix} \hat{\underline{\underline{M}}}_{qq} & \hat{\underline{\underline{M}}}_{qu} \\ \hat{\underline{\underline{M}}}_{uq} & \hat{\underline{\underline{M}}}_{uu} \end{bmatrix}^s \tag{4.14}$$

and

$$\hat{\underline{\underline{K}}}^{(s)} = \left(\underline{\underline{T}}_2^{(s)}\right)^T \overline{\underline{\underline{K}}}^{(s)} \underline{\underline{T}}_2^{(s)} = \begin{bmatrix} \hat{\underline{\underline{K}}}_{qq} & \hat{\underline{\underline{K}}}_{qu} \\ \hat{\underline{\underline{K}}}_{uq} & \hat{\underline{\underline{K}}}_{uu} \end{bmatrix}^s . \tag{4.15}$$

### 4.3.2. Modeling Assumptions

The 9-bay panel was divided into 11 substructures as shown in Fig. 4.48; the skin panel was divided into 9 bays of equal size (substructures 1 to 9); the part of the skin panel surrounding the bays (substructure 10); and the frames and longerons (substructure 11). For most of the bay boundaries the skin panel is riveted to the frame-longeron substructure. However, as shown in Fig. 4.49 there are some nodes on the skin panel, between the frames and the longerons, which are not attached to the frame-longeron substructure; these are the nodes next to the red dots shown in Fig. 4.49. This has a local effect in the linear response, but also in the in-plane displacement induced by the nonlinear response.

It was seen that the fixed-interface modes of substructure 10 did not have a visible contribution in the synthesis of the global modes; therefore, only the constraint modes for this substructure were kept.

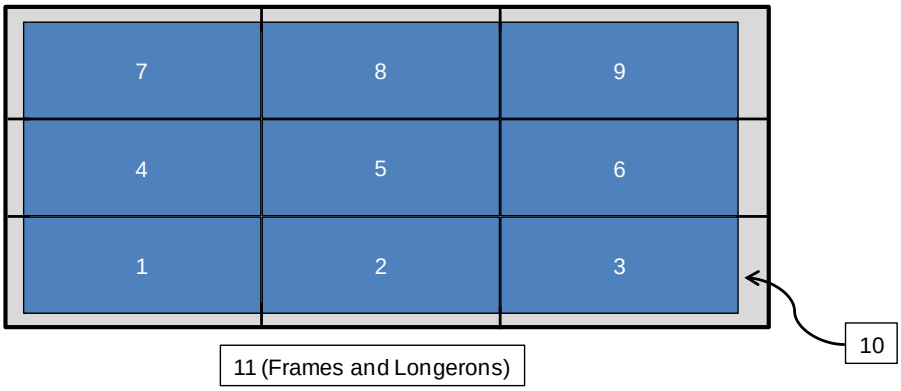


Figure 4.48. 9-bay panel divided into 11 substructures.

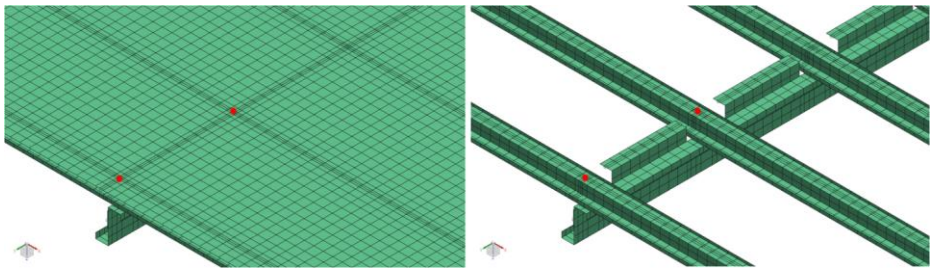

Figure 4.49. Zoomed-in view of skin-frame connection.

It is of interest to use the Craig-Bampton Method to create a basis for the 9-bay panel following a *Bottom-Up* approach. Based on the previous discussion, there are two families of modes that need to be obtained: i) fixed-interface modes and ii) constraint modes. Shown in Fig. 4.50 is a contour plot of the transverse component of the first fixed-interface mode of one of the bays of the 9-bay panel. Shown in Fig. 4.51 is a constraint mode, obtained from the linear static response due to a unit displacement in the transverse direction of an interface node of one of the bays. The constraint modes computed by imposing a unit in-plane displacement along the T1 or T2 direction also resulted in a localized transverse response. However, the transverse response due to a unit rotation with respect to a vector along the T1 or T2 direction (R1 and R2, respectively) was not localized.

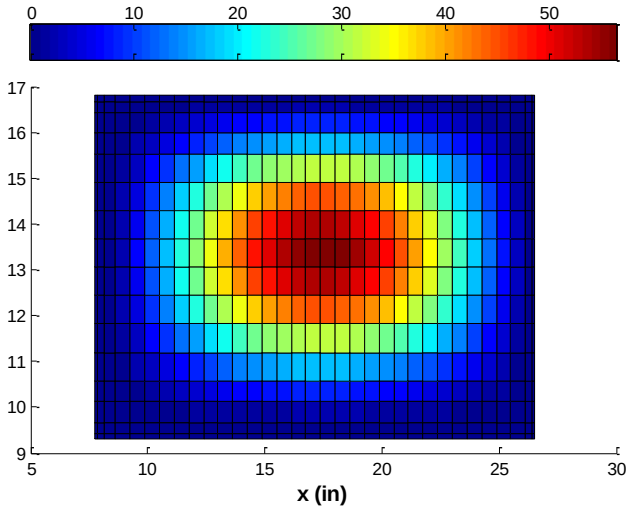


Figure 4.50. Transverse component of a bay first fixed-interface mode.

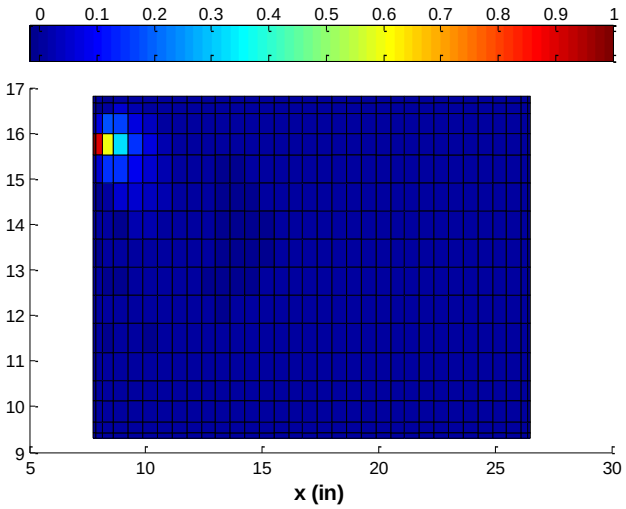


Figure 4.51. Transverse component of the linear static response due to a unit displacement in the transverse direction of an interface node of one of the bays.

The number of boundary and interior nodes, for each substructure, is shown in Table 4.5. Since the interface degrees-of-freedom are expressed in terms of physical coordinates, the number of constraint modes matches the number of interface degrees-of-freedom. The 9-bay panel has a total of 3,771 free interface degrees-of-freedom, so a total of 3,771 constraint modes were be created.

Table 4.5. Node and degree-of-freedom (Dof) number for each substructure.

| Substructure ID | Boundary Node # | Interior Node # | Total Dof |
|---|---|---|---|
| 1 – 9 | 98 × 9 | 480 × 9 | 3,468 × 9 |
| 10 | 350 | 1,094 | 8,664 |
| 11 | 532 | 9,976 | 63,048 |

### 4.3.3. Linear Problem

While the "exact" response predicted by the full FEA model of the 9-bay panel would be recovered if all the fixed-interface modes and constraint modes were included, a compact reduced order model was sought. To this end, a reduced order model of the entire model was assembled using different combinations of fixed-interface modes for each substructure while keeping the entire set of constraint modes. The final model selected led to a good matching of the modes and natural frequencies of the entire system

and the synthesized ones, which in turn ensures a good matching of the linear dynamic response. The difference between the synthesized and original modes was assessed in terms of the norm of the difference of these modes divided by the norm of the original mode.

Only the 46 modes of the entire system within the [0,500]Hz frequency band that had a significant contribution to the linear dynamic response were included. Shown in Fig. 4.52 are the relative errors of the transverse component (i.e., dominant component) of the skin panel nodes for different numbers of bay and frame fixed-interface modes. Shown in Fig. 4.53 are the relative errors of the natural frequencies. Clearly, even the smallest model yielded a good prediction of the natural frequencies. However, this was not the case with the mode shapes, where a more clear effect can be seen from using different numbers of bay and frame fixed-interface modes. For example, the "10 Bay, 100 Frame" model led to good agreement for a majority of the original modes. Increasing the number of bay or frame fixed-interface modes led to improvements in the other cases, but at a higher cost in the number of modes.

With this in mind, it was desired to further assess the "10 Bay, 100 Frame" model by comparing its linear dynamic response with the one corresponding to the original modes of the full structure. To this end, the 9-bay panel was subjected to a uniform pressure on its top surface varying randomly in time as a white noise band-limited process in the frequency range [0,500Hz] used to simulate an acoustic loading. The acoustic excitation consisted of an overall sound pressure level (*OASPL*) of 106dB. As in the dynamic validation of the monolithic ROM (see the previous section), a simple Rayleigh damping model was adopted with $\alpha$=7.55/s and $\beta$=5.6E-6s. This selection led to damping ratios between 0.65% and 1% for all transverse modes in the excitation band. The power spectral density of the transverse displacement of the middle point of the

middle panel, for the original modes and the synthesized modes, is shown in Fig. 4.54. The matching of the dominant features of the dynamic response is excellent, which indicates the suitability of the "10 Bay, 100 Frame" model.

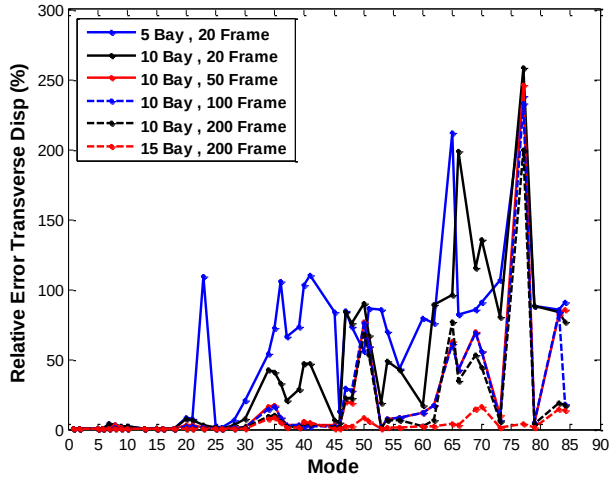


Figure 4.52. Relative errors of the transverse (normal) component of the skin degrees-of-freedom for different combinations of bay-frame fixed-interface mode numbers.

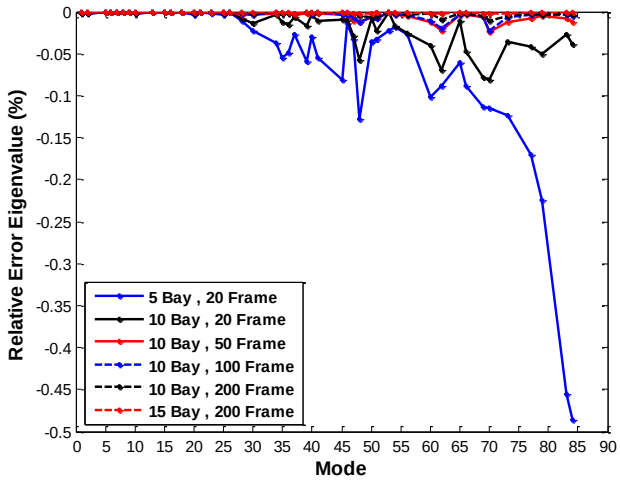


Figure 4.53. Relative errors of the natural frequencies for different combinations of bay-frame fixed-interface mode numbers.

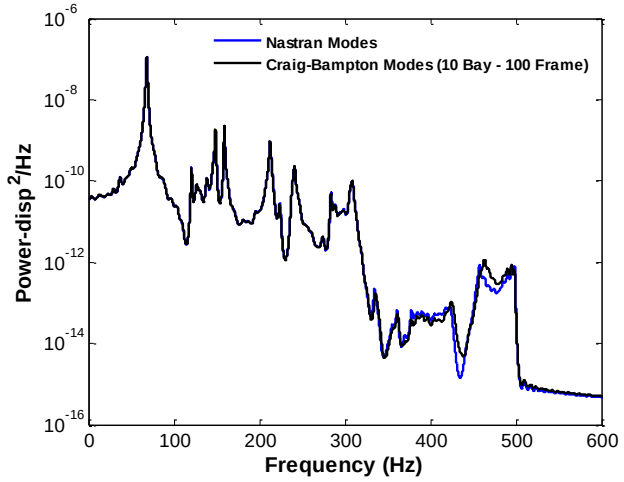


Figure 4.54. Power spectral density of the transverse (T3) deflection at the middle point of bay 5. Craig-Bampton model and finite element ("Nastran Modes"), *SPL* =106dB.

Notwithstanding the good prediction of the linear dynamics of the entire system by the "10 Bay, 100 Frame" model, the large number of fixed-interface frame modes and most importantly the large number of constraint modes deserve a closer examination. The use of a methodology to reduce the number of fixed-interface frame modes and constraint modes was explored next.

In order to reduce the large number of fixed-interface frame modes two alternatives were explored. The first one consisted of assessing the effect of the mass of the frame-longeron substructure (substructure 11) on the natural frequencies of the original mode shapes of the entire structure. To this end, the mass of the frame in the Craig-Bampton computations was divided by different factors and the resulting natural frequencies in the band [0,500]Hz were compared. A small effect would suggest the possibility of statically condensing the fixed-interface frame modes. However, as seen in Fig. 4.55 the effect was not negligible.

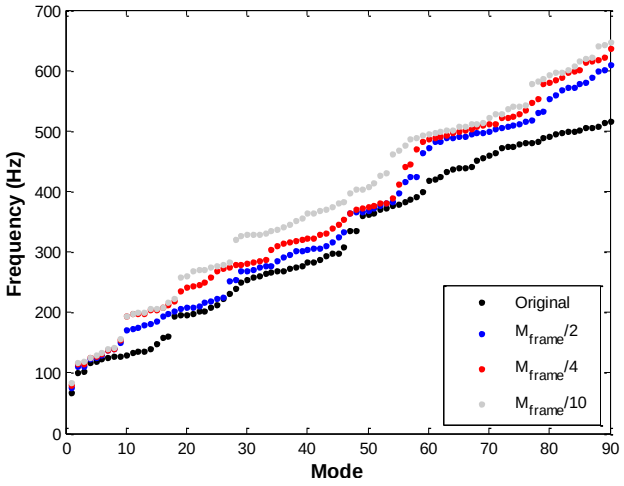


Figure 4.55. First 90 natural frequencies for different scaling factors of the frame-longeron mass matrix: 1, 0.5, 0.25, and 0.10.

The frame-longeron substructure is formed by 4 equal longerons and frames. Therefore, one would expect to have families of modes with natural frequencies that are close to each other (e.g., one mode with motions localized to longeron 1 and another localized to longeron 2, and so on). This can be seen in Fig. 4.56, which is a plot of the first 200 natural frequencies of the fixed-interface modes of the frame-longeron substructure. The first 12 modes have frequencies in the [0,500]Hz band of excitation, so these modes were kept as they would be directly excited. Then, the frame deflections from the first 89 system modes (i.e., those with natural frequencies within the [0,500]Hz band) were obtained, the first 12 fixed-interface modes were extracted, and a POD analysis of the residual was performed. Shown in Figs. 4.57-4.58 are the relative errors of the transverse component of the skin degrees-of-freedom and of the natural frequencies for different numbers of POD modes. The difference between including 40 and 50 POD modes was found to be very small; therefore, the number of fixed-interface modes was reduced from 100 to 52 (40 POD modes plus the 12 in-band normal modes).

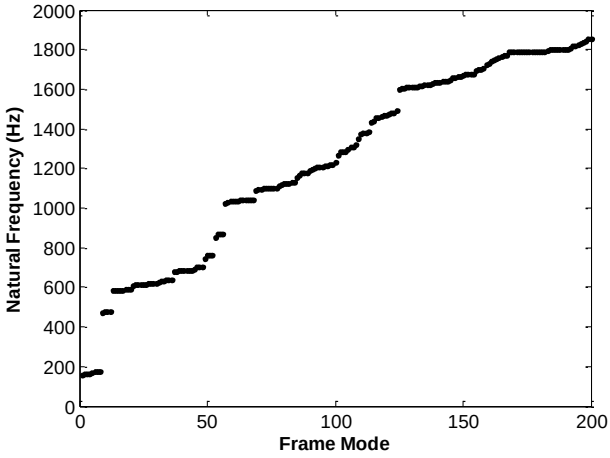


Figure 4.56. First 200 natural frequencies of the fixed-interface frame modes.

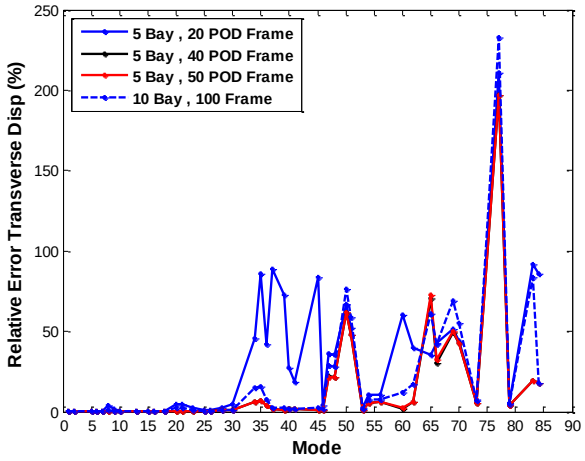


Figure 4.57. Relative errors of the transverse (normal) component of the skin degrees-of-freedom for different number of fixed-interface frame mode numbers.

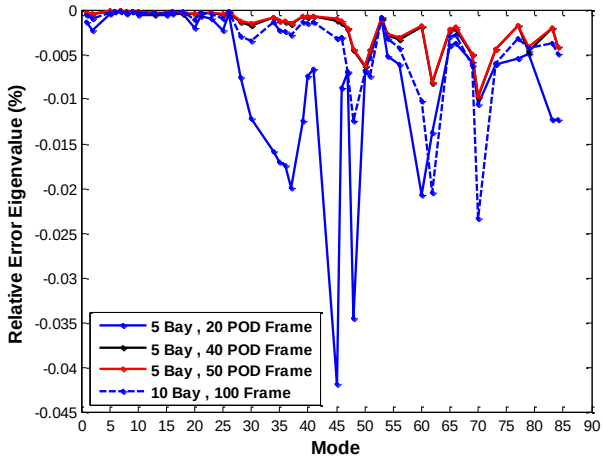


Figure 4.58. Relative errors of the natural frequencies for different number of fixed-interface frame mode numbers.

Next, it was desired to use the full model reduction from Eqs. (4.11)-(4.15) to express the response of the interface in terms of a reduced order model. By expressing the response of the interface in terms of a reduced order model, a substantial reduction in the number of interface degrees-of-freedom was expected. Furthermore, in terms of physical coordinates, the constraint modes are sensitive to the level of mesh refinement; in addition, mesh refinement would also affect the number of interface degrees-of-freedom and consequently the number of constraint modes. On the other hand, the modes of a reduced order model are associated to a natural frequency, which for the low frequency modes is not very sensitive to mesh refinement assuming that the original mesh size is appropriate.

Shown in Fig. 4.59 are the first 80 natural frequencies of the constraint modes computed from Eq. (4.12). There are 36 constraint modes in the frequency band [0,500]Hz that must be included since they could be directly excited by the dynamic loading. Shown in Figs. 4.60-4.61 are the relative errors of the transverse component of the skin panel degrees-of-freedom and of the natural frequencies for different numbers of constraint modes. Approximately 150 constraint modes were needed to match the results obtained with the full set of constraint modes and there were 114 constraint modes outside of the [0,500]Hz frequency band. Therefore, the POD approach used to reduce the number of fixed-interface constraint modes was used. In a similar way, the 36 in-band constraint modes were extracted from the displacement of the boundary degrees-of-freedom of the first 89 global modes. Then, a POD analysis of the residual was performed. Shown in Figs. 4.62-4.63 are the relative errors of the transverse component of the skin degrees-of-freedom and of the natural frequencies for different numbers of POD modes. In order to recover the results obtained with the full set of constraint modes, 54 POD modes were required; a total of 90 constraint modes were selected.

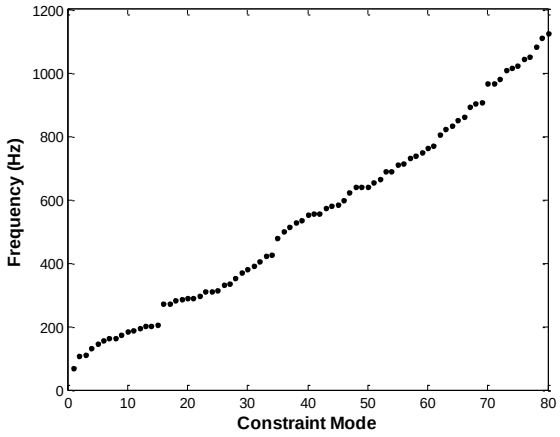


Figure 4.59. First 80 natural frequencies of the constraint modes from Eq. (4.12).

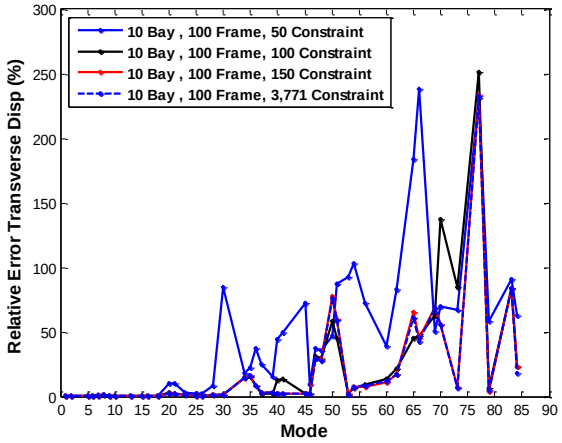


Figure 4.60. Relative errors of the transverse (normal) component of the skin degrees-of-freedom for different number of constraint modes.

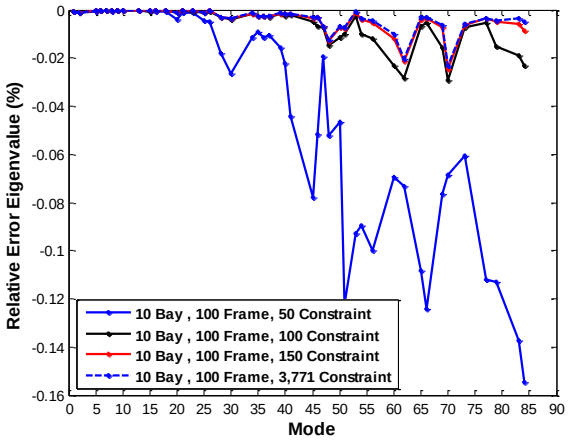


Figure 4.61. Relative errors of the natural frequencies for different number of constraint modes.

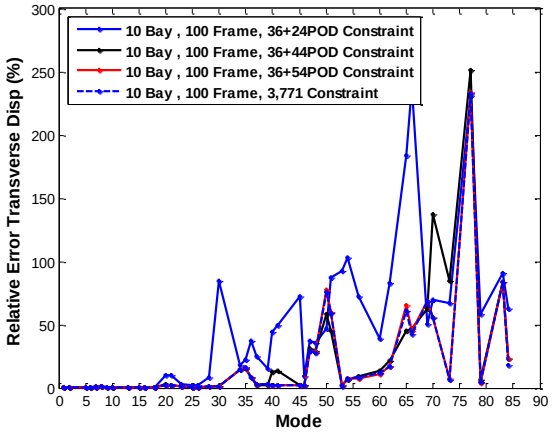


Figure 4.62. Relative errors of the transverse (normal) component of the skin degrees-of-freedom for different number of POD constraint modes.

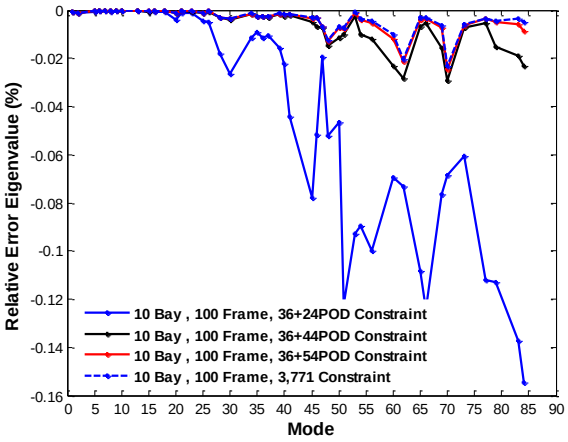


Figure 4.63. Relative errors of the natural frequencies for different number of POD constraint modes.

Therefore, the final reduced model consisted of 10 fixed-interface modes per bay, 52 fixed-interface frame modes (40 POD modes plus 12 in-band normal modes), and 90 constraint modes (54 POD modes plus 36 in-band normal modes). Shown in Fig. 4.64 is the power spectral density of the transverse displacement of the middle point of the middle panel, for the original 89 modes in the frequency band [0,500]Hz and the modes from the Craig-Bampton model. The matching of the dominant features of the response is excellent. However, the total size of the model (232 modes) is much larger than the 89 system modes that are within the frequency band [0,500]Hz. This is an important

challenge in the use of a *Bottom-Up Approach* which arises from the global aspects of the response of the 9-bay panel.

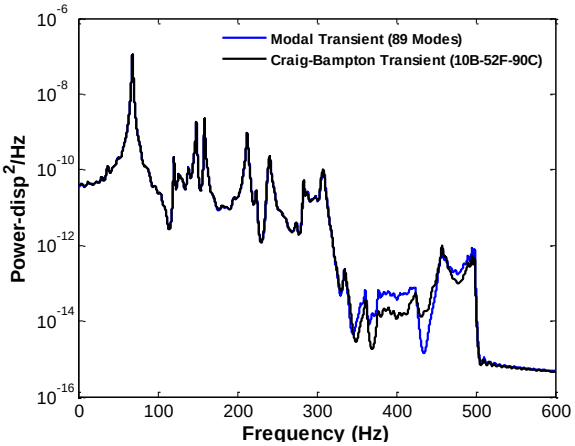


Figure 4.64. Power spectral density of the transverse (T3) deflection at the middle point of bay 5. Modal transient response (89 linear modes of the entire 9-bay panel) and Craig-Bampton model, *SPL* =106dB.

### 4.3.4. Nonlinear Problem

Shown in Figs. 4.65-4.69 are plots of the first five reduced constraint modes, computed from Eq. (4.12) and mapped back to physical coordinates by the transformation matrix $T_1$ (see Eq. 4.8). Also shown, are the first five modes of the entire 9-bay panel. Interestingly, the first four reduced constraint modes are very similar to their counterparts of the entire structure. Clearly, the motion of the interface nodes drives the motion of the bays and of the frame-longeron substructure. This global motion illustrates the strong coupling that exists between the bays. This in turn is a positive aspect, since it means that it will be difficult for the motion to get localized in a particular bay, which could be a concern from a fatigue failure perspective. On the other hand, from the nonlinear reduced order model perspective, the strong coupling between the bays implies that the nonlinear stiffness coefficients of the constraint modes will have an effect on the response.

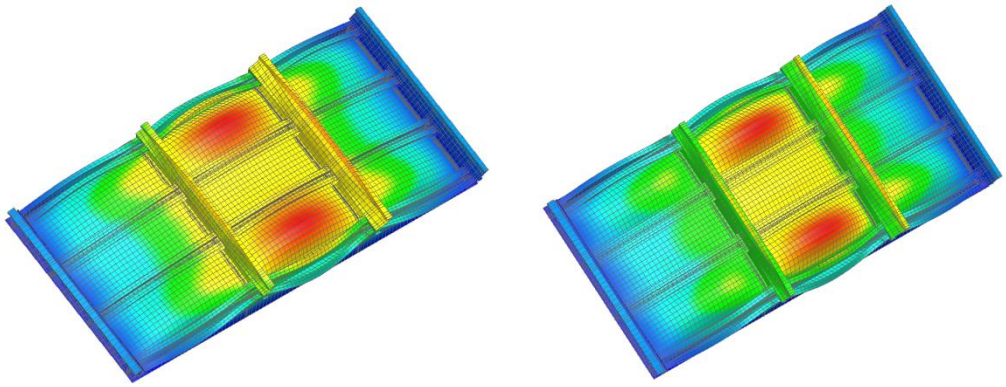

(a) (b)

Figure 4.65. (a) First reduced constraint mode (f = 69.7Hz) and (b) first mode of the entire 9-bay panel (f = 68.2Hz).

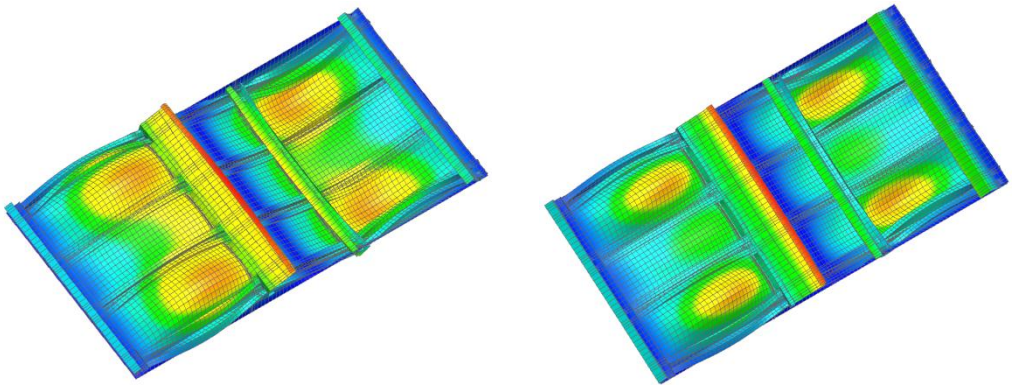

(a) (b)

Figure 4.66. (a) Second reduced constraint mode (f = 106.4Hz) and (b) second mode of the entire 9-bay panel (f = 99.7Hz).

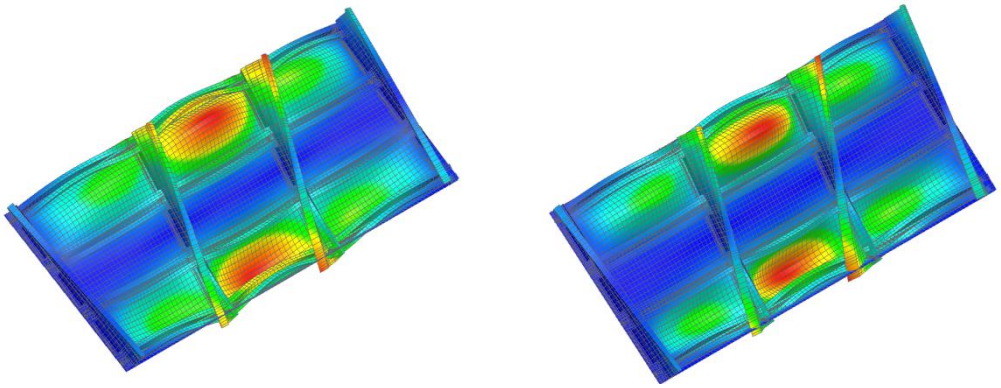

(a) (b)

Figure 4.67. (a) Third reduced constraint mode (f = 111.1Hz) and (b) third mode of the entire 9-bay panel (f = 103.3Hz).

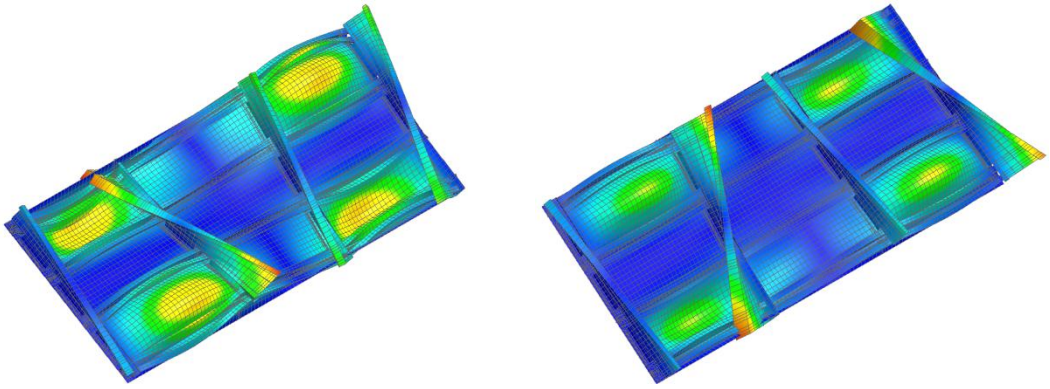

(a) (b)

Figure 4.68. (a) Fourth reduced constraint mode (f = 131.9Hz) and (b) fourth mode of the entire 9-bay panel (f = 116.5Hz).

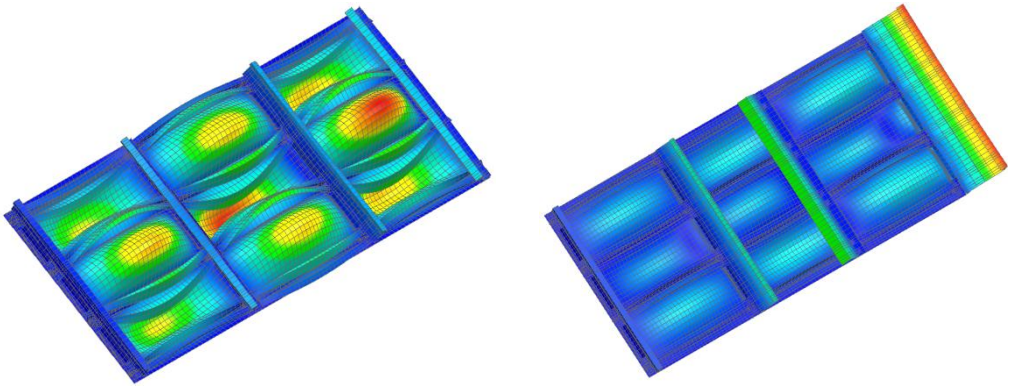

(a) (b)

Figure 4.69. (a) Fifth reduced constraint mode (f = 146.7Hz) and (b) fifth mode of the entire 9-bay panel (f = 120Hz).

Another challenge in the implementation of a *Bottom-Up* approach is in the nonlinear interaction between substructures, which needs to be built in the basis. Shown in Fig. 4.70 are the translational displacement magnitude of the entire model and the T2 component of the middle bay obtained from the nonlinear static analysis due to a uniform pressure loading of 0.6psi. Clearly, the middle bay is loaded by the top and bottom bays (bays 8 and 2, respectively).

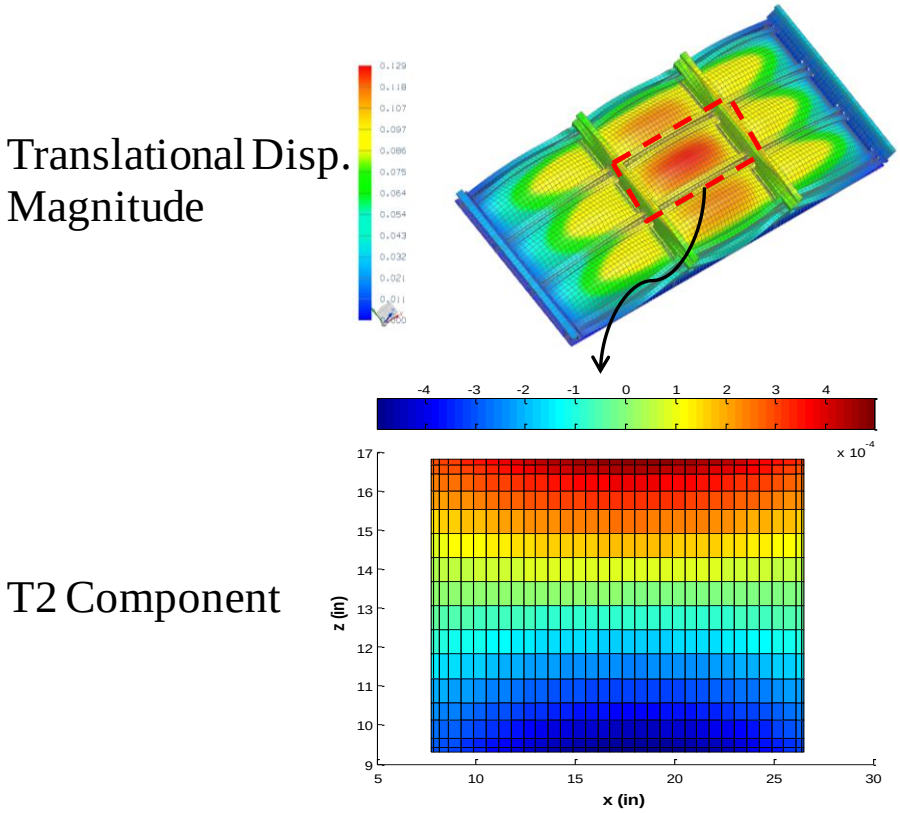


Figure 4.70. Contour plots showing the translational displacement magnitude of the entire 9-bay panel and the in-plane (T2) displacement at bay 5. Nonlinear static displacement due to a uniform pressure of 0.6psi.

The preloading of a substructure by its neighbors can be seen even if the transverse response is mostly localized to one substructure. An example of this can be seen in the localized response shown in Fig. 4.71, which corresponds to a "snapshot" obtained from the nonlinear dynamic response of the 144dB excitation level described earlier in this chapter. This is an interesting case because the response is mostly localized to bay 5; however, the in-plane loading of bays 2 and 8 in the T2 direction can be seen clearly.

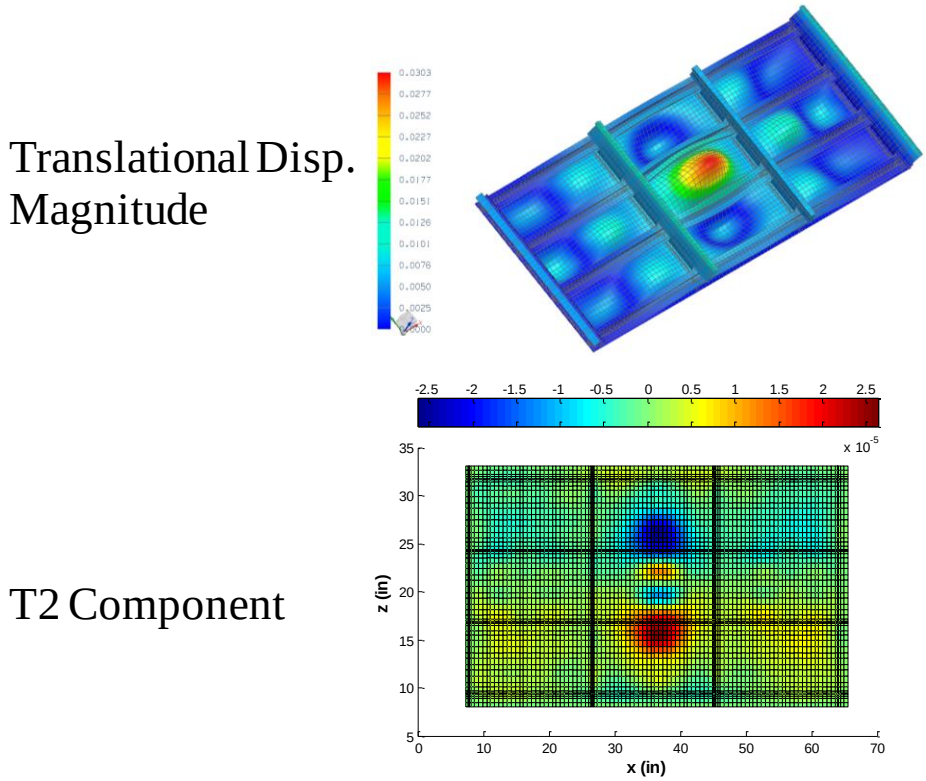


Figure 4.71. Contour plots showing the translational displacement magnitude of the entire 9-bay panel and the in-plane (T2) displacement of the skin panel. "Snapshot" from the nonlinear dynamic response at the 144dB excitation level.

As shown in Fig. 4.72, the preloading of a bay induced by the nonlinear interaction between bays not only leads to significant differences with respect to the original dual construction, but also with respect to duals from different bays. The preloaded duals shown in Fig. 4.72 were obtained by imposing boundary displacements in all directions, in addition to loading of the interior degrees-of-freedom with forces proportional to the first mode of the clamped-clamped bay. The boundary displacement was chosen as the nonlinear static response obtained from a load proportional to the first linear mode of the entire system (i.e., the loading used for the computation of the 1-1 dual of the monolithic ROM). Furthermore, 6 different loading factors $\alpha_i^{(m)}$ were used, half positive and half negative, and leading to peak deflections ranging from 0.9 to approximately 1.5 skin panel thicknesses. The loading of the interior degrees-of-freedom

,with forces proportional to the first modes of the clamped-clamped bay, consisted of 12 different loading factors $\alpha_i^{(m)}$, half positive and half negative, which led to overall peak transverse deflections ranging from 1.5 to approximately 2.2 skin panel thicknesses. Finally, the contribution from the reduced constraint modes in the representation of the interface displacement was subtracted, and the residuals of the 12×3 deflections per bay, after projection on the 10 linear fixed-interface modes identified above, were analyzed by POD.

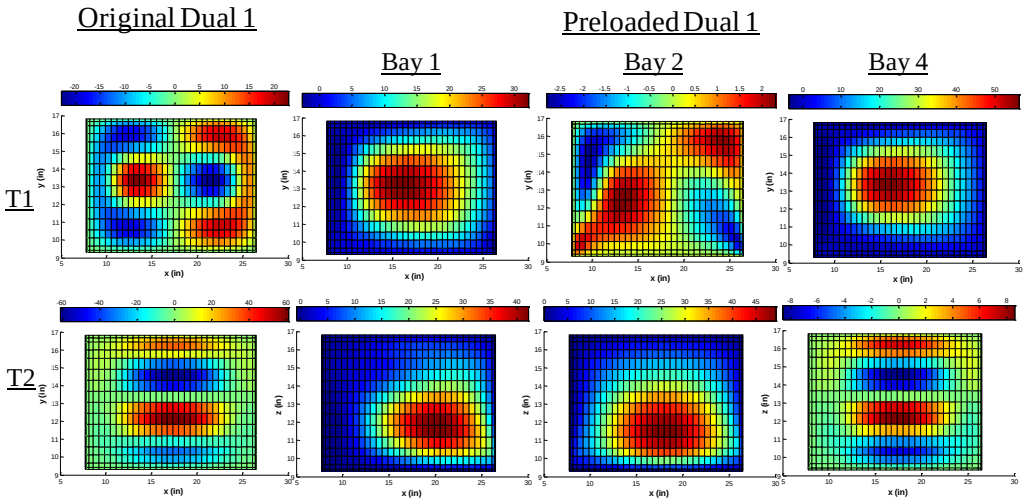


Figure 4.72. In-plane components of the 1-1 dual computed with and without preloading of the interface.

The previous discussion highlights the importance of extending the dual modes concept to include preloading of a substructure by its neighbors. The global features of the response of the 9-bay panel are dominant over the localized characteristics, which was seen in that the modes from the monolithic ROM were a more compact basis than the substructure modes from the previous section. Similarly, the introduction of the preloaded duals by themselves did not lead to a satisfactory reduction of the representation error as compared to the monolithic ROM.

The physical challenges observed here indicate that the representation of the global response from a *Bottom-Up* perspective is not more efficient than using the monolithic ROM. These findings also indicate that a key aspect for the multi-scale modeling of the 9-bay panel is in the representation of its global response. In this light, future work should explore the possibility of following a *Top-Down* multi-scale approach. In this case, the global response would be approximated (macro-scale) and then, this information would be used to compute the response of a particular bay (meso-scale).

# CHAPTER 5

# REDUCED ORDER MODELING FOR THE NONLINEAR GEOMETRIC RESPONSE OF PANELS WITH GEOMETRIC DISCONTINUITIES

## 5.1. Introduction

The purpose of this chapter is to assess the ROM capabilities for problems in the micro-scale. As mentioned in Chapter 1.3, problems in the micro-scale lead to localizations of the stress field. The source of these localizations may arise from cracks, debondings, fasteners, shock impingement points, etc. The main question to be addressed here is: Can a displacement-based ROM capture a localized stress distribution? In addition, the following phenomenological will be the focus of this chapter:

1) Is the displacement field affected by the local defect?
2) Does the defect need to be accounted for in the displacement?
3) Can a local enrichment of the stress be developed?

## 5.2. Models for Validation: Notched and Virgin Panel Models

A beam-like panel was considered here with and without a stress "hot spot", with the properties of the beam provided in Table 5.1. The panel was assumed to exhibit clamped-clamped boundary conditions and to be subjected to a uniform pressure of varying magnitude.

A rounded notch of length equal to one-fourth of the beam thickness was placed at 30% of the length of the beam (henceforth referred to as the notched beam) and along its entire width as shown in Figs. 5.1 and 5.2. Clearly, plane stress conditions cannot be assumed to exist on the *x*-*z* plane since it is not a thin membrane. On the other hand, plane strain conditions do not exist since this is not a long body problem. Therefore, the structure was discretized throughout its entire domain with 8-node brick elements (CHEXA in NX/Nastran), and 14 such elements were used along the width of

the beam. Along the length, the notched beam was divided in different parts, as shown in Fig. 5.1, to capture the local effects of the notch without excessive meshing away from that zone. Away from the notch (parts (a) and (c) in Fig 5.1), 4 elements were used through the thickness of the beam and a uniform division along the length was performed with 20 elements for part (a) and 47 elements for part (c). The finer meshing around the notch (part (b) in Fig 5.1) is shown in Fig. 5.2(a). Note further from this figure that the notch is rounded to avoid any plasticity in its vicinity, which is not considered in this first effort. The purpose of this work was to validate the reduced order modeling strategy, therefore, a very fine mesh was not used in order to accelerate the finite element computations.

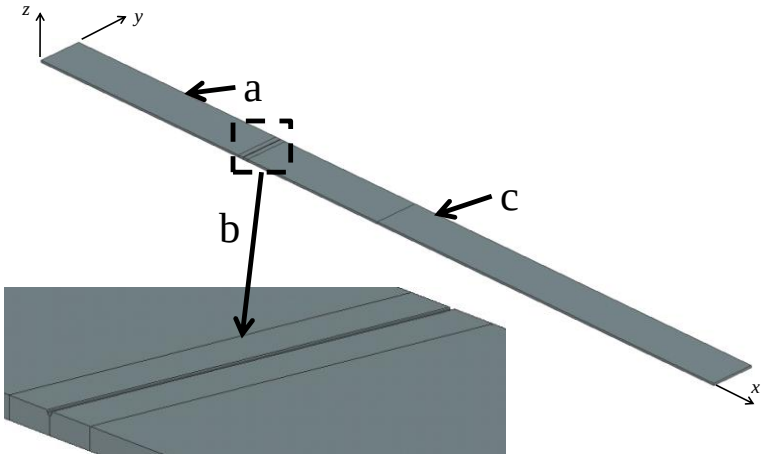


Figure 5.1. Notched beam model: Part (b) shows the zone near the notch with a finer mesh than parts (a) and (c) which are away from the notch.

A virgin beam model was also considered and, for ease of comparison, its meshing was selected to be identical to the one of the notched beam but with the notch filled with CHEXA elements, see Fig. 5.2(b), and with the same material properties, see Table 5.1.

Table 5.1. Clamped-Clamped Beam Properties

| | |
|---|---|
| Beam Length | 0.2286 m |
| Cross-section Width | 0.0127 m |
| Cross-section Thickness | $7.88\ 10^{-4}$ m |
| Density | 2700 kg/m$^3$ |
| Young's Modulus | 73,000 MPa |
| Shear Modulus | 27,730 MPa |

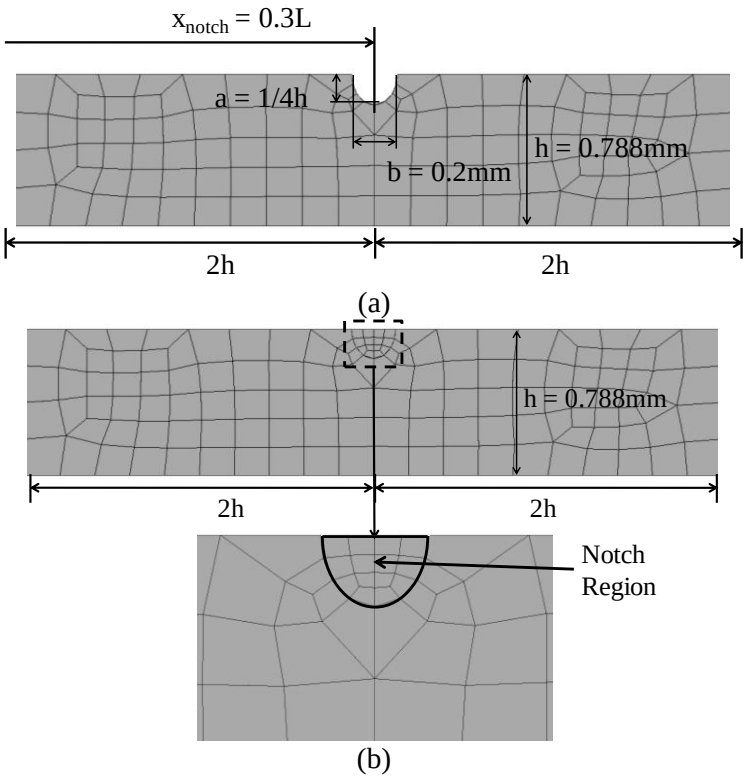


Figure 5.2. Geometry and finite element mesh near the notch region: (a) notched beam and (b) virgin beam. Where $L$=0.2286m and $h$=7.88x10$^{-4}$m.

### 5.3. Reduced Order Basis: Notched and Virgin Panels

It was first of interest to compare the basis functions of the reduced order models, i.e., the transverse and duals modes, of the virgin and notched beams to assess the effects, local and/or global, of the notch.

The transverse linear modes were first investigated and were obtained, for the two beams, from a normal modes solution in NX/Nastran (SOL 103). The natural

frequencies of the first 4 symmetric modes of the two beams are shown in Table 5.2. As expected, given the small size of the notch, its effect on the first few natural frequencies is very small.

Table 5.2. Natural frequencies along with relative error between notched and virgin beams.

| Mode No. | Virgin Beam (Hz) | Notched Beam (Hz) | Relative Difference (%) |
|---|---|---|---|
| 1 | 81.561 | 81.551 | 0.010 |
| 3 | 442.075 | 441.900 | 0.040 |
| 6 | 1098.527 | 1097.261 | 0.110 |
| 10 | 2061.725 | 2061.693 | 0.001 |

The transverse and in-plane (along the length of the beam) components of the first mode shape along one of the top edges of the beams ($y=0$, $z=h$) are shown in Figs. 5.3-5.4. The first observation to be drawn is that the notch does not affect noticeably the transverse displacements, but appears to induce a sharp peak in its in-plane counterpart. However, this peak is an artifact of the geometry, i.e., the notched beam data presented includes the displacement at the nodes along the flat edge of the beam but also those along the faces of the notch. Since these points are much closer to the neutral axis of the beam, their in-plane displacements are expected to be smaller as seen in Fig. 5.5. Plotting the same nodal displacements for the virgin beam, see Figs. 5.6-5.7, confirms this explanation of the peak.

The linear modes of the structure only represent one part of the basis, modeling primarily the transverse displacements, while the dual modes (see [9,12,14]) capture the nonlinearly induced in-plane motions. In this light, it was also desired to assess the effects of the notch on these dual modes. Thus, the 4 dual modes corresponding to the 4 linear modes were created, for both notched and virgin beams.

Shown in Figs. 5.8-5.9 are the transverse and in-plane components of the first (dominant) dual. Note that the notch is most present in the *transverse* component, see

Fig. 5.8, of the dual mode which is quite different for the notched and virgin beams. In particular, note for the former the presence of a large, broad (as measured by the width of the notch) peak at the location of the notch. On the contrary, the in-plane components of this dual mode are almost unaffected by the notch, see Fig. 5.9. The most noticeable difference in the in-plane displacement is a jump occurring at the location of the notch, as seen in Fig. 5.10. Similar observations were drawn for the other 3 dual modes.

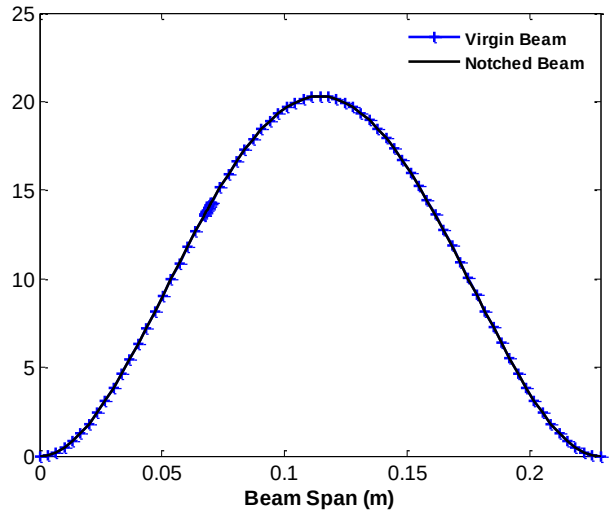


Figure 5.3. Transverse component of the first linear mode along one of the top edges of the beam.

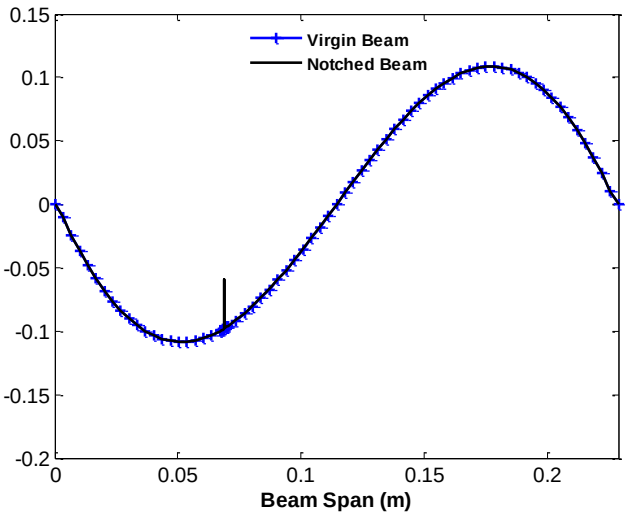


Figure 5.4. In-plane component of the first linear mode along one of the top edges of the beam.

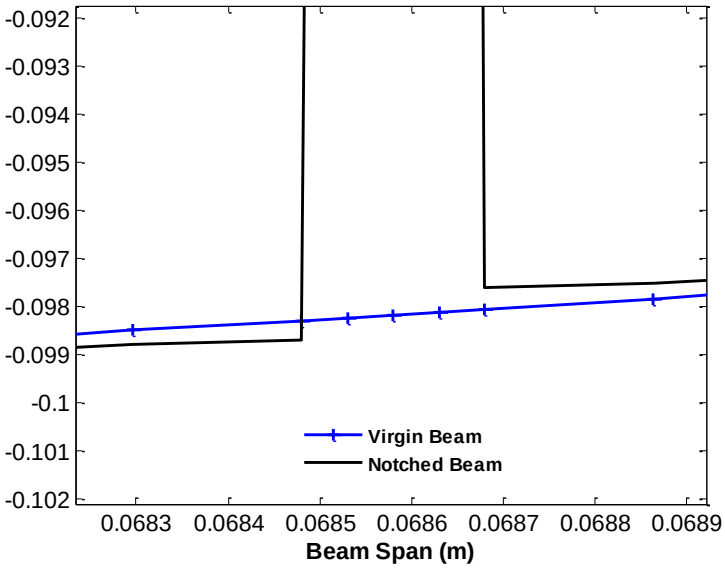


Figure 5.5. Zoomed-in view of the in-plane displacements near the location of the notch.

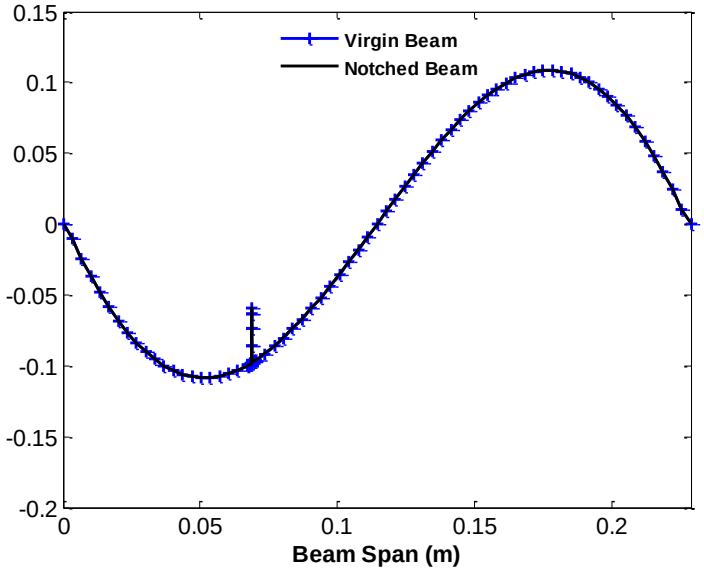


Figure 5.6. In-plane component of the first linear mode, curves correspond to displacements at the same nodes.

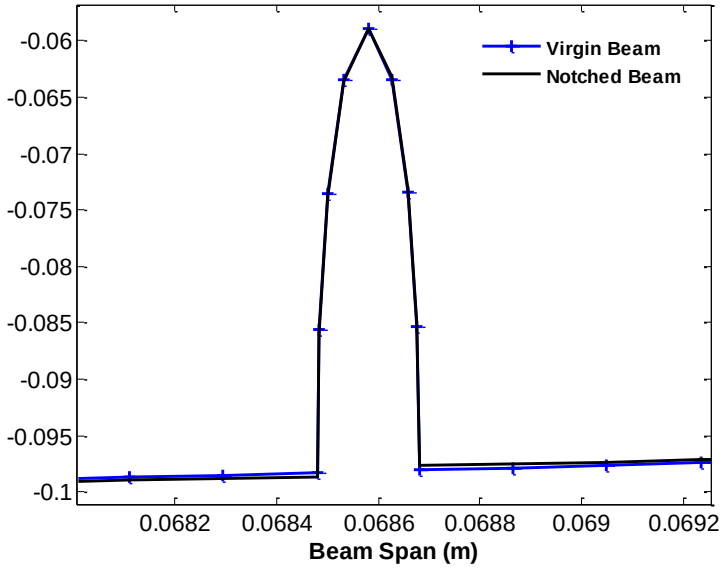


Figure 5.7. Zoomed-in view of the in-plane component, curves correspond to displacements at the same nodes.

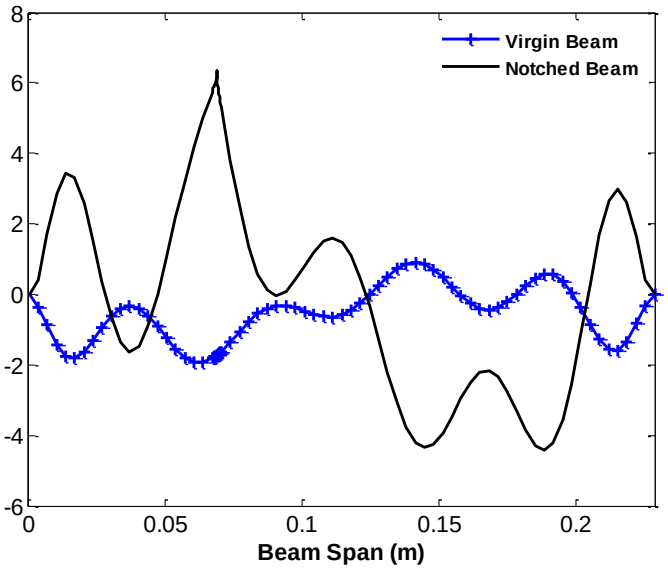


Figure 5.8. Transverse component of the first dual mode along one of the top edges of the beam.

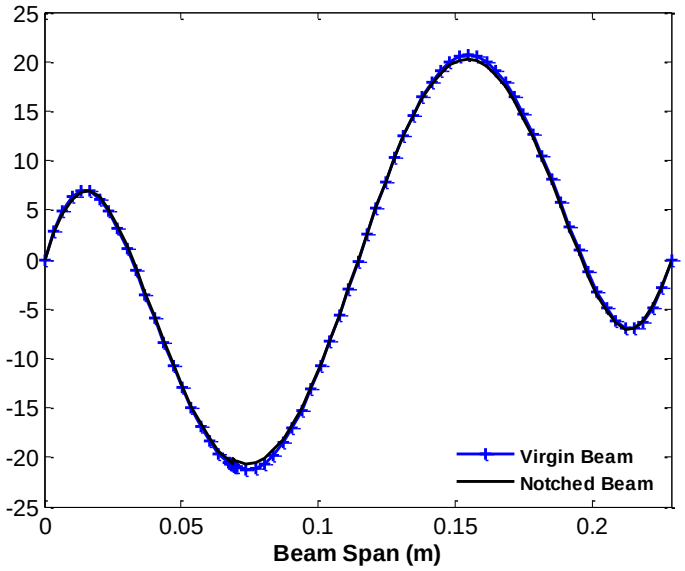


Figure 5.9. In-plane component of the first dual mode along one of the top edges of the beam.

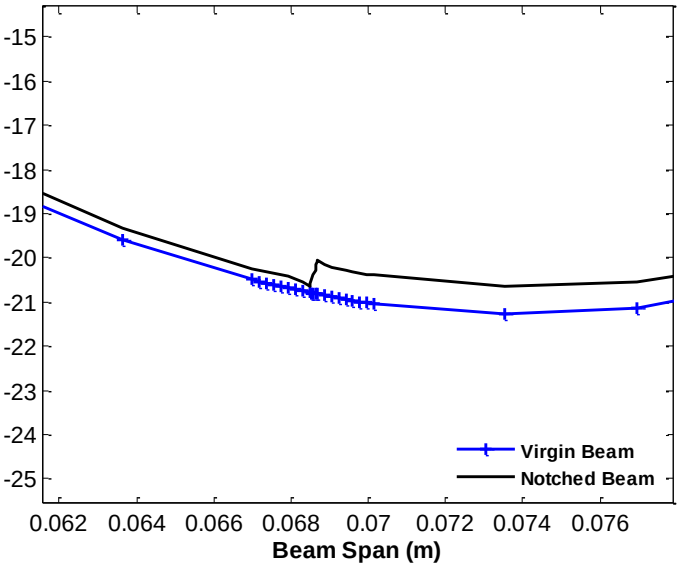


Figure 5.10. Zoomed-in view of the in-plane displacements near the location of the notch.

Using the 4 linear and 4 dual modes analyzed above, reduced order models were built for both notched and virgin beams with the coefficients estimated from the stiffness evaluation procedure of [28] as modified in [10-12].

### 5.4. Static Validation: Displacement and Stress Fields

To assess the adequacy of the reduced order models obtained and assess the effects of the notch, the beams were loaded with a uniform pressure acting on the bottom surface. Two different pressures were chosen, 2.6kPa and 17kPa, which led to peak transverse displacements of approximately 2 and 4 beam thicknesses, well within the nonlinear range. The static responses were computed with the reduced order model as well as by a nonlinear NX/Nastran analysis (SOL 106). Shown in Figs. 5.11-5.14 is a comparison of the predicted transverse and in-plane displacements at the beam's upper and lower edges. Clearly, the matching is excellent for both transverse and in-plane displacements, even in the direct vicinity of the notch (see Fig. 5.15). In Figs. 5.15-5.16, the response of the virgin beam was plotted at the same node locations as the response of the notched beam. Interestingly, the reduced order model of the virgin beam does an excellent job in capturing the in-plane displacement field in the notch region.

Figures 5.17-5.20 show the static response of the beam to pressures equal to -2.6kPa and -17kPa, applied on the bottom surface of the beam, and leading to peak transverse displacements of -2 and -4 beam thicknesses. Clearly, the matching is excellent for both cases, and once more the reduced order model of the virgin beam does an excellent job in capturing the in-plane displacement field in the notch region.

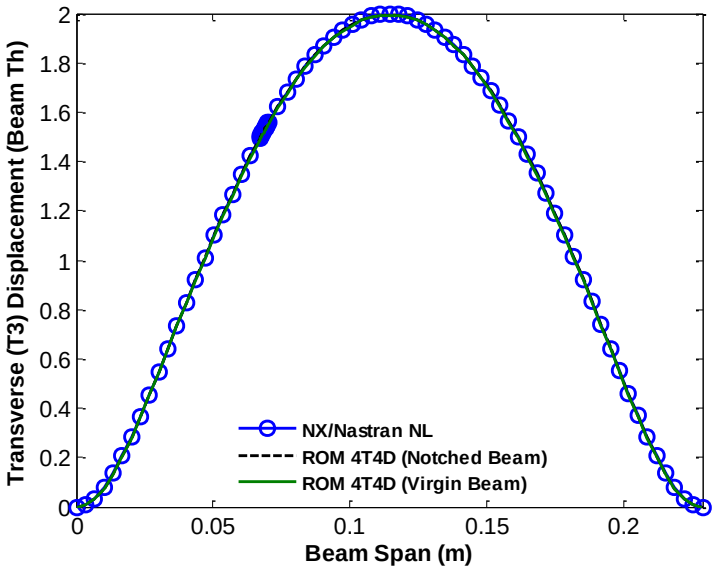


Figure 5.11. Transverse displacements at the top ($y=0$, $z=h$) edge of the beam induced by a uniform pressure of 2.6kPa on its bottom surface. Reduced order models ("ROM 4T4D"), nonlinear static FEA ("NX/Nastran NL").

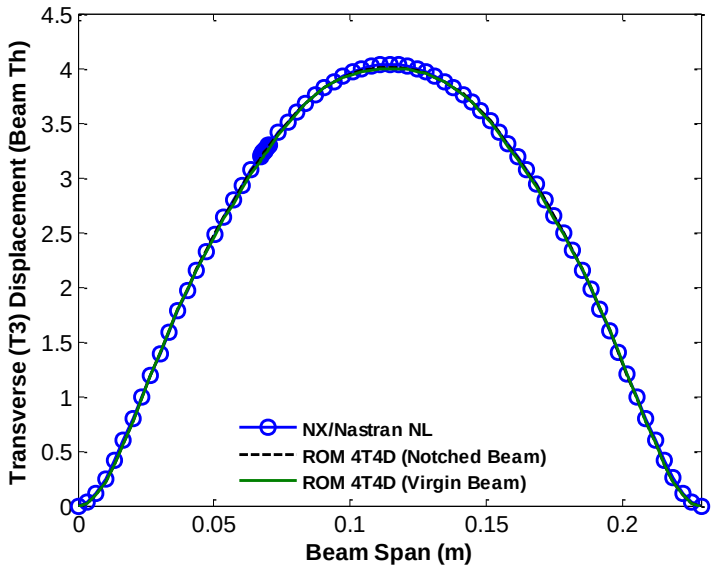


Figure 5.12. Transverse displacements at the top ($y=0$, $z=h$) edge of the beam induced by a uniform pressure of 17kPa on its bottom surface. Reduced order models ("ROM 4T4D"), nonlinear static FEA ("NX/Nastran NL").

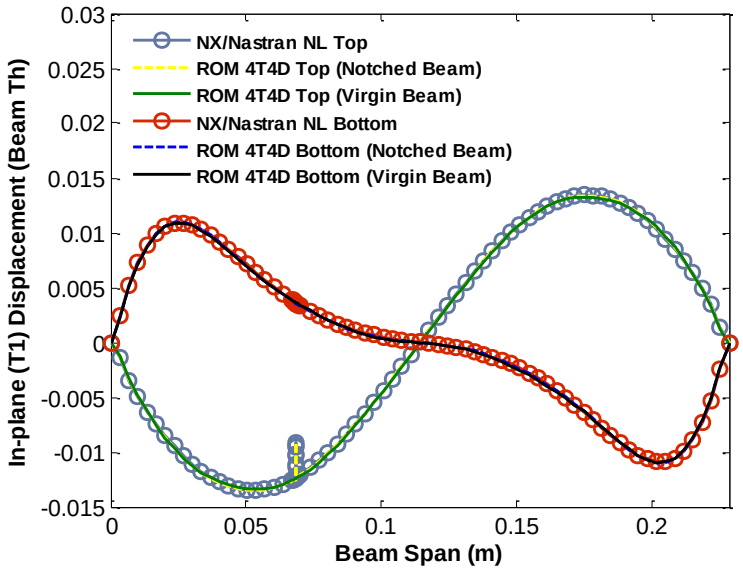


Figure 5.13. In-plane disp. at the top (*y=0, z=h*) and bottom (*y=0, z=0*) edges of the beam induced by a uniform pressure of 2.6kPa on its bottom surface. Reduced order models ("ROM 4T4D"), nonlinear static FEA ("NX/Nastran NL").

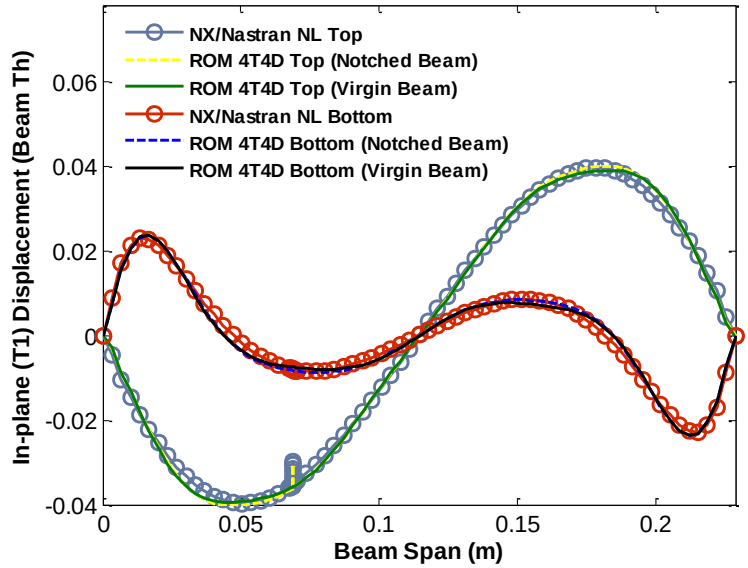


Figure 5.14. In-plane disp. at the top (*y=0, z=h*) and bottom (*y=0, z=0*) edges of the beam induced by a uniform pressure of 17kPa on its bottom surface. Reduced order models ("ROM 4T4D"), nonlinear static FEA ("NX/Nastran NL").

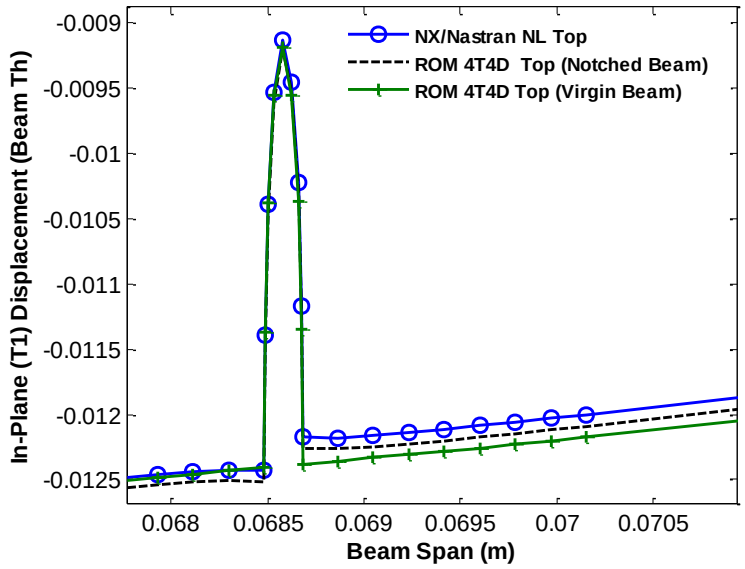


Figure 5.15. Close-up view of the in-plane disp. (T1) at the beam top edge ($y=0$, $z=h$) due to a uniform pressure of 2.6kPa. Reduced order models ("ROM 4T4D"), nonlinear static FEA ("NX/Nastran NL").

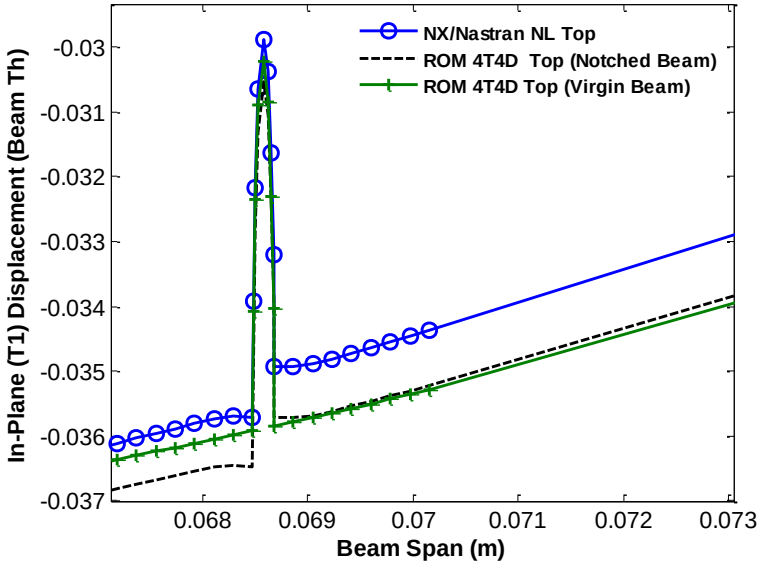


Figure 5.16. Close-up view of the in-plane disp. (T1) at the beam top edge ($y=0$, $z=h$) due to a uniform pressure of 17kPa. Reduced order models ("ROM 4T4D"), nonlinear static FEA ("NX/Nastran NL").

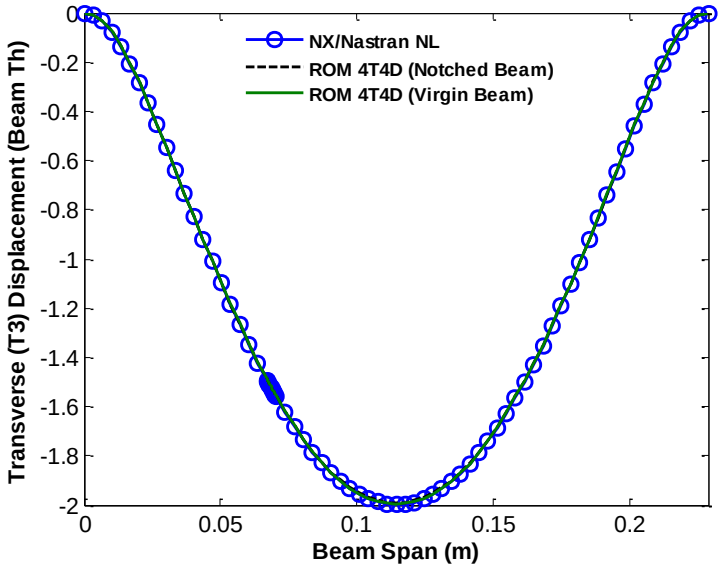


Figure 5.17. Transverse disp. at the top ($y=0$, $z=h$) edge of the beam induced by a uniform pressure of -2.6kPa on its bottom surface. Reduced order models ("ROM 4T4D"), nonlinear static FEA ("NX/Nastran NL").

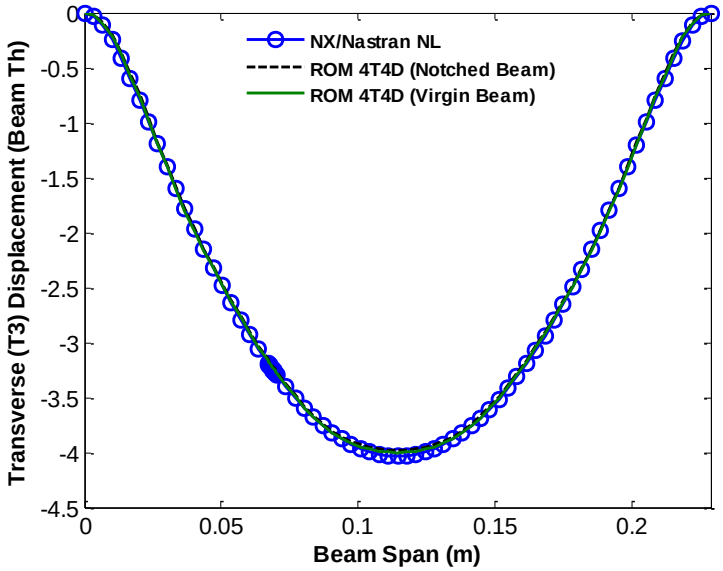


Figure 5.18. Transverse disp. at the top ($y=0$, $z=h$) edge of the beam induced by a uniform pressure of -17kPa on its bottom surface. Reduced order models ("ROM 4T4D"), nonlinear static FEA ("NX/Nastran NL").

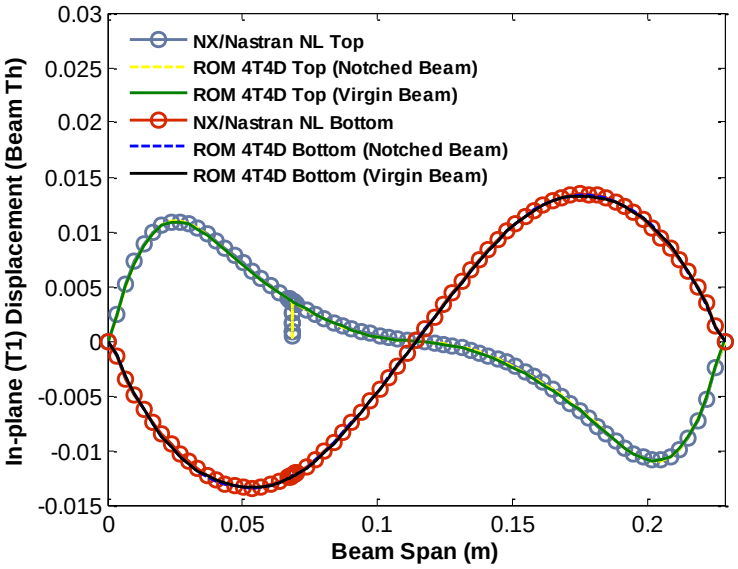


Figure 5.19. In-plane disp. at the top (*y=0, z=h*) and bottom (*y=0, z=0*) edges of the beam induced by a uniform pressure of -2.6kPa on its bottom surface. Reduced order models ("ROM 4T4D"), nonlinear static FEA ("NX/Nastran NL").

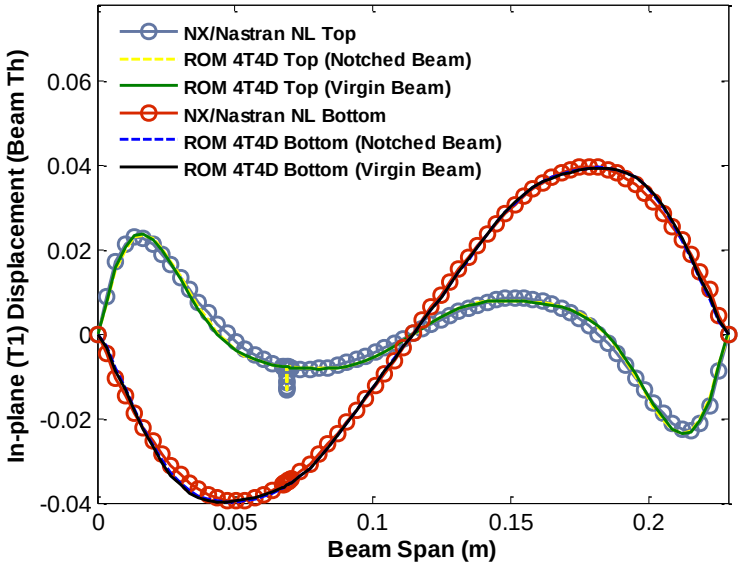


Figure 5.20. In-plane disp. at the top (*y=0, z=h*) and bottom (*y=0, z=0*) edges of the beam induced by a uniform pressure of -17kPa on its bottom surface. Reduced order models ("ROM 4T4D"), nonlinear static FEA ("NX/Nastran NL").

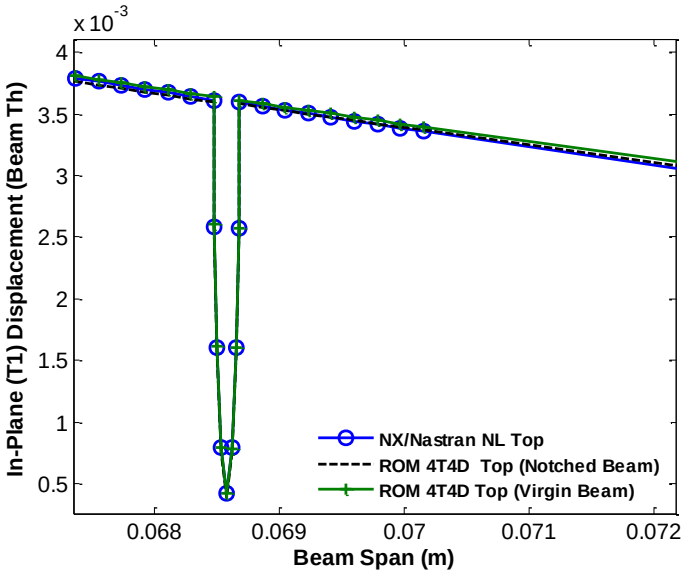


Figure 5.21. Close-up view of the in-plane disp. (T1) at the beam top edge ($y=0$, $z=h$) due to a uniform pressure of (a) -2.6kPa and (b) -17kPa. Reduced order models ("ROM 4T4D"), nonlinear static FEA ("NX/Nastran NL").

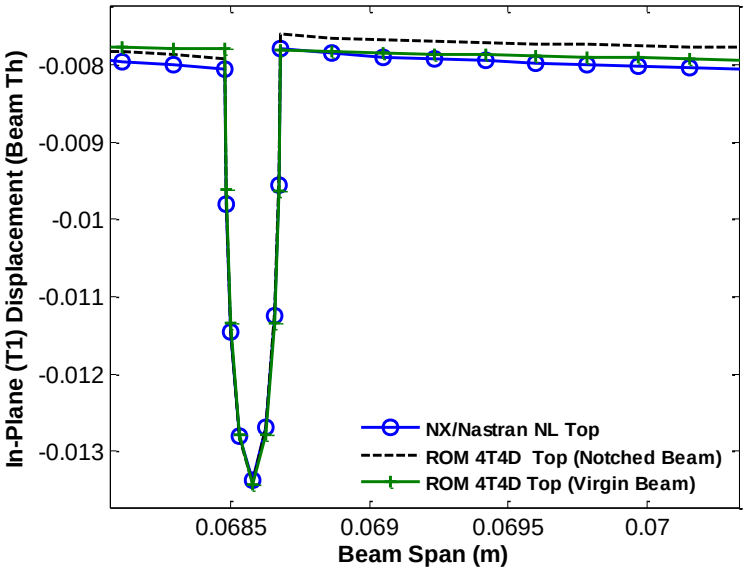


Figure 5.22. Close-up view of the in-plane disp. (T1) at the beam top edge ($y=0$, $z=h$) due to a uniform pressure of (a) -2.6kPa and (b) -17kPa. Reduced order models ("ROM 4T4D"), nonlinear static FEA ("NX/Nastran NL").

Table 5.3. Summary of prediction errors, notched beam and virgin beam ROMs.

| Peak T3 Disp (Beam Thicknesses) | Prediction Error Transverse (T3) Component (%) | | Prediction Error Transverse (T1) Component (%) | | Prediction Error Transverse (T2) Component (%) | |
|---|---|---|---|---|---|---|
| | Notched Beam | Virgin Beam | Notched Beam | Virgin Beam | Notched Beam | Virgin Beam |
| 2 | 0.2 | 0.4 | 1 | 1.4 | 2.4 | 3.4 |
| 4 | 0.5 | 0.9 | 3.9 | 3.7 | 5.9 | 7.4 |
| -2 | 0.3 | 0.3 | 1.4 | 1.4 | 3.4 | 3 |
| -4 | 1 | 0.6 | 3.8 | 3.9 | 7.4 | 7.1 |

Shown in Table 5.3 is a summary of the prediction errors for the three displacement components. The prediction errors were computed from Eq. 4.1. Results are shown for the ROMs of the notched and virgin beam. Clearly, the linear modes chosen to represent the transverse displacements, along with the modeling of the in-plane displacements by the duals, result in a very good matching of the transverse component with respect to NX/Nastran.

The previous results have demonstrated that the reduced order model of the notched beam is able to capture accurately the displacement field of this beam, thereby extending the existing validation cases of [9, 12 and 21-24]. Furthermore, it has been observed, not too unexpectedly, that the displacement fields of the notched and virgin beams are indeed very close to each other, suggesting that the latter could be used for the prediction of the response of the former. Before any such connection can be established, however, it is necessary to assess the capability of the notched beam reduced order model to capture the *stress* distribution of this beam.

To this end, shown in Figs 5.23-5.26 are the dominant stresses $s_{xx}$ along the top edge of the beam ($y=0$, $z=h$), as computed by the reduced order model of the notched beam, see Eq. (2.35), and by NX/Nastran nonlinear for all loading cases analyzed above. Clearly, the agreement is very good to excellent, even in the notch near field, as seen from the results in Tables 5.3-5.4. It is thus concluded from these validation cases that the

nonlinear geometric reduced order modeling technique developed is also applicable to notched panels for the prediction of both their displacement and stress fields.

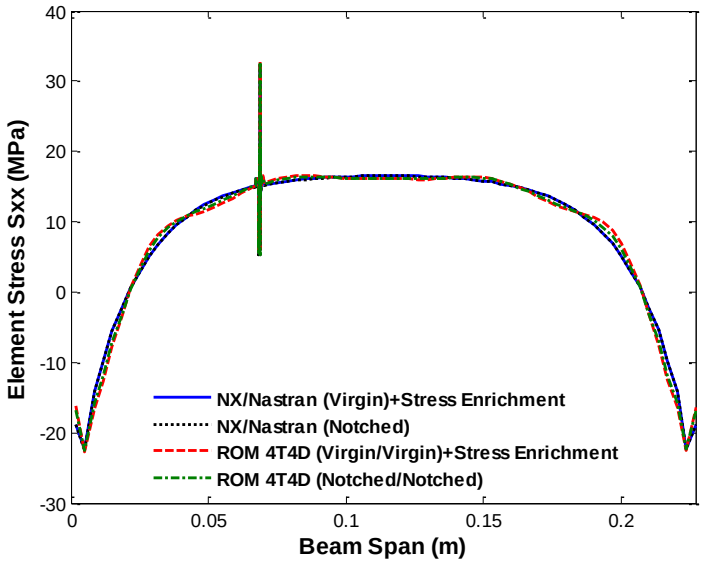


Figure 5.23. Element stress $S_{xx}$ near the beam edge at $y=0$, $z=h$, induced by a uniform pressure of 2.6kPa. Reduced order model with stress enrichment ("ROM 4T4D+Stress Enrichment)", nonlinear static FEA ("NX/Nastran").

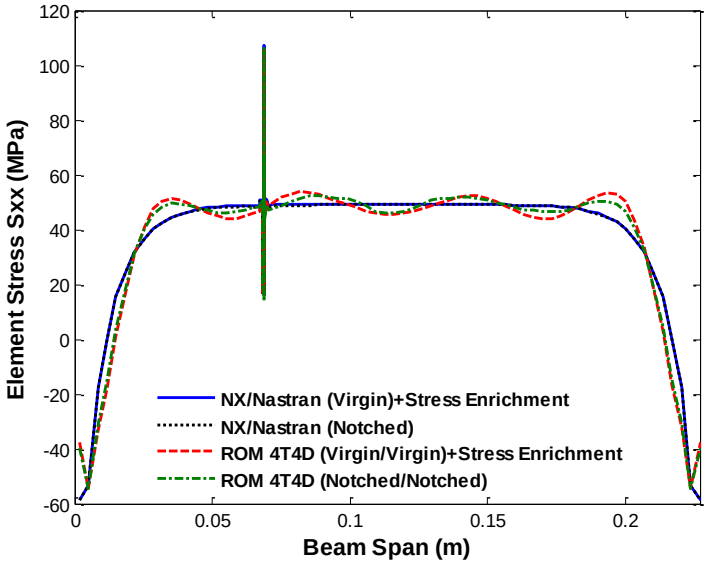


Figure 5.24. Element stress $S_{xx}$ near the beam edge at $y=0$, $z=h$, induced by a uniform pressure of 17kPa. Reduced order model with stress enrichment ("ROM 4T4D+Stress Enrichment)", nonlinear static FEA ("NX/Nastran").

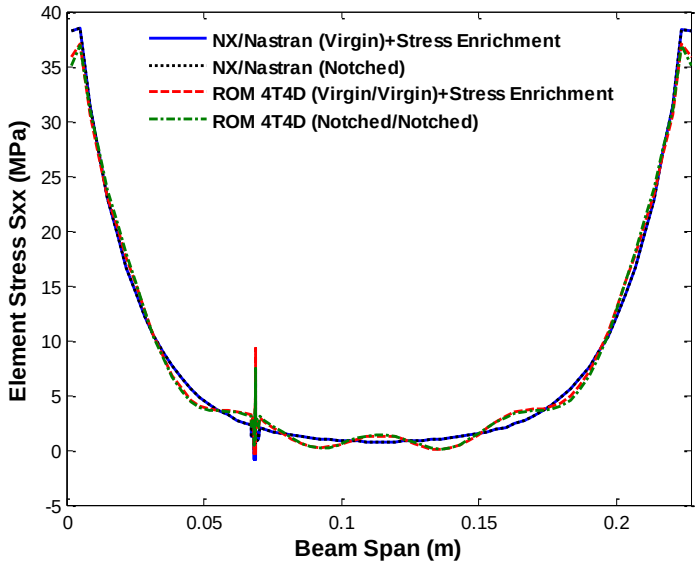


Figure 5.25. Element stress $S_{xx}$ near the beam edge at $y=0$, $z=h$, induced by a uniform pressure of -2.6kPa. Reduced order model with stress enrichment ("ROM 4T4D+Stress Enrichment)", nonlinear static FEA ("NX/Nastran").

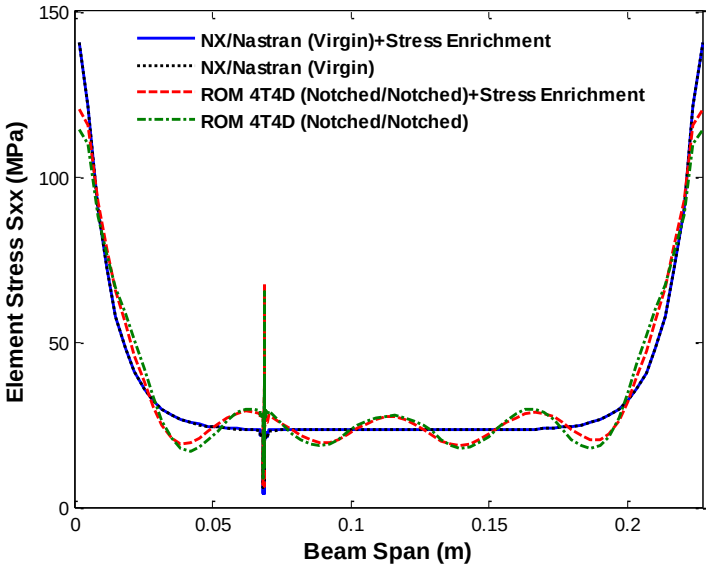


Figure 5.26. Element stress $S_{xx}$ near the beam edge at $y=0$, $z=h$, induced by a uniform pressure of -17kPa. Reduced order model with stress enrichment ("ROM 4T4D+Stress Enrichment)", nonlinear static FEA ("NX/Nastran").

### 5.5. Dynamic Displacement and Stress Fields

Lastly, a dynamic transverse loading was added and the response computed in NX/Nastran. The beam was subjected to a uniform pressure on its bottom surface varying

randomly in time as a white noise band-limited process in the frequency range [0,1042Hz] to simulate an acoustic loading. The acoustic excitation consisted of an overall sound pressure level (*OASPL*) of 147dB. Furthermore, to permit a close comparison between the NX/Nastran and ROM results, a simple Rayleigh damping model was adopted, i.e. for which the damping matrix is $D = \alpha M + \beta K$ with α=12.838/s and β=2.061E-6s. This selection led to damping ratios between 0.5% and 1.3% for all four transverse modes in the excitation band.

The power spectra of the transverse displacement at the middle of the beam and of the in-plane displacement at the beam quarter point, both at the upper edge (i.e., *y=0, z=h*) are shown in Figs. 5.27-5.29. Clearly, based on the matching of the power spectral density of the NX/Nastran results, the ROM of the notched beam and of the virgin beam match very well the dynamics of the beam. Interestingly, the matching of the power spectrum of the in-plane displacement along the T1 direction at the notch tip is very good as well, even for the ROM of the virgin beam.

The power spectral density of the dominant $S_{xx}$ element stresses, at different locations along the beam are shown in Figs. 5.30-5.32. Away from the notch, the power spectrum of both ROMs match NX/Nastran. Figure 5.32 shows clearly the amplification of the stress field at the notch. The power spectrum corresponding to the ROM of the notched beam matches its NX/Nastran counterpart very well.

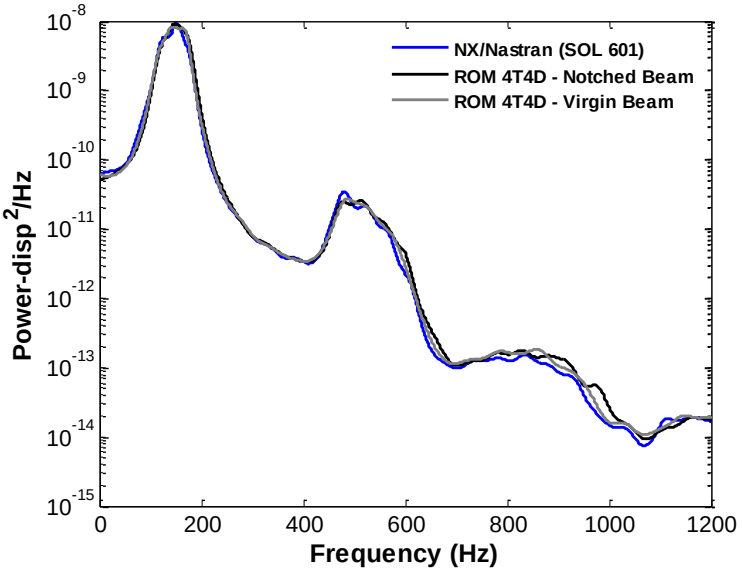


Figure 5.27. Power spectral density of the transverse displacement at the beam middle point, *x=1/2L*, *y=0*, *z=h* (*OASPL* = 147dB). Reduced order model ("ROM(4T4D)") and FEA ("NX/Nastran").

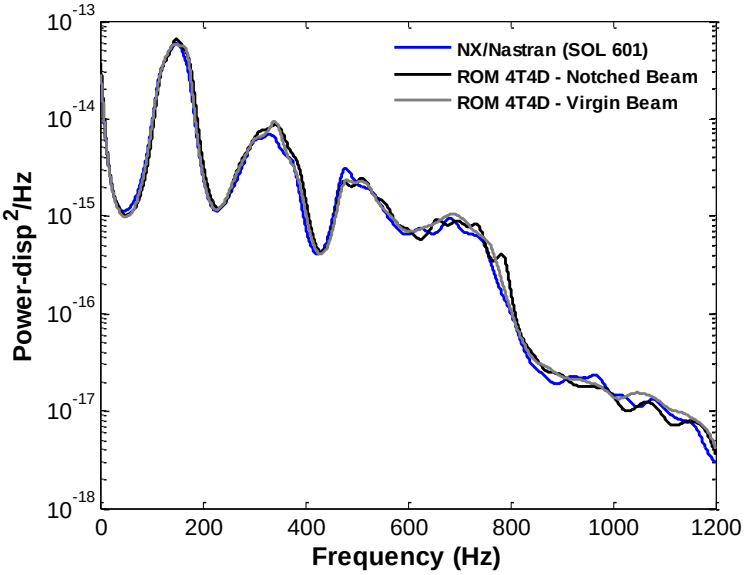


Figure 5.28. Power spectral density of the in-plane displacement at the notch tip (*OASPL* = 147dB). Reduced order model ("ROM(4T4D)") and FEA ("NX/Nastran").

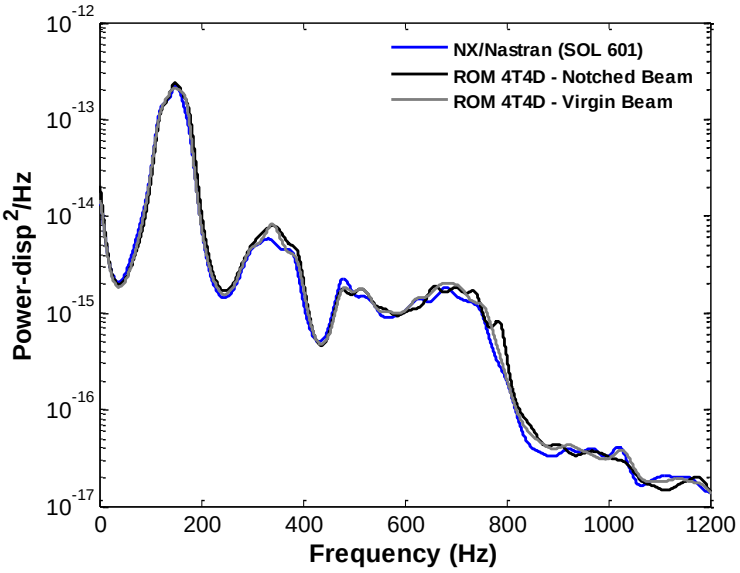


Figure 5.29. Power spectral density of the in-plane displacement at the beam quarter point, *x=1/4L*, *y=0*, *z=h* (*OASPL* = 147dB). Reduced order model ("ROM(4T4D)") and FEA ("NX/Nastran").

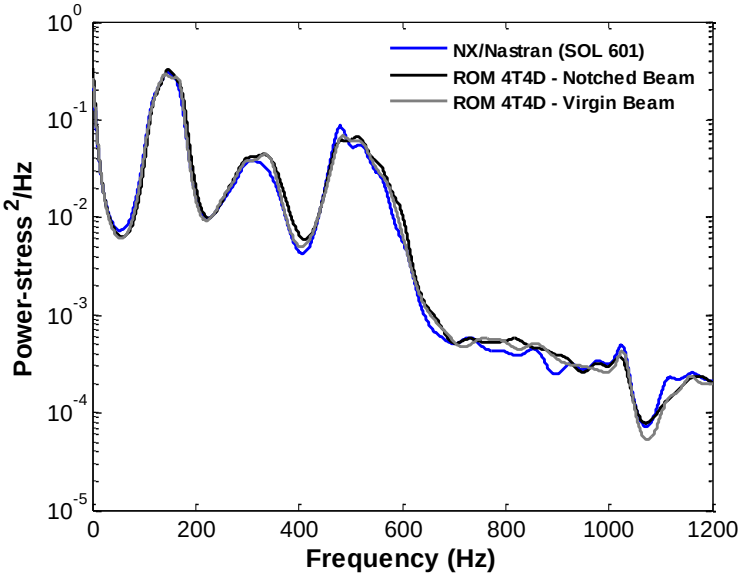


Figure 5.30. Power spectral density of the $S_{xx}$ element stress near the middle of the beam at *y=0*, *z=h* (*OASPL* = 147dB). Reduced order model ("ROM(4T4D)") and FEA ("NX/Nastran").

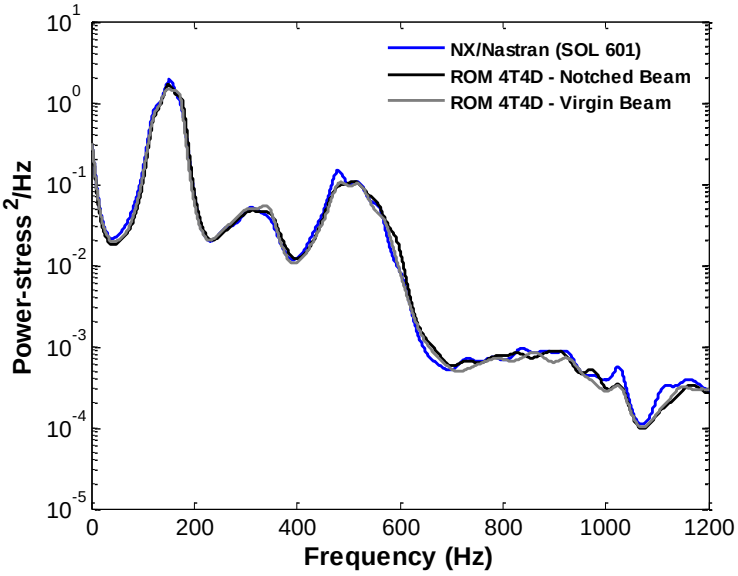


Figure 5.31. Power spectral density of the $S_{xx}$ element stress near the support of the beam at $y=0$, $z=h$ (*OASPL* = 147dB). Reduced order model ("ROM(4T4D)") and FEA ("NX/Nastran").

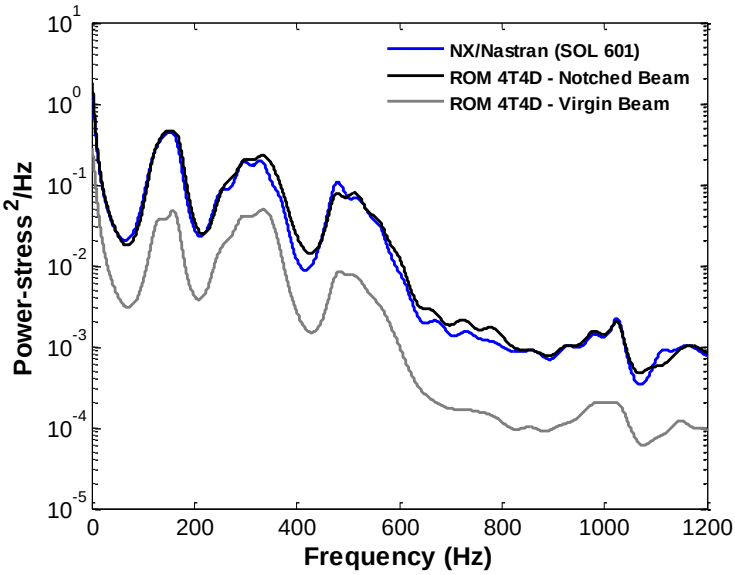


Figure 5.32. Power spectral density of the $S_{xx}$ element stress near the notch at $y=0$, $z=h$ (*OASPL* = 147dB). Reduced order model ("ROM(4T4D)") and FEA ("NX/Nastran").

### 5.6. Stress Field Local Enrichment

While the findings from the previous section provide a framework to carry out dynamic simulations at a much reduced computational cost, its applicability to study the propagation of a crack seems limited as the model, i.e., basis functions and coefficients,

would need to be updated as the crack propagates. For such analyses, it would be highly desirable to rely on a reference geometry, most simply the virgin beam, and enrich the solution by an extra component accounting for the existence and geometry of the crack.

The loading considered in the present validation cases, and representative of the applied loads on panels, leads primarily to bending and stretching (from the nonlinear effects) and thus a mode I fracture mode is dominant. Accordingly, it is proposed here to add to the virgin beam stress distribution, induced by the pressure loading, a term that accounts for the presence of the crack. Following a stress intensity factor perspective, it is suggested that this term, referred to as an enrichment, be computed as the increment of stress induced by the crack, for a loading corresponding to the in-plane stress distribution of the virgin beam in the vicinity of the crack. Further, this enrichment term will be computed in a linear static analysis. Effectively, this approach replaces the stress distribution of the virgin beam in the vicinity of the crack by a stress distribution of the cracked beam that smoothly connects to the virgin far-field behavior.

Two separate versions of this strategy were considered and assessed on the notched beam from previous sections. In the first one, the loading applied to the notched beam is uniform through the thickness with magnitude equal to the stress estimated from the virgin reduced order model on the top of the beam at 2 thicknesses away from the notch. Note that the stress distribution on the notched beam was computed from the finite element model. However, only one such computation is necessary, i.e., for a unit in-plane load, and then is scaled according to the stress predicted on the virgin beam. This enrichment is equivalent to having a constant stress intensity factor, equal to $S_{xx}^{(\max)} / S_{xx}^{(\text{nominal})}$, where $S_{xx}^{(\text{nominal})}$ is equal to the virgin beam stress.

The large deformations considered here lead to a coupling between bending and membrane stretching that modifies the configuration of the stresses for different

loading levels. Therefore, the stress intensity factor is also expected to change as the loading level is modified. In this light, the second stress enrichment considered was computed by applying a pressure varying through the thickness and equal to the $S_{xx}$ stress distribution at a location 2 beam thicknesses from the center of the notch. This pressure distribution was applied in a linear static analysis to one of the ends of the beam, while keeping the other end fixed. As with the previous enrichment, this analysis was performed on both notched and virgin beams. Then, the resulting stress from the notched beam was subtracted by the stress field from the virgin beam to obtain the localized stress at the location of the notch. The disadvantage of this method is that a linear static analysis has to be performed every time the loading changes.

### 5.7. Validation of Stress Enrichment: Static Loading

Shown in Table 5.4 are the peak stresses at the notch, as computed by the reduced order model of the virgin beam with the two enrichments previously described. Clearly, the agreement is very good for the largest stresses (Case 1 and Case 2). Note that the stresses of the NX/Nastran analysis for the virgin beam were enriched as well to assess the accuracy of the enrichment procedure independently of the reduced order model. The enriched NX/Nastran stress results agree very well with the corresponding predictions on the notched beam.

Table 5.4. Peak in-plane element stresses in the notch region for the four loading cases studied: 2.6kPa (Case 1), 17kPa (Case 2), -2.6kPa (Case 3), -17kPa (Case 4). Relative errors are with respect to the Nastran results of the notched beam.

| Computation | Case 1 | | Case 2 | | Case 3 | | Case 4 | |
|---|---|---|---|---|---|---|---|---|
| | MPa | Erel (%) | MPa | Erel (%) | MPa | Erel (%) | MPa | Erel (%) |
| Nastran Notched Beam | 32.3 | | 105.7 | | 6.4 | | 55.4 | |
| Nastran Virgin Beam + Enrichment #1 | 32.2 | 0.3 | 107 | 1.2 | 7.2 | 12.5 | 58.2 | 5 |
| Nastran Virgin Beam + Enrichment #2 | 32.3 | 0 | 107.2 | 1.4 | 7.1 | 11 | 58 | 4.6 |
| ROM Notched Beam | 32.7 | 1.2 | 105.8 | 0.1 | 7.3 | 14 | 65.2 | 17 |
| ROM Virgin + Enrichment #1 | 32.7 | 1.2 | 105.6 | 0.1 | 9.3 | 45 | 67.7 | 22 |
| ROM Virgin + Enrichment #2 | 32.8 | 1.5 | 105.9 | 0.2 | 9.2 | 44 | 67.7 | 22 |

### 5.8. Validation of Stress Enrichment: Dynamic Loading

For completeness it was desired to assess the effect of the enrichments in a dynamic analysis. The dynamic loading described in section 5.5 was used. The power spectral density of the $S_{xx}$ element stresses, at different locations along the beam are shown in Figs. 5.33-5.36. Interestingly, both enrichments lead to almost identical stress results. As seen in Fig. 5.33, the addition of the two enrichment schemes (described in section 5.5) to the ROM of the virgin beam, resulted in a good matching of NX/Nastran near the notch. This clearly is very pleasing, especially after looking at the results shown in Fig. 5.32.

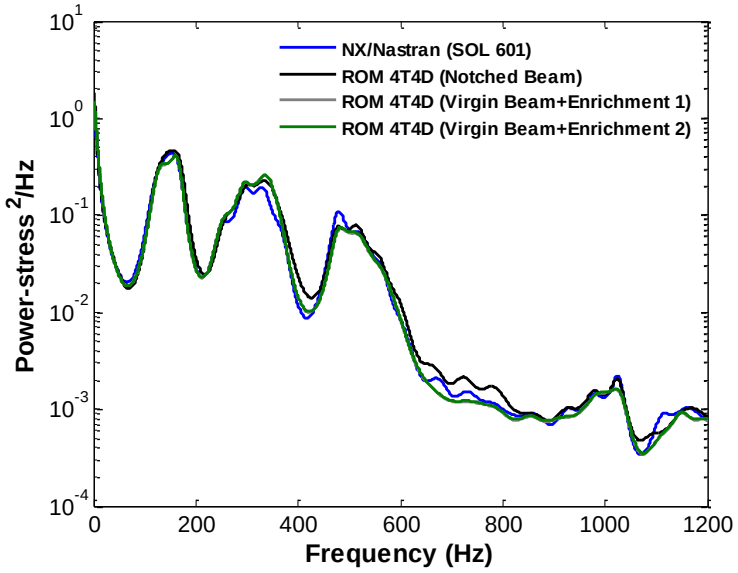


Figure 5.33. Power spectral density of the $S_{xx}$ element stress near the notch tip at *y=0*, *z=h* (*OASPL* = 147dB). Reduced order model ("ROM(4T4D)") and FEA ("NX/Nastran").

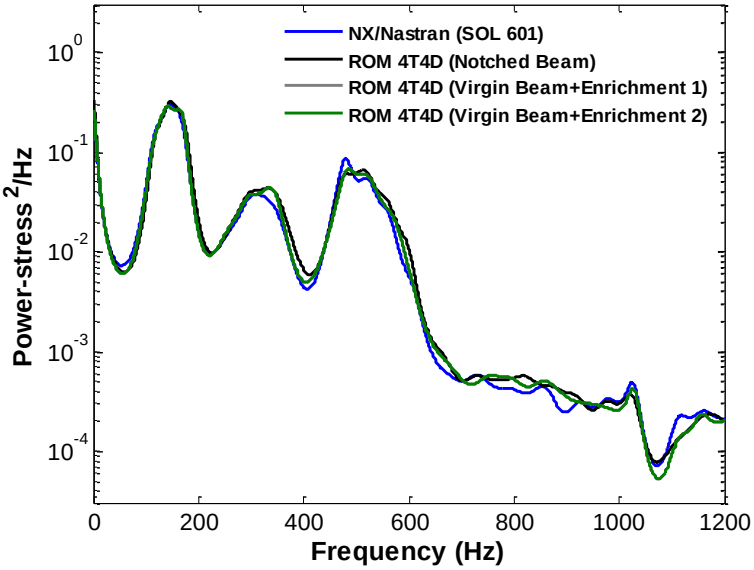


Figure 5.34. Power spectral density of the $S_{xx}$ element stress near the middle of the beam at *y=0*, *z=h* (*OASPL* = 147dB). Reduced order model ("ROM(4T4D)") and FEA ("NX/Nastran").

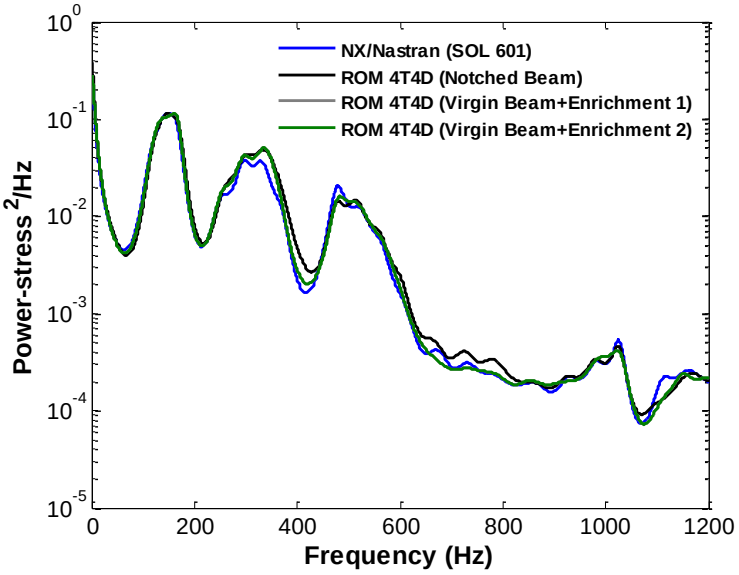


Figure 5.35. Power spectral density of the $S_{xx}$ element stress at 2 beam thicknesses from the notch tip and $y=0$, $z=h$ (*OASPL* = 147dB). Reduced order model ("ROM(4T4D)") and FEA ("NX/Nastran").

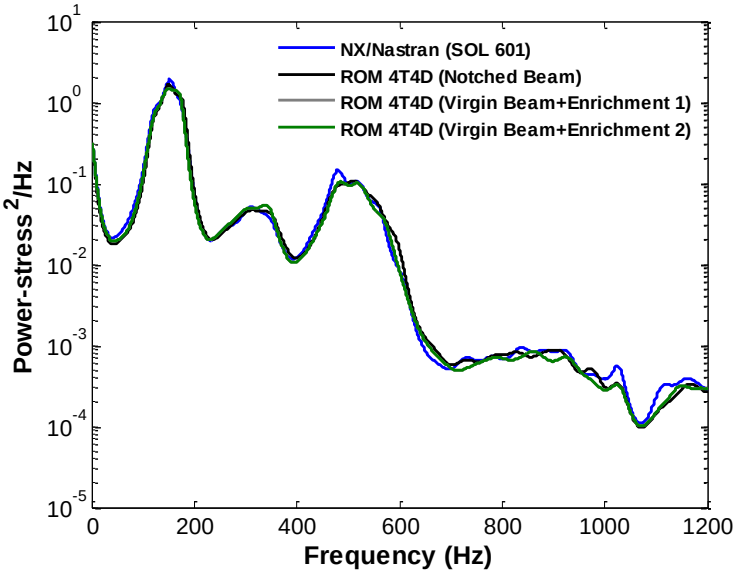


Figure 5.36. Power spectral density of the $S_{xx}$ element stress near the support of the beam at $y=0$, $z=h$ (*OASPL* = 147dB). Reduced order model ("ROM(4T4D)") and FEA ("NX/Nastran").

# CHAPTER 6

# ALGORITHMIC IMPROVEMENTS

## 6.1. Introduction

As discussed previously, due the large number of modes that may be needed to capture the response of a complex structure computational challenges may arise, not only in the construction process but also in the solution of the ROM equations. Challenges in the construction were addressed in Chapter 3, more specifically in the identification of the nonlinear stiffness coefficients. With respect to the solution of the ROM equations, two approaches will be presented in the present chapter to reduce the computational effort associated with their solution.

## 6.2. Benefits of "Cleaning" the Model in CPU Time

One of the major computational challenges associated with the solution of the ROM equations is the evaluation of the nonlinear restoring force

$$\left(\underline{\overline{K}}_{NL}\right)_i = \sum_{j=1}^{m}\sum_{l=j}^{m}\overline{K}_{ijl}^{(2)} q_j q_l + \sum_{j=1}^{m}\sum_{l=j}^{m}\sum_{p=1}^{m}\overline{K}_{ijlp}^{(3)} q_j q_l q_p \quad . \tag{6.1}$$

As mentioned in Chapter 2, the number of nonlinear stiffness coefficients for a ROM with $M$ modes is approximately equal to $M^4/6$. Therefore, a basis with 60 modes would lead to approximately 2 million coefficients. Clearly, the computational effort involved in computing the expression in Eq. (6.1) can be very large if one considers that this has to be performed for every iteration in the nonlinear solution and every time step to be analyzed.

The reduced order modeling procedure relies on a finite element model of the structure. In the present situation of "large" deflections, the von Karman strain definition is generally adopted.

$$\varepsilon_x = \frac{\partial u_1}{\partial x} + \frac{1}{2}\left(\frac{\partial u_3}{\partial x}\right)^2 \quad \varepsilon_y = \frac{\partial u_2}{\partial y} + \frac{1}{2}\left(\frac{\partial u_3}{\partial y}\right)^2 \quad \varepsilon_z = \frac{\partial w}{\partial z} = 0$$

$$\gamma_{xy} = \frac{1}{2}\left[\frac{\partial u_1}{\partial y} + \frac{\partial u_2}{\partial x} + \left(\frac{\partial u_3}{\partial x}\right)\left(\frac{\partial u_3}{\partial y}\right)\right] \quad \gamma_{xz} = \frac{1}{2}\left[\frac{\partial u_1}{\partial z} + \frac{\partial u_3}{\partial x}\right] \tag{6.2}$$

$$\gamma_{yz} = \frac{1}{2}\left[\frac{\partial u_2}{\partial z} + \frac{\partial u_3}{\partial y}\right].$$

The basic assumption of the von Karman strain definition is that the force induced transverse motions in the weak bending direction are much larger than the in-plane displacement induced by the nonlinear coupling with the transverse displacement. While the low-frequency linear modes included in the reduced order model have in general dominant transverse components (i.e., in the direction normal to the panel), the dual modes have dominant in-plane features.

In this light, since the nonlinear stiffness coefficients are computed from the finite element model of the structure, the coefficients related to the product of two or three dual modes are expected to have a negligible effect in the solution of the generalized coordinates from the ROM equations of motion. This is expected to be the case as long as the strain-displacement relations from Eq. (6.2) are used in the finite element package used to compute the stiffness coefficients. With this in mind, the following stiffness coefficients could be ignored in the evaluation of Eq. (6.1): $K_{tii}^{(2)}$, $K_{iti}^{(2)}$, $K_{iii}^{(2)}$, $K_{ttii}^{(3)}$, $K_{tiii}^{(3)}$, $K_{itti}^{(3)}$, $K_{itii}^{(3)}$, and $K_{iiii}^{(3)}$, where, the index *t* corresponds to a linear mode, the index *i* corresponds to a dual mode. Furthermore, due to the symmetry of the coefficients, $K_{tii}^{(2)}$ and $K_{tii}^{(2)}$ have to be eliminated because $K_{tii}$ and $K_{ttii}$ were removed. In order to ensure convergence of the solution, the cubic coefficients $K_{ttti}^{(3)}$ and $K_{ittt}^{(3)}$ were ignored in the evaluation of Eq. (6.1).

This approach was validated on the nonlinear static and dynamic solutions from Chapter 4. First, the 82-mode model from the nonlinear static validation was investigated. Shown in Table 6.1 are the prediction errors for the full and the "cleaned" models along with the computation times needed for the solution of the problem.

Table 6.1. Comparison of relative errors and CPU time between "Full Model" and "Cleaned Model".

| | T3 | In-plane Mag. | T2 | T1 | CPU Time |
|---|---|---|---|---|---|
| Full Model | 1.2% | 4.3% | 3.3% | 36% | 9 minutes |
| Cleaned Model | 1.4% | 4.5% | 3.4% | 37.7% | 1 minute |

The correlation of the cleaned solution with the full one is very good and the reduction in the CPU time is noticeable.

The validation on the dynamic problem with an acoustic excitation of 144dB yielded excellent results as well. Shown in Figs. 6.1-6.6 is a comparison of the transverse and in-plane response at bays 1, 2, and 5 of the 9-bay panel from Chapter 4. Clearly, the correlation between the "full" and "cleaned" solutions is excellent. In addition, the CPU time for the "cleaned" solutions was 6.5 times lower than the one for the "full" solution.

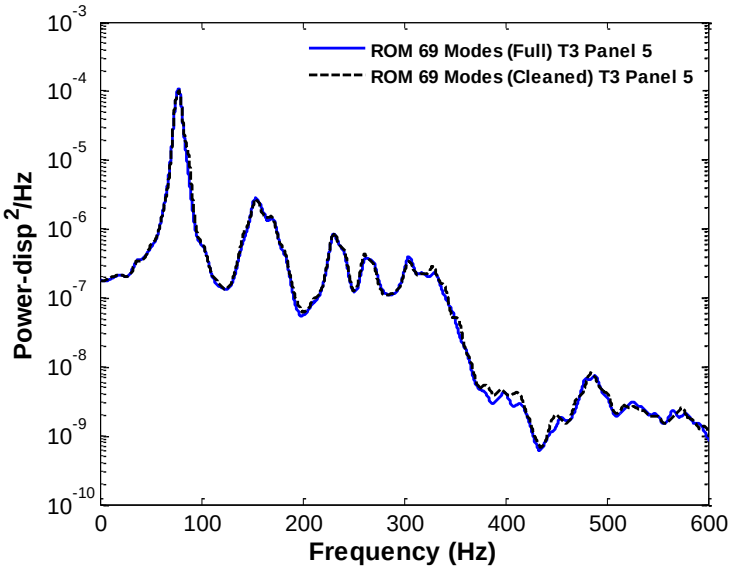


Figure 6.1. Power spectral density of the transverse (T3) displacement at the middle point of bay 5. Reduced order models "Full" and "Cleaned", *SPL* =144dB.

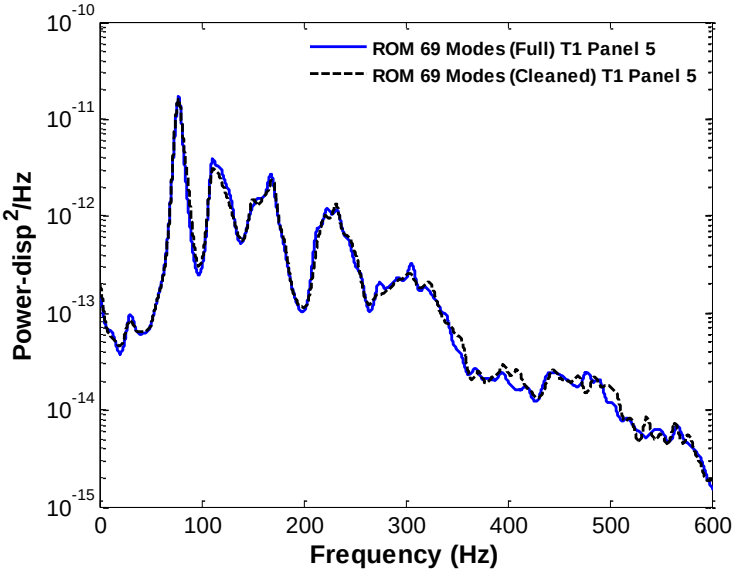


Figure 6.2. Power spectral density of the in-plane (T1) displacement at the middle point of bay 5. Reduced order models "Full" and "Cleaned", *SPL* =144dB.

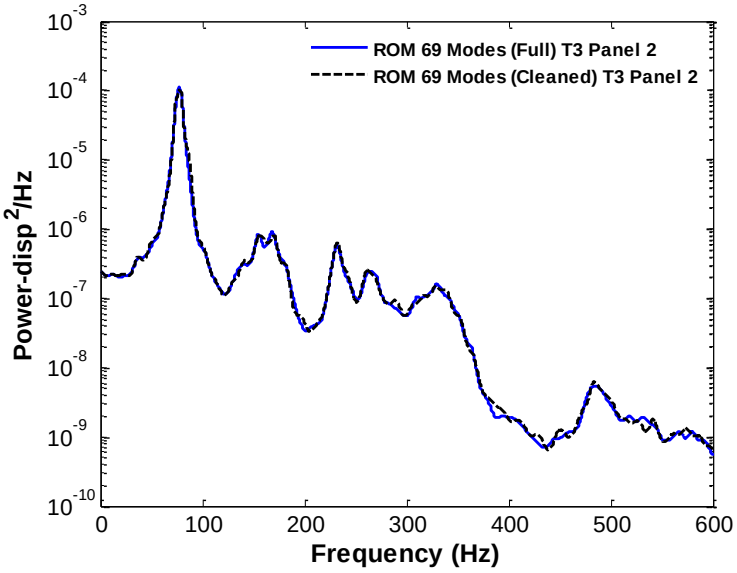


Figure 6.3. Power spectral density of the transverse (T3) displacement at the middle point of bay 2. Reduced order models "Full" and "Cleaned", *SPL* =144dB.

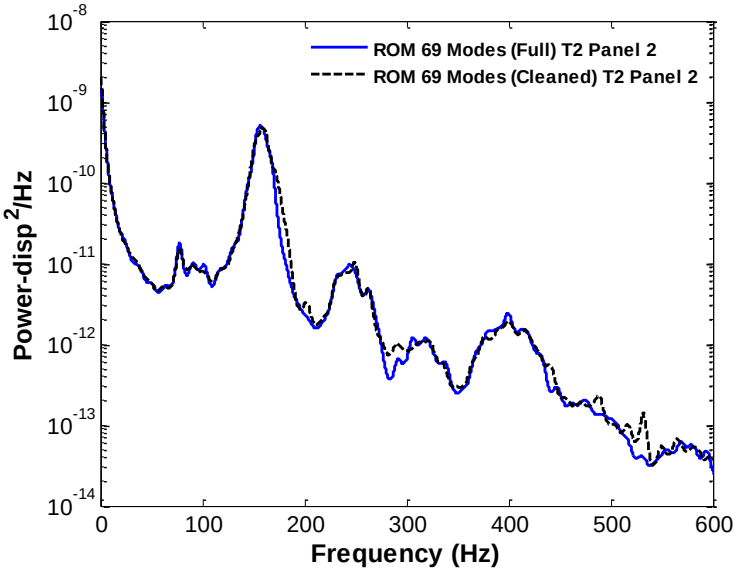


Figure 6.4. Power spectral density of the in-plane (T2) displacement at the middle point of bay 2. Reduced order models "Full" and "Cleaned", *SPL* =144dB.

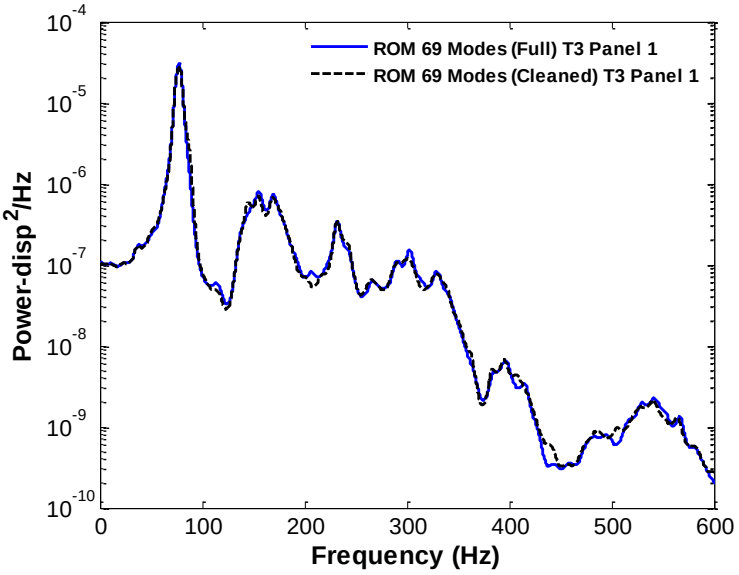


Figure 6.5. Power spectral density of the transverse (T3) displacement at the middle point of bay 1. Reduced order models "Full" and "Cleaned", *SPL* =144dB.

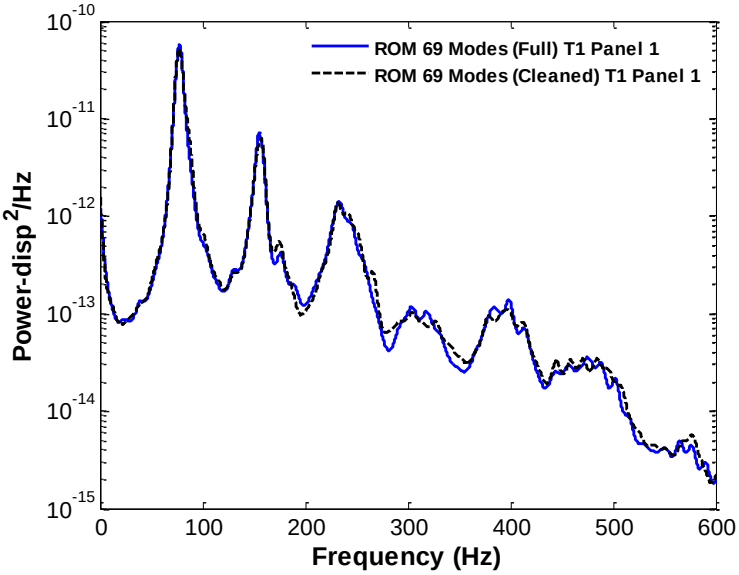


Figure 6.6. Power spectral density of the in-plane (T1) displacement at the middle point of bay 1. Reduced order models "Full" and "Cleaned", *SPL* =144dB.

### 6.3. Static Condensation of the Dual Modes

As discussed in previous chapters, the purpose of the dual modes is to capture the in-plane displacement induced by large loading conditions through the nonlinear coupling

with the transverse deflection. For simple structures, such as a clamped-clamped beam under pure transverse loading conditions, they are not directly excited by the loading, but respond quasi-statically [4, 14-15]. With this in mind, the inertia of the duals could be neglected and the generalized coordinates of the dual modes solved for explicitly and substituted into the equations of the linear modes. This in turn would lead to a reduction of the number of equations to be solved and possibly of the nonlinear iterations needed for the solution to converge at every time step.

In this light, the ROM equations can be split into the equations of the linear modes and those of the dual modes. Assuming that the model consists of one linear mode and one dual, using the "cleaning" scheme from the previous section, and assuming the dual modes to act quasi-statically, the resulting equations are as follows

$$\begin{aligned} &M_{tt}\ddot{q}_t + C_{tt}\dot{q}_t + K_{tt}q_t + K_{ttt}q_t^2 + K_{tti}q_t q_i + K_{tttt}q_t^3 = F_t \\ &K_{ii}q_i + K_{itt}q_t^2 = F_i \end{aligned} \tag{6.3}$$

where, the index $t$ corresponds to a linear mode, the index $i$ corresponds to a dual mode, and the forces $F_t$ and $F_i$ are time dependent. Then, solving for the generalized coordinate of the dual mode, $q_i$, from the second equation, and substituting it into the equation of the linear mode yields

$$M_{tt}\ddot{q}_t + C_{tt}\dot{q}_t + K_{tt}q_t + K_{ttt}q_t^2 + K_{tti}q_t K_{ii}^{-1}\left(F_i - K_{itt}q_t^2\right) + K_{tttt}q_t^3 = F_t\,. \tag{6.4}$$

Finally, rearranging terms the following expression is obtained

$$\begin{aligned} M_{tt}\ddot{q}_t + C_{tt}\dot{q}_t + \left(K_{tt} + K_{tti}K_{ii}^{-1}F_i\right)q_t + K_{ttt}q_t^2 + \\ + \left(K_{tttt} - K_{tti}K_{ii}^{-1}K_{itt}\right)q_t^3 = F_t \end{aligned}\,. \tag{6.5}$$

For the 9-bay panel $F_i$ is not equal to zero, so it leads to a parametric type excitation. In this case, the computational effort is increased since the inverse of

$K_{tt} + K_{tti} K_{ii}^{-1} F_i$ would have to be computed for every time step. Accordingly, this approach was not adopted.

# CHAPTER 7

## SUMMARY

The focus of this investigation has been on the expansion of the current reduced order modeling techniques of geometrically nonlinear problems to problems in the micro-scale and macro-scale.

First, a background on the derivation of the ROM equations of motion was given. In addition, the identification of the ROM parameters and the selection of the basis needed to represent the displacement field of the structure were discussed.

Then, two challenges associated with the analysis of complex structural models were identified: the identification of the ROM stiffness coefficients and the selection of the basis. Two key modifications of the existing approaches were described:

(1) A novel identification strategy of the reduced order model parameters was derived which is based on the use of the tangent stiffness matrix and necessitates a computational effort only proportional to $M^2$, where $M$ is the number of basis functions, as opposed to $M^3$ in the current formulations.

(2) The linear and dual mode basis selection strategy was extended to include eigenvectors of the tangent stiffness matrix at key static deformations.

The above novel developments were successfully validated on the nonlinear static and dynamic responses of a 9-bay panel structure modeled with 96,156 degrees of freedom within Nastran. In addition to the conventional ROM approach, a multi-scale analysis was explored. This approach was useful in gaining more understanding of the physics of the 9-bay panel considered in this section.

Furthermore, a first assessment of the predictive capabilities of nonlinear reduced order models for notched panels was carried out. An aluminum clamped-clamped beam with a notch placed at 30% of its length and of depth equal to a quarter of the thickness

was considered as a typical panel. As expected, the notch was found to have a negligible effect on the first few natural frequencies of the beam, as compared to the virgin beam, but also on the corresponding mode shapes. In addition, only small notch-related effects could be detected on the in-plane component of the dual modes, which are basis functions constructed to capture the nonlinear transverse in-plane coupling occurring in large deformations. However, a large, rather broad peak was observed in the smaller transverse component of the dual modes of the notched beam which is absent on the corresponding plot for the virgin beam.

A displacement field induced by a uniform pressure on the beam, large enough to induce nonlinearity, i.e. peak transverse displacements of the order of 2 and 4 thicknesses, was also found to be very weakly dependent on the notch. Furthermore, this displacement field was shown to be well predicted by the reduced order models of both notched and virgin beams. Also, a dynamic validation was carried out and the matching of the power spectrum of the displacement at selected points was excellent.

In regards to the prediction of the stress field, it was found that the notched beam reduced order model was indeed able to capture accurately the stress distribution induced by the pressure loading in both static and dynamic loading cases.

Nevertheless, it was questioned whether a prediction based on the virgin beam reduced order model could also be used if appropriately "enriched" with the notched beam stress field in a superposition-like manner. Two enrichment options were assessed that rely on this stress field as obtained, in a *linear* finite element static analysis, from a notched beam subjected to the stress state induced on the virgin beam near the notch location. This methodology led to good to excellent predictions of the stress field near the notch for both static and dynamic loading cases.

The last chapter of this work dealt with the assessment of a series of algorithmic improvements aimed at further reducing the CPU time of the solution of the ROM equations of motion. First, it was seen that by taking advantage of the von Karman strain assumption used for the beam and shell elements in NX/Nastran, the computational effort in the evaluation of the nonlinear restoring force could be reduced. This in turn led to substantial reductions in the computational time, with execution times which were up to 9 times faster than before. Also, given that the dual modes are excited quasi-statically, a static condensation of the duals modes was proposed. It was found that the force in the in-plane direction appeared in the coefficient of the linear equations leading to a type of parametric excitation. This in turn increased the computational effort in problems where the in-plane force is not equal to zero.

## REFERENCES


[1] Blevins, R.D., Holehouse, I., and Wentz, K.R. "Thermoacoustic Loads and Fatigue of Hypersonic Vehicle Skin Panels." *Journal of Aircraft*, no. 30 (1993): 971-978.

[2] Rao, S.S. *Mechanical Vibrations*. Upper Saddle River, New Jersey: Pearson/Prentice Hall, 2004.

[3] Mignolet, M.P. *Encyclopedia of Aerospace Engineering* by R. Blockley and W. Shyy (joint editors). 1st ed., 3 vols. "Dynamic Response Computations." Wiley & Sons, 2010.

[4] Mignolet, M.P., Przekop, A., Rizzi, S.A., and Spottswood, S.M., "A Review of Indirect/Non-Intrusive Reduced Order Modeling of Nonlinear Geometric Structures," *Journal of Sound and Vibration*, To appear, 2012.

[5] McEwan, M.I., Wright, J.R., Cooper, J.E., and Leung, A.Y.T. "A combined Modal/Finite Element Analysis Technique for the Dynamic Response of a Nonlinear Beam to Harmonic Excitation." *Journal of Sound and Vibration* 243 (2001): 601-624.

[6] Hollkamp, J.J., Gordon, R.W., and Spottswood, S.M. "Nonlinear Modal Models for Sonic Fatigue Response Prediction: A Comparison of Methods." *Journal of Sound and Vibration* 284 (2005): 1145-1163.

[7] Hollkamp, J.J., and Gordon, R.W., 2008, "Reduced-Order Models for Nonlinear Response Prediction: Implicit Condensation and Expansion," *Journal of Sound and Vibration*, Vol. 318, pp. 1139–1153.

[8] Przekop, A., and Rizzi, S.A., "A Reduced Order Method for Predicting High Cycle Fatigue of Nonlinear Structures," *Computers and Structures*, Vol. 84, No. 24-25, pp. 1606-1618, 2006.

[9] Kim, K., Khanna, V., Wang, X.Q., and Mignolet, M.P., "Nonlinear Reduced Order Modeling of Flat Cantilevered Structures," *Proceedings of the 50th Structures, Structural Dynamics, and Materials Conference*, Palm Springs, California, May 4-7, 2009. AIAA Paper AIAA-2009-2492.

[10] Mignolet, M.P., Radu, A.G., and Gao, X. "Validation of Reduced Order Modeling for the Prediction of the Response and Fatigue Life of Panels Subjected to Therm-Acoustic Effects." *Proceedings of the 8th International Conference on Recent Advances in Structural Dynamics.* Southampton, United Kingdom, 2003.

[11] Radu, A., Yang, B., Kim, K., and Mignolet, M.P. "Prediction of the Dynamic Response and Fatigue Life of Panels Subjected to Thermo-Acoustic Loading." *Proceedings of the 45th Structures, Structural Dynamics, and Materials Conference.* Palm Springs, California, 2004. AIAA Paper AIAA-2004-1557.

[12] Kim, K., Wang, X.Q., and Mignolet, M.P., "Nonlinear Reduced Order Modeling of Functionally Graded Plates," *Proceedings of the 49th Structures, Structural Dynamics, and Materials Conference*, Schaumburg, Illinois, Apr. 7-10, 2008. AIAA Paper AIAA-2008-1873.

[13] Przekop A., and Rizzi S.A., "Nonlinear Reduced Order Random Response Analysis of Structures with Shallow Curvature," AIAA Journal Vol. 44 (8), pp. 1767-1778, 2006.

[14] Gordon R.W., and Hollkamp, J.J., "Reduced-Order Modeling of the Random Response of Curved Beams using Implicit Condensation," AIAA-2006-1926, 2006.

[15] Spottswood, S.M., Hollkamp, J.J., and Eason, T.G., "On the Use of Reduced-Order Models for a Shallow Curved Beam Under Combined Loading," *Proceedings of the 49th Structures, Structural Dynamics, and Materials Conference*, Schaumburg, Illinois, Apr. 7-10, 2008. AIAA Paper AIAA-2008-1873.

[16] Przekop, A., and Rizzi, S.A., "Dynamic Snap-Through of Thin-Walled Structures by a Reduced-Order Method," *AIAA Journal*, Vol. 45, No. 10, pp. 2510–2519, 2007.

[17] Spottswood, S.M., Eason, T.G., Wang, X.Q., and Mignolet, M.P., "Nonlinear Reduced Order Modeling of Curved Beams: A Comparison of Methods," *Proceedings of the 50th Structures, Structural Dynamics, and Materials Conference*, Palm Springs, California, May 4-7, 2009. AIAA Paper AIAA-2009-2433.

[18] Kim, K., Kim, Y.C., Mignolet, M.P., Liu, D.D., Chen, P.C., Lee, D.H., "Random Aeroelastic Response Due to Strong Hypersonic Unsteady-Wave/Shock Interaction with Acoustic Loads," *Proceedings of the 48th Structures, Structural Dynamics, and Materials Conference*, Honolulu, Hawaii, Apr. 23-26, 2007. AIAA Paper AIAA-2007-2014.

[19] Liu, D.D., Chen, P.C., Zhang, Z., Wang, Z., Yang, S., Lee, D.H., Mignolet, M.P., Kim, K., Liu, F., Lindsley, N., and Beran, P., "Continuous Dynamic Simulation of Nonlinear Aerodynamic/Nonlinear Structure Interaction (NANSI) for Morphing Wing Aeroelasticity," *Proceedings of the 50th Structures, Structural Dynamics, and Materials Conference*, Palm Springs, California, May 4-7, 2009. AIAA Paper AIAA-2009-2572.

[20] Liu, D.D., Wang, Z., Yang, S., Cai, C., Wang, X.Q., and Mignolet, M.P., "Nonlinear Aeroelastic Methodology for A Membrane-on-Ballute Model with Hypersonic Bow Shock," *Proceedings of the 50th Structures, Structural Dynamics, and Materials Conference*, Palm Springs, California, May 4-7, 2009. AIAA Paper AIAA-2009-2363.

[21] Perez, R., Wang, X.Q., and Mignolet, M.P., "Nonlinear Reduced Order Models for Thermoelastodynamic Response of Isotropic and FGM Panels," *AIAA Journal*, Vol. 49, pp. 630-641, 2011.

[22] Perez, R., Wang, X.Q., and Mignolet, M.P., "Steady and Unsteady Nonlinear Thermoelastodynamic Response of Panels by Reduced Order Models," *Proceedings of the 51th Structures, Structural Dynamics, and Materials Conference*, Orlando, Florida, April 12-15, 2010. AIAA Paper AIAA-2010-2724.

[23] Matney, Perez, R., and Mignolet, M.P., "Nonlinear Unsteady Thermoelastodynamic Response of a Panel Subjected to an Oscillating Flux by Reduced Order Models," *Proceedings of the 52th Structures, Structural Dynamics, and Materials Conference*, Denver, Colorado, April 4-7, 2011. AIAA Paper AIAA-2011-2016.

[24] Matney, A., Perez, R., Spottswood, S.M., Wang, X.Q., and Mignolet, M.P., "Nonlinear Structural Reduced Order Modeling Methods for Hypersonic Structures", *Proceedings of the 53rd Structures, Structural Dynamics, and Materials Conference*, Honolulu, Hawaii, April 23-26, 2012. AIAA Paper AIAA-2012-1972.

[25] Perez, R., Wang, X.Q., and Mignolet, M.P., "Reduced Order Modeling for the Nonlinear Geometric Response of Cracked Panels," *Proceedings of the 52th Structures, Structural Dynamics, and Materials Conference*, Denver, Colorado, April 4-7, 2011. AIAA Paper AIAA-2011-2018.

[26] Bonet, J., and Wood, R.D., *Nonlinear Continuum Mechanics for Finite Element Analysis*, Cambridge: Cambridge University Press, 1997.

[27] Fung, Y.C., and Tong, P. *Classical and Computational Solid Mechanics* . River Edge, New Jersey: World Scientific, 2001.

[28] Muravyov, A.A., and Rizzi, S.A., "Determination of Nonlinear Stiffness with Application to Random Vibration of Geometrically Nonlinear Structures," Computers and Structures, Vol. 81, pp. 1513-1523, 2003

[29] Przekop, A., Rizzi, S.A., and Groen, D.S., "Nonlinear Acoustic Response of an Aircraft Fuselage Sidewall Structure by a Reduced-Order Analysis," *Proceedings of the 9th International Conference on Recent Advances in Structural Dynamics*, Southampton, United Kingdom, Jul. 17-19, 2006.

[30] P. Tiso, E. Jansen, M. Abdalla, "Reduction Method for Finite Element Nonlinear Dynamic Analysis of Shells," *AIAA Journal*, Vol. 49 pp. 2295-2304, 2011.

[31] Buehrle, R.D. Fleming, G.A., Pappa, R.S., and Grosveld, F.W., "Finite Element Model Development For Aircraft Fuselage Structures," *Proceedings of the 18th Modal Analysis Conference*, San Antonio, Texas, Feb., 2000.

[32] Craig Jr., R.R. and Kurdilla, A.J. *Fundamentals of Structural Dynamics*. Hoboken, New Jersey: John Wiley & Sons, 2006.

[33] Mignolet M.P. Soize, C., "Nonparametric Stochastic Modeling of Structures with Uncertain Boundary Conditions and Uncertain Coupling Between Substructures," *Proceedings of the 49th Structures, Structural Dynamics, and Materials Conference*, Schaumburg, Illinois, Apr. 7-10, 2008.

[34] Mignolet, M.P. and Soize, C., "Stochastic reduced order models for uncertain geometrically nonlinear dynamic systems," *Comput. Methods Appl. Mech. Engrg.*, Vol. 197, pp. 3951-3963, 2008.